ISSN No. 0737-5352-51

Exploratory Study For Detecting Low Clouds (Base < 10,000 Feet) Over The Southwestern United States Using Tropical Rainfall Measuring Mission Microwave (TRMM) Imager 85.5 GHZ Data And Coincident 10.8 Micron Infared Data

Stephen J. Barlow

Thomas H. Vonder Haar

Research Supported by the Department of Defense Center for Geosciences/Atmospheric Research, under the Army Research Laboratory (ARL) Cooperative Agreement No. DAAL01-98-2-0078, and by the Air Force Institue of Technology (AFIT)

CIRA Cooperative Institute for Research in the Atmosphere

Center for Geosciences/Atmospheric Research

Colorado State University

EXPLORATORY STUDY FOR DETECTING LOW CLOUDS (BASE < 10,000 FEET) OVER THE SOUTHWESTERN UNITED STATES USING TROPICAL RAINFALL MEASURING MISSION MICROWAVE (TRMM) IMAGER 85.5 GHZ DATA AND COINCIDENT 10.8 MICRON INFRARED DATA

Submitted by

Stephen J. Barlow

Department of Atmospheric Science

In partial fulfillment of the requirements

for the Degree of Master of Science

Colorado State University

Fort Collins, Colorado

Summer 2001

ABSTRACT OF THESIS

EXPLORATORY STUDY FOR DETECTING LOW CLOUDS (BASE < 10,000 FEET) OVER THE SOUTHWESTERN UNITED STATES USING TROPICAL RAINFALL MEASURING MISSION MICROWAVE (TRMM) IMAGER 85.5 GHZ DATA AND COINCIDENT 10.8 MICRON INFRARED DATA

Recent research in retrieving cloud liquid water over land using the 85.5 GHz microwave channel has shown limited success. This work usually requires extensive manipulation of the data to correct for atmospheric effects, and to eliminate rain events. Even with these corrections, the over-land methods must still address the complex spatial variability of soil and vegetation characteristics, which have a profound affect on surface emissivity, e.g., a non-uniform background. This work uses the Normalized Polarization Difference (NPD) method in an attempt to identify low cloud signature over the Southwestern United States from 1 June to 31 August 1998. This will provide nighttime capability in identifying low-cloud areas over data-sparse, data-denied regions with relatively uniform terrain characteristics. The development of a simplified method for use in data-sparse, data-denied regions was of prime importance.

In order to identify low clouds, effective surface emittance calculations were made using co-located Tropical Rainfall Measuring Mission Microwave 85.5 GHz data and coincident 10.8 μm infrared data for clear-sky conditions. Based on previous work, the Southwestern United States, in general, should have the large polarization differences (>

0.015) as well as uniform skin temperatures, which could provide a suitable background to detect low cloud signal above the background noise. Eleven sites were chosen based on varying degrees of polarization difference, as well as having available surface and upper air data. In situ surface observations were used to identify the low cloud base, while the infrared brightness temperature at 10.8 μm was used to estimated the cloud top height using the nearest upper air sounding. The estimated cloud thickness was calculated from this data.

Extensive efforts were made to eliminate multiple cloud layers, which would have a negative impact on brightness temperatures. A scattering index, the Grody algorithm, and surface observations were used to filter precipitating clouds. The results using a linear regression best fit indicated poor correlation (R^2) between the NPD and the estimated low-cloud thickness with values of R^2 ranging from 0.002 to 0.345. Four primary error mechanisms were identified, and quantified. The uncorrected atmosphere accounted for about a 0.7-1.7 K error; horizontal variations in infrared temperature on the scale of 2.0-7.3K; instrument noise of about 1.5K; and effective surface emissivity relative uncertainties ranging from 0.22-1.16% . Future improvements in sensor noise characteristics and resolution, as well as the ability to perform instantaneous atmospheric corrections using coincident sounder and microwave imager data should lead to a viable NPD method over land.

Stephen Barlow
Atmospheric Science Department
Colorado State University
Fort Collins, CO 80523
Summer 2001

ACKNOWLEDGEMENTS

First and foremost, I would like to thank my committee: Dr. Tom Vonder Haar, Dr. Steve Rutledge, and Dr. David Krueger for their support and patience throughout this process. Your positive support allowed me to finish this project while working full-time as an Air Force Typhoon Duty Officer in Hawaii, and to finish my Master's Degree.

This research required extensive data processing and computer programming in its early stages, and was made possible only with the invaluable assistance of the Cooperative Institute for Research in the Atmosphere (CIRA) and the Colorado State University (CSU). I would also like to thank a number of people who provided both technical support and key advice. First of all, Andy Jones who's in-depth knowledge of the research problem, and expertise in data fusion methods proved invaluable. His assistance in computer programming, data processing, and data calibration techniques was critical in the initial stages of the research. John Forsythe for his ability to solve problems in the most expeditious and exact manner. Kelly Dean for his computer programming assistance. Cindy Combs for her advice and programming help. Tom Greenwald for providing the TMI and VIRS data. Ken Knapp for the use of his computer resources which greatly expedited my work, and also, for his advice on writing a thesis. I would also like to express my deep appreciation to Richard Moore for his friendship, candidness, and moral support. Finally, I would like to thank my wife, Myongcha, and my sons; Kenny and Daniel for always making sure my priorities were in the right place.

This work was funded by the DoD Center for Geosciences/Atmospheric Research under the Army Research Laboratory (ARL) Cooperative Agreement DAAL01-98-2-0078, and by the Air Force Institute of Technology (AFIT).

TABLE OF CONTENTS

LIST OF FIGURES

LIST OF TABLES

Chapter 1

Introduction

There has been a large amount of research conducted in the area of estimating cloud liquid water and cloud properties over water surfaces using passive microwave data. The over-water microwave algorithms benefit from the fact that the radiative effects of cloud water are large due to the low microwave emissivity of the surface (approximately 0.5); therefore clouds appear radiatively warm over the colder water background.

Comparatively, there has been very little work done in retrieving cloud liquid water amounts and cloud properties over land using passive microwave data other than exploratory studies and simulations. The difficulty in measuring cloud liquid water amounts over land is primarily due to the horizontal variation of soil types, vegetation types, and the moisture content of the soil, all of which greatly impact the surface emissivity values. The poor spatial and temporal resolution of passive microwave sensors, in general, has also contributed to the difficulty in retrieving cloud parameters over land since there is typically large variability in surface properties within the instrument's footprint.

One of the more important benefits of using passive microwave measurements over land is their ability to penetrate layered clouds and retrieve cloud information at night or day. This data would be invaluable, especially over remote, data-sparse areas of the globe. Unfortunately, the capabilities of passive microwave over land have yet to be proven to the extent that justifies increased spending to improve the resolution and noise characteristics or to motivate extensive research.

1.1 Viability of Over-Land Retrievals

A number of simulations have shown that cloud liquid water path (LWP) can be extracted from microwave data. Diak (1995) used the 183-GHz water vapor data (channel 19 and 20) from the Advanced Microwave Sounding Unit (AMSU) to estimate column cloud water amounts for non-precipitating cloud. Diak showed that when there is adequate signal to noise, the effective cloud fraction could be used successfully as a proxy for cloud liquid water amount under varying surface emissivity, atmospheric conditions, and cloud conditions. The exploratory study by Jones and Vonder Haar (1990) indicated that there is promise in estimating cloud liquid water path (LWP) over land surfaces. This was substantiated further by recent work (Greenwald et al., 1997) that has demonstrated that detection and retrieval of cloud liquid water over land surfaces is indeed feasible under certain conditions using the highest frequency channels of the Special Sensor Microwave Imager (SSM/I), e.g., 85.5 GHz.

There is no doubt in the research and operational meteorology community that further research into developing reliable methods that can extract cloud properties over land, e.g., cloud liquid water, cloud height, etc., would be invaluable. Cloud liquid water path (LWP) is one such parameter that might possibly be useful as an indicator of potential aircraft icing (Popa Fotino et al., 1986). Cloud water is a primary influence in the transfer of infrared and visible radiation, so that an understanding of the threedimensional distribution of this quantity would benefit the radiative transfer components of atmospheric models (Diak, 1995). In context of global climate studies, satellite estimates of cloud LWP can also contribute to a better understanding of the connection between cloud physical properties and the radiation budget, which is important since clouds are known to have a significant impact on the radiation balance of the earth. Over remote, data-sparse regions of the world, the ability to extract cloud properties, e.g., identification of cloud decks or LWP, would provide vital information to the military planners for anti-aircraft weapon avoidance, and could provide input into complex weapon targeting algorithms. Additionally, passive microwave techniques have potential to provide quantitative information on whether or not precipitation is occurring below layered clouds, or whether there is a low deck of stratocumulus beneath a cirrostratus overcast.

Over-land passive radiometry research remains a daunting challenge, however, there must be a continued drive to improve both passive microwave sensors and techniques. This work represents one such exploratory study addressing the operational requirement for a quick-turn microwave satellite product. Specifically, this work addresses the need for a day/night cloud identification product for use in remote, data-sparse, data-denied regions.

1.2 Research Objectives

The primary goal of this research is to utilize the so-called Normalized Polarization Difference (NPD) method (Greenwald et al., 1997) to detect non-precipitating low clouds (bases less than 10,000 feet) over the Southwestern United States in the period from

June-August 1998. NPD is derived more completely in chapter 5, and is equal to the microwave brightness temperature difference at 85.5 GHz divided by the polarization difference at 85.5 GHz, $\Delta T_B/\Delta\varepsilon$. Although, the NPD method was originally created to find cloud liquid water path over land, this work will apply the NPD method to the related area of cloud detection in an attempt to separate low cloud signals from the background signal using the degree of depolarization of the signal.

Previous work by Jones and Vonder Haar (1997) and Combs et al. (1998) have shown that this region, in general, has a significant surface polarization difference greater than the background noise. Clouds act to depolarize the radiation, therefore, as cloud thickness increases there should be greater depolarization. Cloud thickness values will be calculated from in situ surface observation and upper air data, and will be correlated to NPD measurements. This work hopes to take advantage of the benefits of the NPD method, and of the improved spatial resolution of the Tropical Rainfall Measuring Mission (TRMM) Microwave Imager (TMI) 85.5 GHz channel, so that the background surface emissivity can be more accurately determined.

This work will also explore and attempt to quantify the errors involved in passive microwave radiometry over land, e.g., instrument noise, horizontal variability of effective surface emissivity, etc., and their impact on the development of a simple low-cloud identification method.

1.3 Overview

Chapter 2 will focus on the theory and assumptions used in passive microwave radiative transfer theory that provide the basis for this work, and specifically as they pertain to the non-precipitating cloud case. Further, this chapter will examine the atmospheric and surface effects. Chapter 3 will discuss the processing and calibration of the TMI and the visible/infrared sounder (VIRS) data. The unique aspects of the applicable sensors that are relevant to this work will be covered briefly. It will also discuss the method used to co-locate and merge the TMI and VIRS data into a common projection. Chapter 4 summarizes the effective surface emittance retrieval procedure, which is a clear-sky method, and introduces a conservative cloud-free discrimination threshold. The results will be presented, and the effective surface emittance and effective surface emittance composite calculations will be substantiated by a detailed error analysis of the method and approximations used. Chapter 5 will discuss the development and evolution of the NPD method. Its theoretical basis, and its strengths and weaknesses will be addressed from a mathematical and physical approach. Results will be presented for selected sites within the area of interest, namely the Southwestern United States.

Chapter 2

Fundamentals of Passive Microwave Remote Sensing

The microwave region of the electromagnetic spectrum extends from roughly 0.3 to 300 GHz (1 m to 1 mm in wavelength). Figure 2.1 illustrates the clear sky transmittance through the atmosphere for the microwave spectrum. Atmospheric windows are apparent near 35, 90, and 135 GHz while strong O_2 absorption bands occur near 60 and 120 GHz. A strong water vapor absorption band is located near 180 GHz with a much weaker absorption band around 20 GHz.

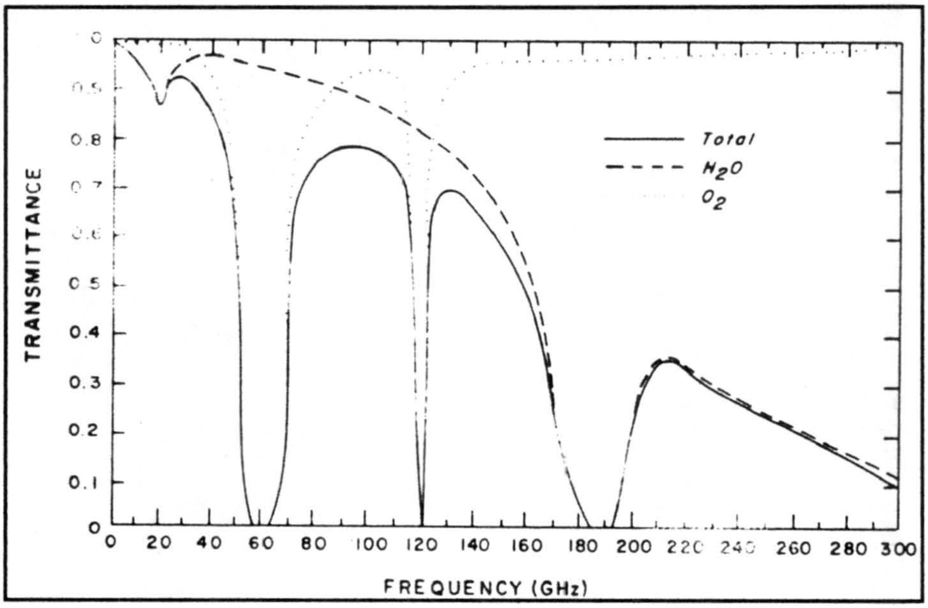

Figure 2.1: Atmospheric transmittance as a function of frequency (from Liou, 1980).

Atmospheric transmittance, however, can change considerably depending on the mean atmospheric conditions (see Fig. 2.2). In the window region near 85.5 GHz, the polar atmosphere has significantly greater transmissivity than the humid tropical atmosphere, or the standard atmosphere.

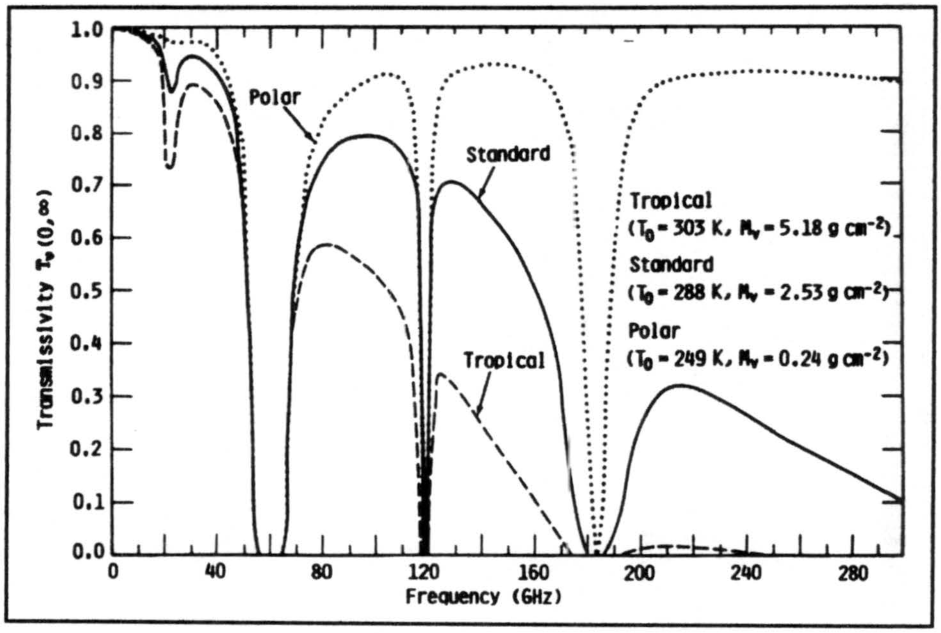

Figure 2.2: Atmospheric transmittivity as characterized by different surface temperatures T_0 and integrated water vapor content M_v (from Ulaby, 1981).

This work will be concerned primarily with the atmospheric window that includes 85.5 GHz, and uses the transmittance form of the radiative transfer equation.

2.1 Transmittance Form of the Microwave Radiative Transfer Equation

The upwelling intensity at the top of the atmosphere can be expressed by the transmittance form of the integrated radiative transfer equation at frequency ν for both the vertical and horizontal polarization

$$
\begin{aligned}
I_\upsilon(0) &= \varepsilon_\upsilon B_\upsilon(T_s)\tau_\upsilon(p_s,0) \\
&+ \int_{p_s}^{0} B_\upsilon[T(p)]\frac{\partial \tau_\upsilon(p,0)}{\partial p}dp \\
&+ (1-\varepsilon_\upsilon)[\tau_\upsilon(p_s,0)]^2 \int_{p_s}^{0} \frac{B_\upsilon[T(p)]}{[\tau_\upsilon(p,0)]^2}\frac{\partial \tau_\upsilon(\pi,0)}{\partial p}dp \\
&+ (1-\varepsilon_\upsilon)[\tau_\upsilon(p_s,0)]^2 B_\upsilon(T_{space})
\end{aligned} \tag{2.1}
$$

where ε is the surface emissivity, B_v is the Planck function, T_S is the surface skin temperature, τ_v is the total transmittance of the atmosphere, p is the pressure, and T_{space} is the cosmic background temperature. The first term in equation 2.1 is the emission from the surface attenuated by the atmosphere, the integral terms are the direct contribution from the atmosphere, and the contribution reflected by the surface; and the last term is the radiation from space reflected by the surface. As we can see, the radiance is a function of surface skin temperature, surface emittance, the atmosphere's transmittance, which is a function of the temperature and moisture profile, and the deep space emission temperature. Since the deep space emission temperature is small ($T_{space} \sim 2.7K$) in comparison to the atmospheric emission temperature above 5 GHz, it is usually neglected, but is presented here for completeness. The radiometer views emission from the atmosphere, surface, and from reflected emission (Figure 2.3).

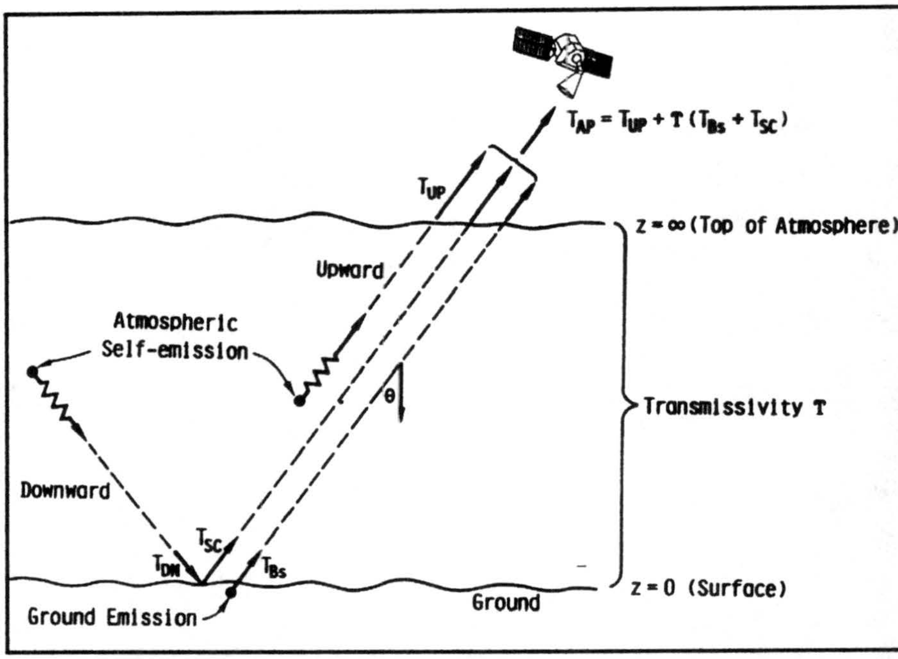

Fig. 2.3: Satellite-borne radiometer observing the earth at a nadir angle θ (from Ulaby, 1981).

The surface term is a function of the surface skin temperature, surface emissivity, wavelength, and the pressure. The microwave radiative transfer equation in equation 2.1 incorporates the Rayleigh-Jeans limit, and further assumes that the atmosphere is a non-scattering, plane-parallel atmosphere with a non-blackbody, surface boundary condition.

2.1.1 Rayleigh-Jeans Limit

The typical cloud drop sizes for non-precipitating clouds are less than 20 μm. In these cloud types, absorption or emission effects and the transmissivity of cloud liquid water is strongly linked to the cloud water vertical distribution and the atmospheric temperature profile (Diak, 1995). The representative droplet size distributions are shown in figure 2.4 (Liou, 1992) and Table 2.1 (Liou, 1992) for selected cloud types. Fair weather cumulus has a narrow droplet size distribution with the largest radius at about 20 μm and a mean radius near 4 μm. Cumulus congestus droplet radius is generally less than 20 μm, but can extend up to 40 μm. Cumulonimbus has a much broader droplet size distribution that extends to a radius of 70 μm. Both stratocumulus and stratus (over land) exhibit droplet radii ranges well under 20 μm. Mean droplet size data from Stephens (1994) indicates a higher mean radius, near 20-24 μm for cumulus congestus and cumulonimbus with maximum radius closer to 100 μm.

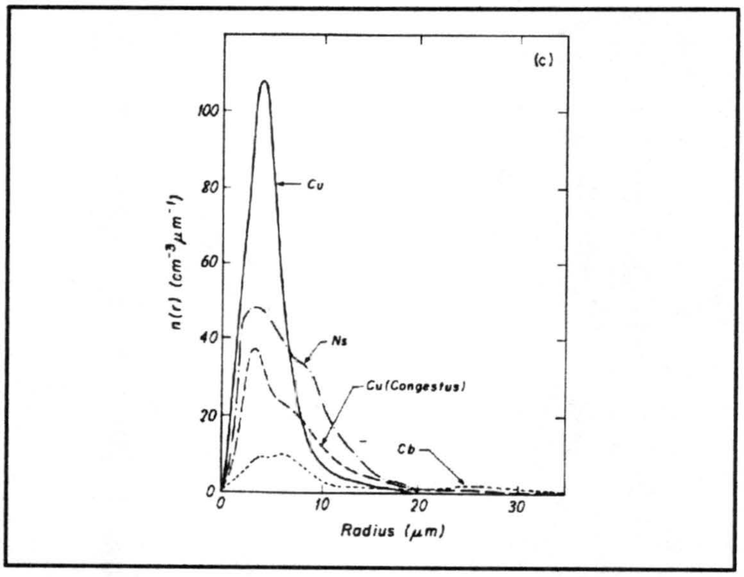

Fig. 2.4: Droplet size distribution of fair weather cumulus, nimbostratus, cumulus congestus, and cumulonimbus (from Liou, 1992).

	Cloud Type	Investigator	N (cm^{-3})	r_m (μm)	Δr (μm)	LWC ($g\,m^{-3}$)
Low clouds	St I (ocean)	Neiburger	464	3.5	0–16	0.24
	St II (land)	Diem	260	4.5	0–20	0.44
	Sc	Diem	350	4.0	0–12	0.09
	Ns	Diem	330	4.0	0–20	0.40
Middle clouds	As	Diem	450	4.5	0–13	0.41
	Ac	aufm Kampe and Weickmann	—	5.0	0–12	—
Cumulus	Cu (fair weather)	Battan and Reitan	293	4.0	0–20	0.33
	Cu (congestus)	Durbin	207	3.5	0–40	0.66
	Cb	Weickmann and aufm Kampe	72	5.0	0–70	2.50

Table 2.1: Characteristics of the droplet size distribution for various cloud types (from Liou, 1992).

Therefore the low-frequency limit where hν << kT follows, and the Planck function can be approximated as

$$B_\upsilon(T) \approx \frac{2\upsilon^2 kT}{c^2} = \frac{2kT}{\lambda^2} \qquad (2.2)$$

where λ is the wavelength. Note the linear relationship of the Planck function with the physical temperature. This allows the intensity to be scaled as

$$T_b(\upsilon) \equiv \frac{\lambda^2}{2k} I_\upsilon \qquad (2.3)$$

This expression defines the Rayleigh-Jeans equivalent brightness temperature and which is the intensity in the radiative transfer equation (RTE) but has been dimensionally scaled to give units of degrees Kelvin. This definition is not an approximation in itself (Janssen, 1993). The solution of the RTE can be rewritten as

$$T_b(\upsilon) = T_{b0}(\upsilon) e^{-\tau(s0)} + \int^{s_0} \frac{T(s)}{\Re(\upsilon, T_s))} e^{-\tau(s)} \alpha ds \qquad (2.4)$$

where the background brightness temperature T_{b0} is derived from our general boundary condition as

$$T_{b0} = \frac{\lambda^2}{2k} I_\upsilon(s_0) \qquad (2.5)$$

The factor

$$\Re(\upsilon, T) = \frac{2kT}{\lambda^2} \frac{1}{B_\upsilon(T)} = \frac{kT}{h\upsilon}(e^{h\upsilon/kT} - 1) \qquad (2.6)$$

can be seen to be just the ratio of the physical temperature T of a blackbody emitter to its brightness temperature T_b, namely,

$$\Re(\upsilon, T) = \frac{T}{T_b} \qquad (2.7)$$

Expanding $\Re$ (ν, T) in terms of $h\nu/kT$, we have

$$\Re(\upsilon, T) = 1 + \frac{1}{2!}\left[\frac{h\upsilon}{kT}\right] + \frac{1}{3!}\left[\frac{h\upsilon}{kT}\right]^2 + \ldots \qquad (2.8)$$

where we see that $\Re$ is always greater than unity, and approaches unity in the Rayleigh-Jeans limit (Janssen, 1993).

Equation 2.4 is exact as far as the Planck law is concerned. The Rayleigh-Jeans approximation is incorporated by setting $\Re=1$, giving

$$T_b(\upsilon) = T_{b0} e^{-\tau(s)} + \int_0^{s_0} T(s) e^{-\tau(s)} \alpha \, ds \qquad (2.9)$$

This is the form of the radiative transfer equation commonly used in microwave remote sensing. It is more accurate than one would expect at first glance; if one assiduously holds to the Rayleigh-Jeans approximation to include the calibration of a radiometer against blackbody targets, then this equation is actually correct to the first order in $h\nu/kT$

in spite of having neglected this and all higher orders when we chose $\Re=1$ (Janssen, 1993).

Equation 2.9 is a simple weighted average over the physical temperature of an atmosphere. The emission $\alpha T\ ds$ from each element is attenuated by a factor $e^{-\tau}$ by the intervening medium as it travels toward the point of measurement. The sum of these contributions represents an average temperature along the propagation path weighted at each point by $\alpha e^{-\tau}$. The radiative transfer equation expresses the forward problem: if the absorption and temperature are known along the path of propagation, then the brightness temperature can be computed from this equation (Janssen, 1993).

The simple form of the RTE given by Eq. 2.9 can be used for most applications without concern for the errors introduced by either the Rayleigh-Jeans approximation or the neglect of scattering. Deviations from the Rayleigh-Jeans approximation become more important as microwave remote sensing is extended to higher frequencies, and as applications at all frequencies become more exacting. Also, whereas typical cloud particles are not significant microwave scatterers, rain is, and is encountered frequently in tropospheric remote sensing. These approximations are no longer valid when the cosmic microwave background is present either as a cold-temperature reference or as the background term T_{b0}.

2.1.2 Non-Scattering Atmosphere

The total power lost from the path of propagation due to scattering must be small compared to that involved in absorption or emission, and this depends on the case. Specifically, let us consider scattering unimportant if the power lost from the beam due to scattering in each volume element is small compared to the power absorbed in that element, or, more conservatively, if the ratio of the scattering to absorption cross-section Q_s/Q_a is small for the scattering particles involved. If we consider that the reemitted power will be comparable to that absorbed, then the net fraction of the total radiance due to scattering that is ultimately measured will then be less than or equal to this ratio. This is particularly true if there are other sources of absorption involved, and the condition can be overly conservative in some cases.

The condition is meaningful when considering liquid water, a strong microwave absorber that tends to dominate the radiative transfer process when it's present in even modest amounts in the form of clouds or rain.

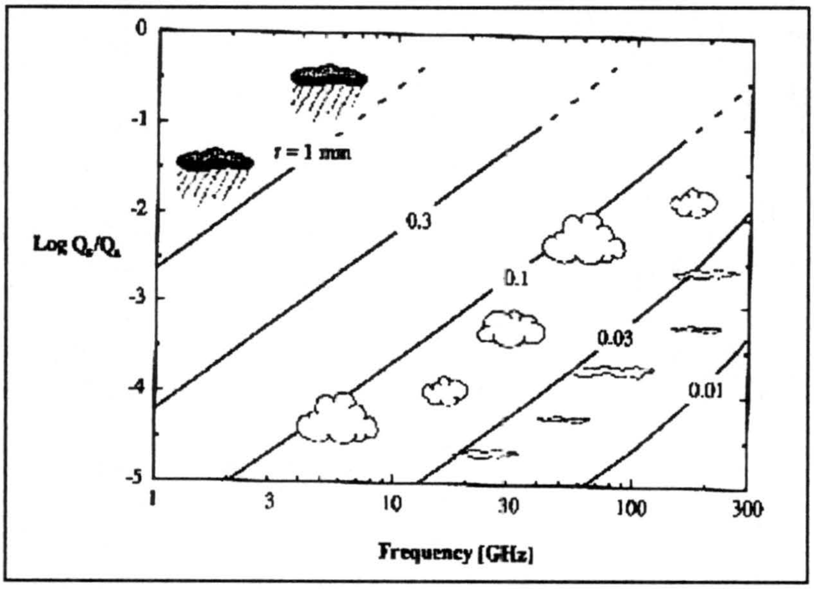

Figure 2.5: Ratio of scattering to absorption cross-section for water spheres of radius r. Typical droplet-size ranges are indicated for clouds with and without rain (from Janssen, 1993)

In the figure above (Janssen, 1993), we show the ratio Q_s/Q_a for single spherical water droplets of radius r that have been calculated using the frequency-dependent dielectric constant of water at a nominal temperature of 10° C. The solid portions of the curves indicate the region where the Rayleigh scattering criterion $2\pi r << \lambda$ is valid, and the dashed upper region indicates the transition to the Mie scattering regime.

The upper limit for cloud droplet radii in the atmosphere is around 0.1 mm (100 μm). Thus, at the frequencies commonly used for remote sensing of the troposphere--about 20-90 GHz--absorption in liquid water cloud regions exceeds scattering by at least two orders of magnitude, and we would expect errors to be comfortably less than 1 % if we neglect scattering in the retrieval temperatures in this frequency regime. When cloud droplets coalesce to form rain, on the other hand, the resulting particle sizes approach the wavelength at all microwave frequencies. Drop-size distributions are highly variable, with the mean drop radius tending to increase with rain rate--from 0.5 to 1.5 mm (500 to1500 μm) for light to heavy rainfall, well into the Mie regime (Janssen, 1993).

2.1.3 Plane-Parallel Approximation

The plane-parallel assumption is commonly employed in satellite meteorology. The distance along the atmosphere path ds is related to the vertical depth dz by

$$ds = \sec\theta dz$$

where θ is the satellite zenith angle of incidence at the surface as measured from the vertical. Figure 2.6 is a diagram of the plane-parallel atmosphere. By making this assumption, the temperature and absorption coefficients are functions of height (vertical coordinate z) only. It follows that the intensity is a function of the vertical position and zenith angle.

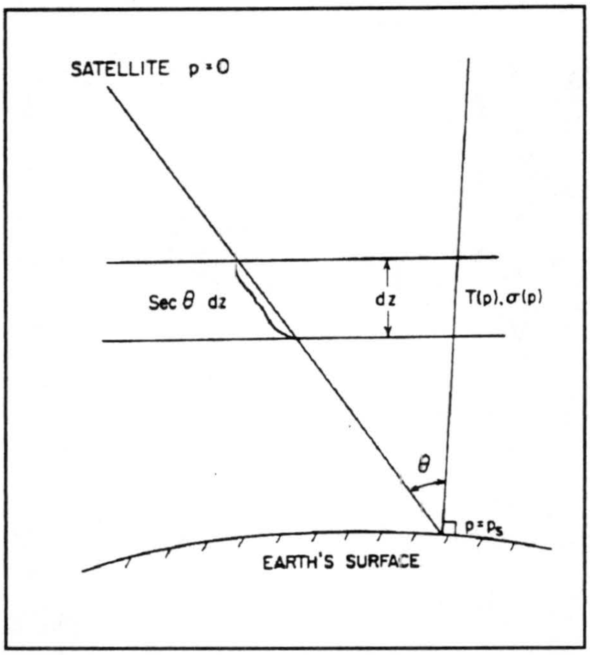

Figure 2.6: Plane-parallel geometry (Jones, 1988).

2.1.4 Non-Blackbody Surface Boundary Condition

In the microwave region of the spectrum, the surface does not emit as a blackbody but rather as a gray body. The surface in this case emits less than a blackbody and does not necessarily absorb all the energy incident upon it. An electromagnetic wave incident upon a surface boundary can be described by the reflectance, absorptance, and transmittance. These quantities must sum to one to assure conservation of energy. Surface emittance, ε_ν, is a quantity related to the reflectance and is described as the ratio of the observed brightness temperature to the brightness temperature of an ideal blackbody in thermodynamic equilibrium,

$$\varepsilon_{\upsilon} = \frac{T_{MW}}{\overline{T}_{BB}} \qquad (2.9)$$

In addition, if the surface is considered opaque, then the surface emittance is directly related to absorption. The other component of the radiance at the surface is due to reflected radiation from above the surface. The deep space emission due to cosmic background radiation, another component of surface radiance, is neglected because of its small relative contribution to the total upwelling radiance.

2.2 Atmospheric Effects

2.2.1 Gaseous Absorption

Microwaves have a wide range of behavior at different spectral regions. In the lower frequencies, 1-15 GHz, the atmosphere is transparent even to clouds and moderate rain rates, but in higher frequencies (> 15 GHz) molecular absorption bands become more prominent and the atmosphere becomes more opaque to microwave radiation. The main gaseous constituents attenuating the radiation are oxygen and water vapor. Water vapor is highly variable and is concentrated at the lowest levels of the atmosphere with attenuation increasing for increasing amounts of water vapor at a given temperature and pressure.

The window regions of the microwave spectrum are not true windows, and the window in which the TRMM 85.5 GHz channel resides has more attenuation than the 22.235 GHz water vapor absorption line. The low frequencies in the 1-10 GHz range have low spatial resolution and are used mainly for estimating land and ocean surface parameters due to their ability to penetrate clouds and most vegetation.

2.2.2 Absorption by Hydrometeors

Spherical particles can absorb and scatter microwave radiation and the complete solution for a single particle of radius r can be represented by the scattering, absorption, and extinction cross-sections, A_s, A_a, A_e. A representative volume in an atmosphere can contain several particles of different sizes, which interact with the electromagnetic radiation. The combined effects of the particles in the volume can be represented by the volume absorption coefficient,

$$\sigma_a = \int_0^\infty n(r) A_a(r) dr, \tag{2.10}$$

where n(r) is the drop-size distribution, and r is the particle radius.

There are two alternatives at this point, one is to assume that the particles are relatively small and make the Rayleigh approximation, and the other is to consider the particles large enough to require the full Mie equations. Of considerable convenience is the natural size differential of cloud droplets and precipitation, which enables atmospheric liquid water to be divided into two classes: non-precipitating clouds and precipitating clouds (Deirmendjian, 1963). Assuming non-precipitating clouds allows the application of the Rayleigh approximation for the TRMM frequencies. This yields,

$$\sigma_a = \frac{8\pi^2}{\lambda_b} \mathrm{Im}\{-K\} \int_0^\infty p(r) r^3 dr, \tag{2.11}$$

and since the cloud water content in the volume is given by,

$$m_{\upsilon} = \frac{4\pi\rho_L}{3}\int_0^{\infty} p(r)r^3 dr, \tag{2.12}$$

$$\sigma_a = \frac{6\pi}{\lambda_b \rho_L} \mathrm{Im}\{-K\} m_{\upsilon}. \tag{2.13}$$

where ρ_L is the water density, the volume absorption coefficient is directly related to cloud water content,

$$\sigma_a = \frac{6\pi}{\lambda_b \rho_L} \mathrm{Im}\{-K\} m_v. \tag{2.14}$$

The absorption coefficient is not a function of the droplet size distribution in the Rayleigh limit, and allows the calculation of the absorption coefficient with a more convenient parameter, liquid water content (Westwater, 1972).

However, the full Mie theory must be used for precipitation-sized particles. When scattering processes are included, the high frequency channels such as the 85.5 GHz channel can have brightness temperatures well below their actual thermal temperature as shown by Wu and Weinman (1984) using their radiation model in Figure 2.7. This is due to the scattering of cold deep space radiation by the large precipitation sized particles into the satellite's sensor. Brightness temperatures at 85.5 GHz can be as low as 100 K, which represents a dynamic range of approximately 200 K.

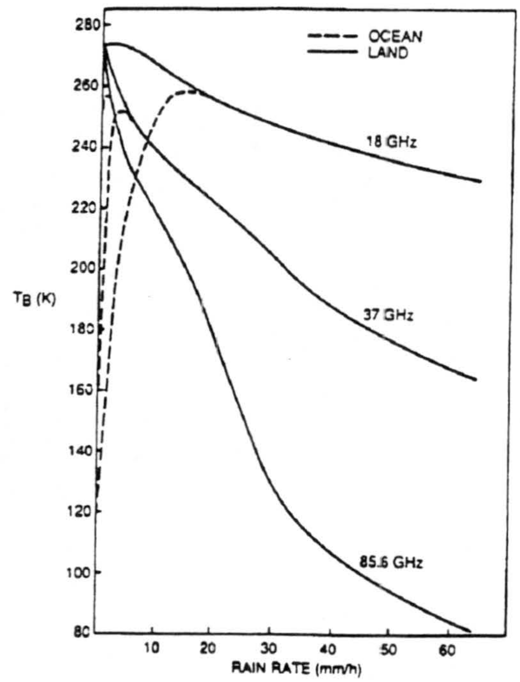

Figure 2.7: Brightness temperature – rain rate relationships at 18, 37, and 85 GHz from radiative transfer modeling of Wu and Weinman (1984).

The most responsible component for the large scattering effects are ice particles in the higher levels of the precipitating clouds. Figure 2.8 from Spencer et al. (1989) shows that ice and water have comparable volume scattering coefficients but that ice has negligible volume absorption compared to water which is the cause of the significantly higher single scatter albedo of ice than for water.

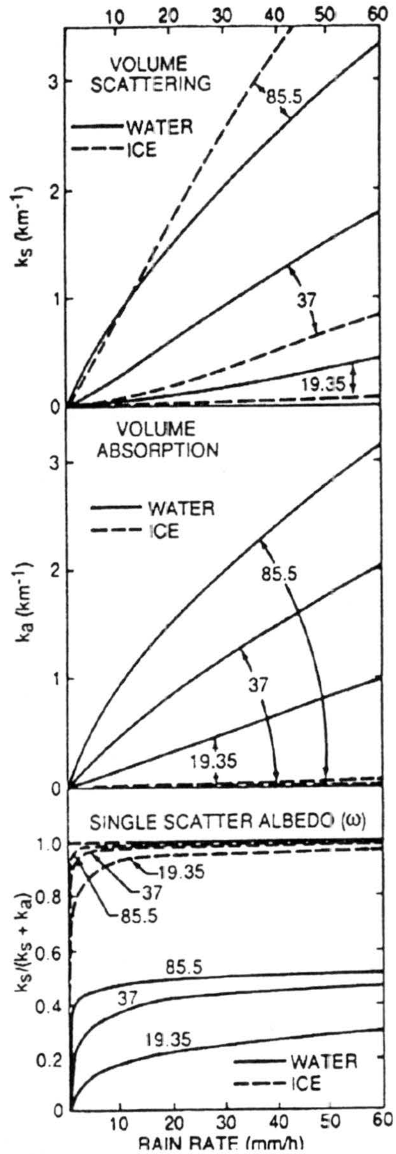

Figure 2.8: Mie volume scattering coefficients (top), volume absorption coefficients (middle), and single scattering albedos (bottom) for a Marshall-Palmer precipitation size distribution of water and ice spheres at three frequencies (GHz) (Spencer et al., 1989).

2.3 Surface Effects and Polarization

A key to understanding microwave remote sensing techniques is to realize that the surface emittance can vary depending on the electromagnetic properties of the surface. For land the surface emittance varies due to soil moisture content and can range from near unity for dry soils to less than 0.6 for wet soils (Wang and Schmugge, 1980;

Schmugge, 1985). As mentioned before, passive microwave remote sensing of the atmosphere over a land surface is a challenge due to the complex soil and vegetation characteristics, and difficulty in retrieving cloud variables.

Ulaby (1986) calculated the brightness temperature for three moisture conditions (Fig. 2.9), and showed the significant changes in brightness temperature that can occur when soil is wetted for a 52.8° angle of incidence. There is a sharp divergence of the horizontal and vertical polarization brightness temperatures when the angle of incidence is greater than 10 degrees, and for 52.8 degrees there is a near 100 K brightness temperature difference.

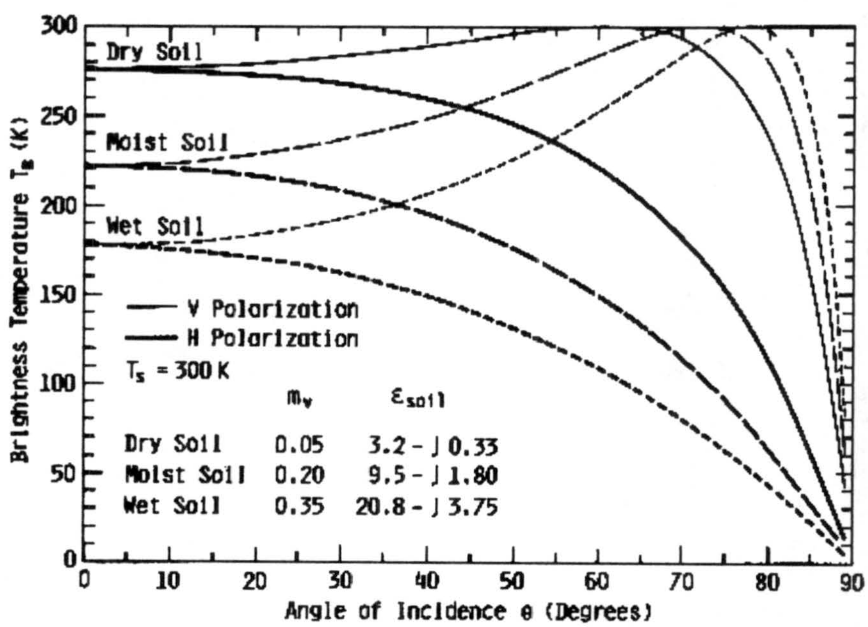

Fig. 2.9: Calculated brightness temperature for a homogeneous soil medium with a specular surface at three moisture conditions (Ulaby, 1986). Horizontal polarization is shown in thicker, bolder line.

Polarization of electromagnetic radiation is another surface effect and is of primary importance in the Normalized Polarization Difference (NPD) method since it is the depolarization of microwave radiation that is essential in identifying clouds and cloud liquid water. Reflection varies widely for natural surfaces and is dependent on wavelength, angle of incidence, angle at which the surface is viewed from space, and the physical characteristics of the surface itself. There are two distinct processes responsible for the reflection of radiation at the earth's surface.

The first is specular (mirror-like) reflection and the second is diffuse reflection (i.e., from a rough surface). Real reflection from the earth's surface is composed of both diffuse and specular reflection; however, diffuse reflection is usually taken to be unpolarized according to Lambert's law, regardless of the state of polarization of the incident radiation. Specular reflection is similar to the glare off a table. The reflected light is polarized preferentially in the horizontal due to the horizontal polarization's higher reflectance. The reflectance of an electromagnetic wave by a specular dielectric surface is given by the square of the magnitude of the Fresnel reflection coefficients (Reitz et al., 1979)

$$\rho_h = \left| \frac{\cos\theta - \sqrt{\varepsilon - \sin^2\theta}}{\cos\theta + \sqrt{\varepsilon - \sin^2\theta}} \right|^2, \tag{2.15}$$

for horizontal polarization and,

$$\rho_v = \left| \frac{\varepsilon\cos\theta - \sqrt{\varepsilon - \sin^2\theta}}{\varepsilon\cos\theta + \sqrt{\varepsilon - \sin^2\theta}} \right|^2, \tag{2.16}$$

for vertical polarization, where θ is the angle of incidence and ε is the relative complex dielectric constant for the two mediums. Recalling that $\varepsilon = 1 - \rho$, then the surface emittance must also have different values for each polarization, with the vertical polarization surface emittance generally greater than the horizontal polarization.

Among the most important properties influencing the dielectric constant for land surfaces is soil moisture. An increase in the dielectric constant corresponds to a decrease in the surface emittance. Soil depth penetration by the electromagnetic radiation has been theoretically (Wilheit, 1978b) and experimentally (Newton et al., 1982) determined to be on the order of a few tenths of a wavelength. Application to the TRMM instrument frequencies show that the effective surface emittance is from the top 1 cm of the soil and is therefore sensitive to surface soil moisture and not sub-surface soil moisture.

Other influences on the surface emittance are surface roughness, and non-homogeneity of the surface, which can be due to vegetation, terrain, etc. for land surfaces (Choudhury et al., 1979; Schmugge et al., 1980). For a specular surface the reflected electromagnetic radiation is entirely coherent and obeys Snell's Law of $\theta_i = \theta_r$, so that the angle of incidence equals the angle of reflection. As the surface becomes rougher the scattering due to the surface has a larger diffuse component in addition to the coherent reflection.

Chapter 3

Data

3.1 TRMM Data Format

The Tropical Rainfall Measuring Mission (TRMM) data was provided to Colorado State University by the National Aeronautical Space Administration (NASA). The TRMM datasets are in the Hierarchical Data Format (HDF). HDF was designed by NCSA to address many requirements for storing scientific data, i.e., support for types of data and metadata commonly used by scientists, efficient storage of and access to large data sets, platform independence, and extensibility for future enhancements and compatibility with other standard formats. The primary HDF data structures are Scientific Data (multi-dimensional arrays), Vdata (tables of integers, floats, and characters), Raster Images, Annotation, and Palette [A sixth, the vgroup object, does not contain data and is designed for the purpose of grouping the other five primary data objects within an HDF file]. HDF is more than a file format, it also consists of supporting software that make it easy to store, retrieve, visualize, analyze, and manage data in HDF files. HDF files that contain more than one data element are generally easier to work with when the data objects containing related data are grouped together.

The TMI and VIRS swath data is organized in Vgroups. Each Vgroup has a tag number (Tag), a reference number (Ref), and a classification (Class, i.e., SwathData). There are a number of Vgroup Interface Routines used to access the HDF files.

The TMI and VIRS data were essentially translated from this HDF format into what is called the HDFEOS format. The HDFEOS format has a more rigid structure; however, it is easier to merge different datasets, like the TMI and VIRS datasets. This merging of datasets in HDF is difficult, since the code is specific to each sensor. Additionally, HDF would require a separate remapping program for each sensor while with HDFEOS you only need one remapping program to handle both VIRS and TMI. This greatly simplified the programming of the algorithms that use both the VIRS and TMI datasets simultaneously, where both datasets are remapped to the same projection.

The global TRMM data was accessed, calibrated, and sectorized into a much more manageable southwest US sector using the Data Processing and Error Analysis System (DPEAS) (Jones and Vonder Haar, 2001). DPEAS was used to merge the TMI and VIRS data. Now the data is available in the HDFEOS structure, which allows for much simpler processing and future manipulation.

3.2 TRMM Microwave Imager (TMI) Description

The TMI is a nine-channel passive radiometer based on the Special Sensor Microwave/Imager (SSM/I), which has flown on the Defense Meteorological Satellite Program (DMSP) since 1987 (Kummerow, 1998). TRMM was launched in November of 1997 into a circular orbit, at an altitude of 350 km. Because of this low orbit, the TMI provides much improved spatial resolution over its predecessor, the Special Sensor Microwave/Imager (SSM/I), on which its design is based.

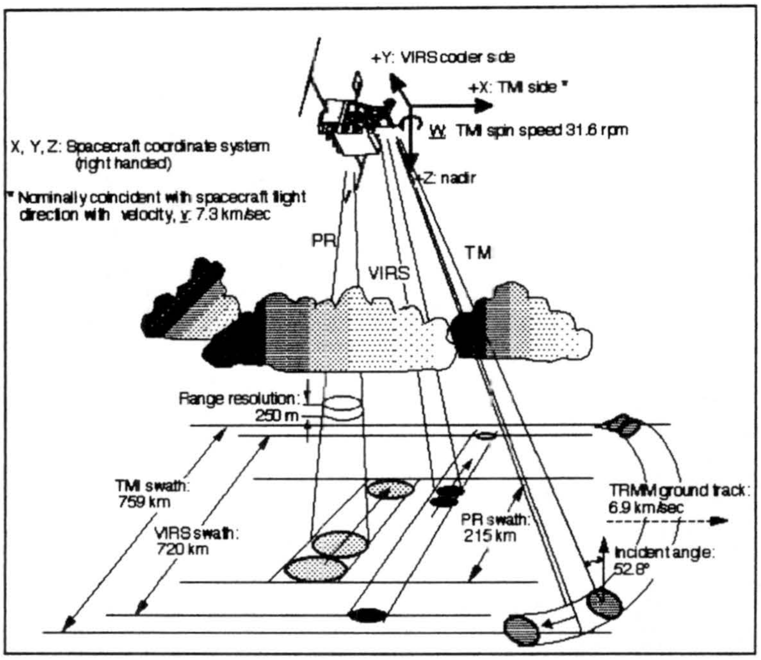

Figure 3.1: TMI conical scanning geometry (Kummerow, 1998).

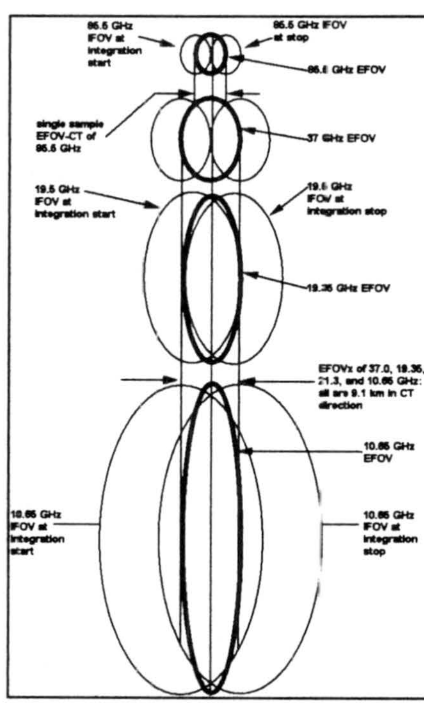

Figure 3.2: TMI field of view (FOV) (Kummerow, 1998).

TRMM's orbit inclination of 35° provides extensive coverage in the tropics, from approximately 36°-latitude north to 36°-latitude south. The TMI has 5 frequencies and dual polarization (see Table 3.1). The data are collected during the forward 130° portion of the instrument rotation that results in a conical scanning pattern that yields a swath width of 758.5 km. The conical scanning pattern has a constant satellite zenith angle of 52.8° (Fig. 3.1), eliminating changing limb effects due to varying zenith angle. The effective ground resolution of the 85.5 GHz data is 5 km x 7 km with 1 sample per beam width.

Table 3.1. TMI Instrument Characteristics

Channel Number	Frequency GHz	Polarization H or V	Effective Field of View,* km	Sensitivity (NEΔT),† K	Accuracy, K
1	10.65	V	63 x 37	0.63	1.5
2	10.65	H	63 x 37	0.54	1.5
3	19.35	V	30 x 18	0.50	1.5
4	19.35	H	30 x 18	0.47	1.5
5	21.3	V	23 x 18	0.71	1.5
6	37.0	V	16 x 9	0.36	1.5
7	37.0	H	16 x 9	0.31	1.5
8	85.5	V	7 x 5	0.52	1.5
9	85.5	H	7 x 5	0.93	1.5

Adapted from *Kummerow et al.* [1998].
* Using a 3-dB limit.
† Average of laboratory measurements.

The TMI data used is level 1B, which are calibrated brightness temperatures (using onboard calibration data). Each scan line consists of latitude and longitude values along with brightness temperatures for the 208 Effective Fields of View (EFOVs) at 85.5 GHz.

3.3 TRMM Visible Infrared Sounder (VIRS) Instrument Description

The VIRS is a five-channel imaging spectro-radiometer with bands in the wavelength range from 0.6 to 12.0 μm. It is similar to the Advanced Very High Resolution Radiometer (AVHRR) that has flown since 1978 on the National Oceanic and Atmospheric Administration (NOAA) series of spacecraft in that both have the same center wavelengths and bandwidths (Kummerow, 1998).

This work will use the 10.8 μm channel data to determine the surface skin temperature. The 10-12 μm band is the most suitable channel for determining the surface temperature by space remote sensing, since it is situated in the atmospheric window and the relative emissivity of surfaces in this interval is comparatively stable and close to unity. Radiation from the earth's surface can be considered blackbody radiation and is a function of the surface temperature and the wavelength.

3.4 Co-Location of Satellite Data Sets

A Windows NT data fusion method based on Jones et al.'s (1995) PORTAL (Polar Orbiter Remapping and Transformation Application Library), was created to re-map and co-locate measurements from the TMI and VIRS instruments into TMI projection. This method maintained the full resolution of the satellite measurements while reducing the overall computational requirements of the retrieval methods. Data was binned into approximately 15 km x 15 km grids.

Chapter 4

Measurement of Effective Surface Emittance

4.1 Surface Emittance Retrieval Procedure

The instantaneous microwave surface emissivities were calculated according to the alternative procedure in Jones and Vonder Haar (1997) without an atmospheric correction.

4.1.1 Cloud Discrimination

Cloud-free areas were determined using a conservative threshold IR skin temperature of 295 K. Areas where the skin temperature was greater than 295 K were assumed cloud-free. This conservative threshold was key in creating a cloud-free, surface emissivity background, in which to view cloud properties and their associated polarization signal over the background emissivity composite. Microwave surface emittance is only calculated for clear-sky conditions since clouds can have a measurable impact on the observed microwave brightness temperatures (Jones and Vonder Haar, 1990; Greenwald, 1997).

4.1.2 Surface Emittance Calculation

This procedure uses a simple effective microwave surface emittance concept where it is assumed that the infrared brightness temperature is a close approximation to the actual blackbody temperature (Ulaby et al., 1986),

$$\varepsilon_k = \frac{TB_{MW}(k)}{TB_{IR}(k)}, \qquad 4.1$$

where $TB_{MW}(k)$ and $TB_{IR}(k)$ are the microwave and mean infrared brightness temperatures for the TMI channel k. The mean infrared brightness temperature was estimated using the infrared (10.8 μm) data from the TRMM Visible/Infrared Sounder (VIRS) data. The infrared brightness temperature closest to the center of the microwave EFOV was used as an approximation. For the southwest US in summer, this should be a fairly good approximation for a weighted average, however, it does not address the differences in topography and the sensor resolution differences. Error involved in this assumption was estimated by measuring the horizontal variability of the infrared brightness temperature (Table 5.3) over a 5 x 5 grid (about 75 x 75 km area) with relative uncertainty less than 3% at all sites. The coincident TMI 85.5 GHz brightness temperatures were used along with the surface skin temperatures to calculate the instantaneous surface emissivities (effective surface emissivity), which were then gridded and combined into ten-day composites. The data was binned into approximately 15 km x 15 km grid boxes, and a 90-day surface emissivity composite was calculated for the period of June 1, 1998 to August 29, 1998. From these clear sky effective surface emissivity composites, the emissivity differential (Δε) was determined.

One of the primary error sources involved in this procedure arises from the uncorrected atmosphere. Work by Jones and Vonder Haar (1997) showed that the 85.5 GHz channel is more sensitive to water vapor than the lower frequencies (Fig. 4.1). Therefore, at 85.5 GHz the atmospheric correction is a strong function of the effective microwave surface emittance value, with the atmospheric correction becoming larger with lower effective microwave surface emittance values. This result is expected since the low effective microwave surface emittance regions are areas with higher microwave reflectivity and this amplifies the water vapor effect of the atmosphere (Jones, 1997).

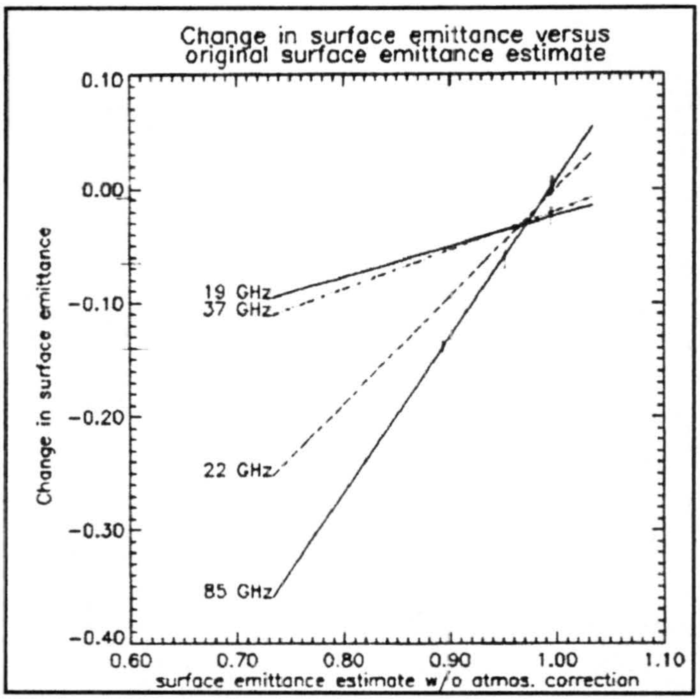

Figure 4.1: Change in the surface emittance versus the effective surface emittance estimate using a standard midlatitude summer sounding (from Jones and Vonder Haar, 1997).

Figure 4.2 indicates an atmospheric correction of 3.5% at 85.5H GHz. A larger atmospheric correction is present for the horizontal polarizations than for the vertical polarizations, as would be expected from their lower effective microwave values (see Figure 4.1) (Jones and Vonder Haar, 1997). This shows the change in the surface emittance versus the effective surface emittance using a standard midlatitude summer sounding at various microwave frequencies. For surface emittances without an atmospheric correction ranging from 0.90 to 1.00, which sufficiently covers the emittances in the study, the change begins at approximately –0.14 and decreases to –0.01 for a 1.00 uncorrected surface emittance.

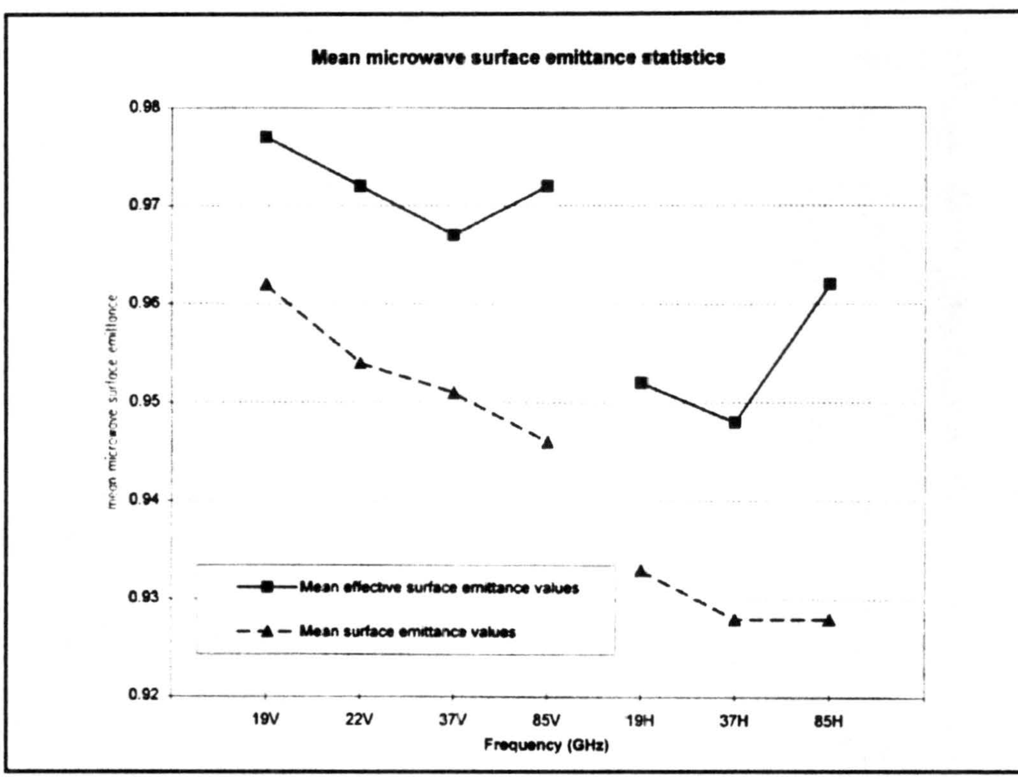

Fig. 4.2: Mean microwave surface emittances for July 30 to October 7, 1991. The effective microwave surface emittance does not include an atmospheric correction (Jones, 1997).

4.2 Results

4.2.1 Composite Surface Emittance

The effective surface emittance was calculated over an approximate 90-day period from 1 June 1998 to 30 August 1998 over the Southwestern United States. Specifically, the focus area was bounded by 20-40 degrees north latitude and 90-120 west longitude. Specific sites were chosen (see the Table 4.1 below) based on location and availability of corresponding surface synoptic data for the period.

The effective surface emittance has been estimated during clear-sky conditions. Improved surface temperature measurements are available from the infrared channels during clear-sky conditions, thus the surface emittance measurements are more accurate than can be measured during cloudy conditions. However, the assumption is made that the surface emittance measurements during an earlier time period are representative of the surface when clouds move into the instrument field of view (FOV) at a later time.

From the surface emittance measurements it appears that fast changes on a day-to-day time scale in surface emittance are due to precipitation events and not to drying or vegetation changes. Also, since the 85.5 GHz channels are more sensitive to cloud liquid water than previously used microwave channels, surface effects become less important as the cloud liquid water increases and the atmospheric attenuation obscures the ground from view of the sensor (Jones, 1990). The spatial resolution of the TRMM 85.5 GHz channel is also much better at the higher frequencies than the SSM/I. This allows for improved estimates of the horizontal variability of cloud liquid water.

4.2.2 General Terrain Characteristics (from an Effective Surface Emissivity Viewpoint)

The horizontal polarization shows surface water effects more readily than the vertical polarization since there is a larger dynamic range of microwave surface emittances for the horizontal polarization. The microwave surface emittances range from about 0.5 for large water bodies to near 1.0 for the most arid or heavily vegetated regions (Jones, 1997).

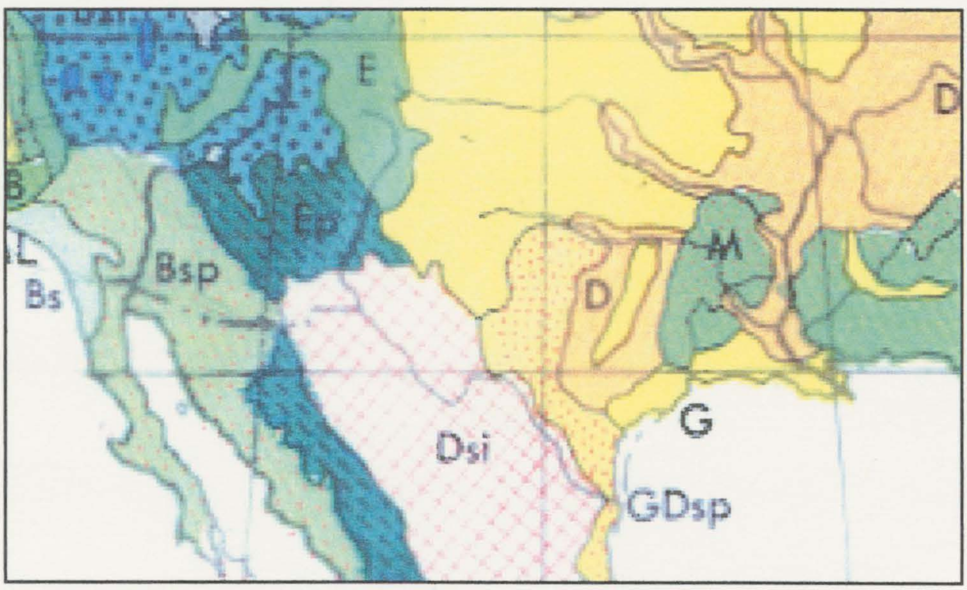

Fig 4.3: General vegetation characteristics over the SW United States (from Goode's World Atlas).

Type	Vegetation Characteristic
Dsi	Broadleaf Deciduous. Plants apart > 3 ft
Ep	Needleleaf Evergreen Trees (Coniferous), growth singly or in groups or patches
Bsp	Broadleaf Evergreen (Coniferous), dwarf shrubform, maximum height 3 feet, growth singly or in groups or patches
G	Grass and other herbaceous plants
GDsp	Grass and other herbaceous plants. Broadleaf deciduous, shrubform, minimum height 3 feet, growth singly or in groups or patches
Bzi	Broadleaf evergreen (Coniferous), dwarf shrubform, maximum height 3 feet, plants sufficiently far apart that they frequently do not touch
E	Needleleaf evergreen trees (Coniferous)

Table 4.1: Figure 4.3 vegetation abbreviations and vegetation characteristics.

Lakes and large rivers are the most prominent feature of the microwave surface emittance results in Figures 4.4 and 4.5. The polka dot pattern (especially in the east Texas, east Oklahoma, and Ozark regions) is due to smaller lakes that have partial footprint coverage (lakes about 5-10 km in size) (Jones, 1997). Non-lake features are also prevalent in the figures. These include deserts, irrigation areas, heavy crop regions, and coniferous forests and temporal surface wetness signatures.

The desert regions in parts of Arizona and New Mexico show rather low microwave surface emittances over a broad region. The desert regions have low microwave surface emittances due to a combination of effects such as the generally higher dielectric constant of rock materials (Ulaby et al., 1986 and Jones, 1997), in addition to enhanced surface-scattering properties [Grody, 1991]. Since the material has a high dielectric constant, it also acts in a manner similar to water (another material with a high dielectric constant).

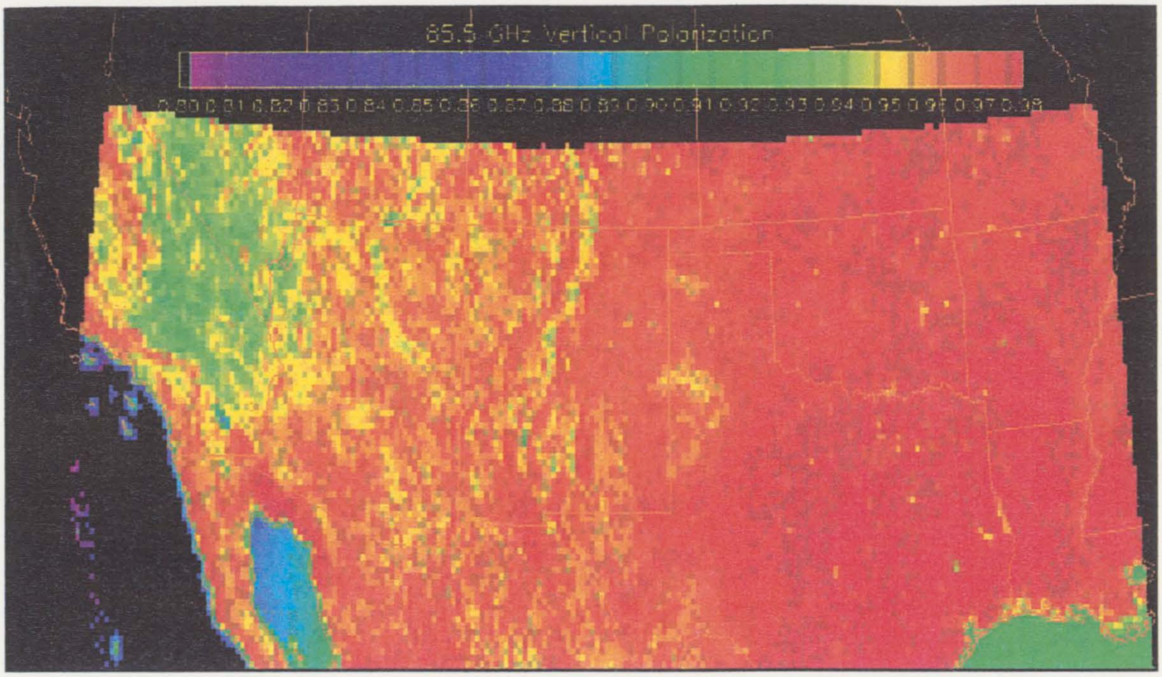

Fig. 4.4: TRMM 85.5 GHz vertical polarization effective surface emissivity composite from 1 Jun to 31 August 1998.

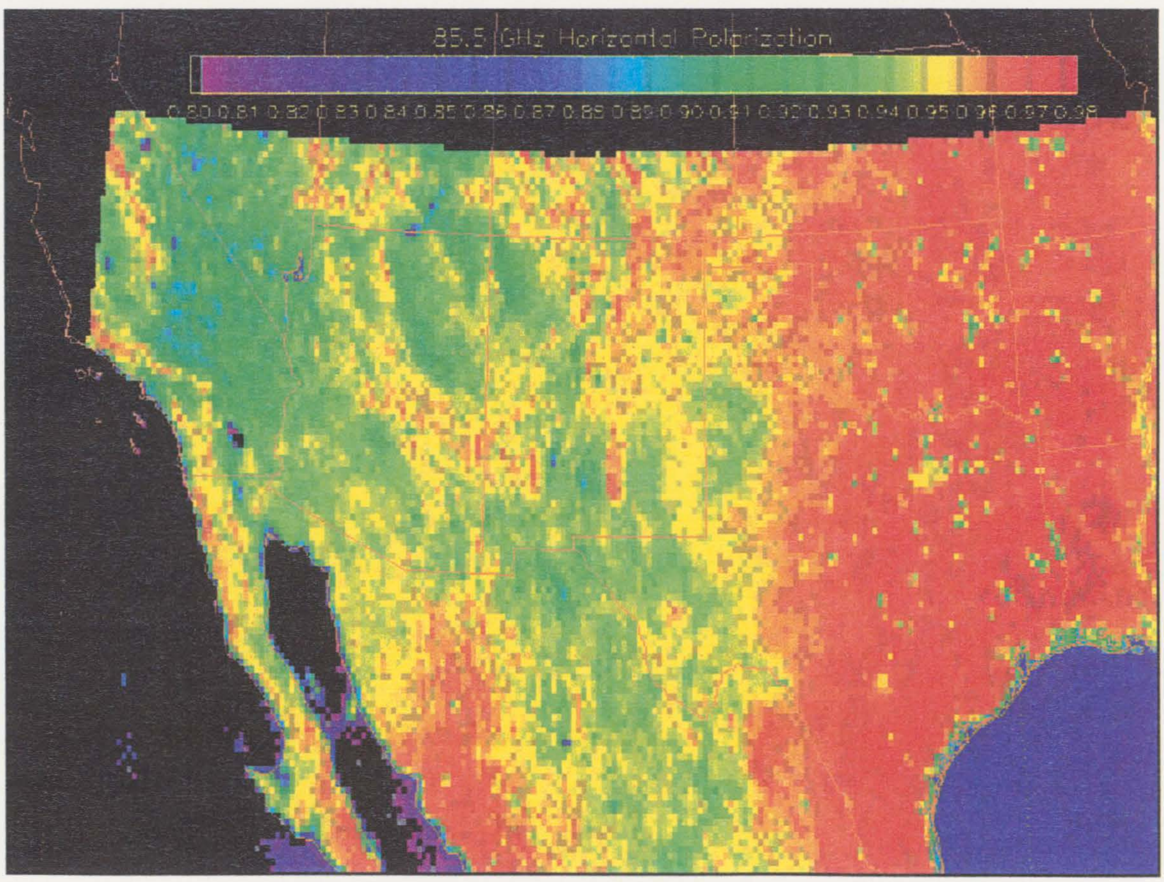

Fig. 4.5: TRMM 85.5 GHz horizontal polarization effective surface emissivity composite from 1 June to 31 August 1998.

As mentioned previously, desert regions also have lower infrared surface emittance, which would cause the surface skin temperature for those regions to be underestimated, thus causing the microwave surface emittance to be underestimated as well (Jones, 1997). The clear sky conditions in Figure 4.6 are based on surface observations which indicate no clouds, however, there may be contaminated data included, e.g., cloudy samples. However, based on 4285 samples, the mean difference (IR brightness temperature minus surface air temperature) was –16 K with a standard deviation of 17.3 K. This clearly shows that the surface skin temperature may be underestimated, on average, with a mean relative error of –6.1% with standard deviation of 7.5%.

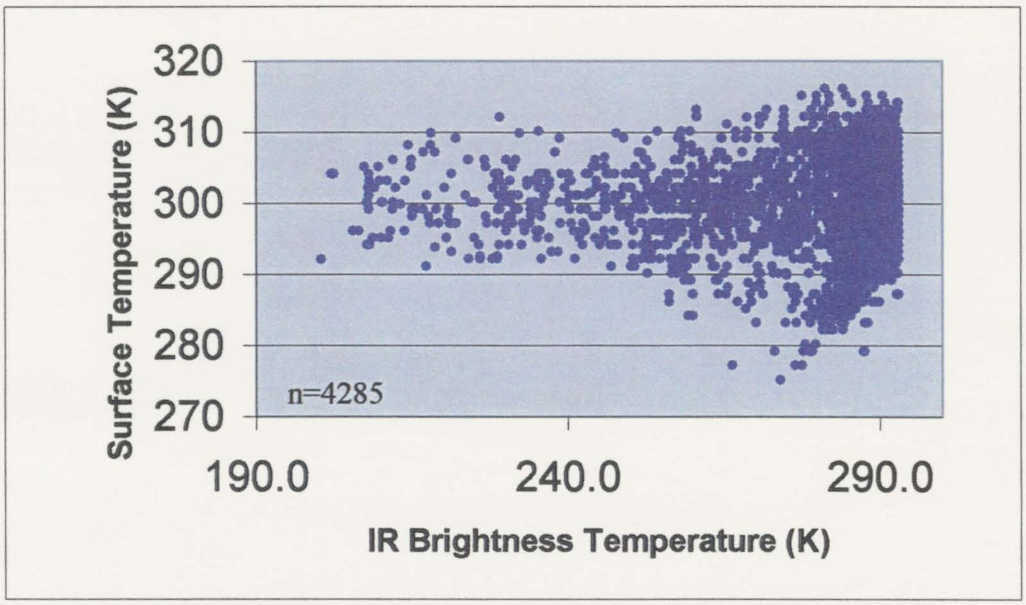

Fig.4.6: Relationship between the clear-sky infrared brightness temperature and the observed surface air temperature over the period June-August 1998.

The desert regions in parts of Arizona and New Mexico, and the Mojave Desert in southern California show rather low microwave surface emittances over a broad region.

Irrigated land and moist croplands have lower microwave surface emittances as well. These regions change only slowly with time and thus appear in the total composite results better than some of the other features that have smaller spatial features or have a significant temporal factor to their existence. Regions of particular significance are Southeastern Colorado, a relatively large region in west Texas near Lubbock, Texas, the San Joaquin Valley in central California, the Imperial Valley in southern California, as well as portions of Northwestern Mexico along situated near the Gulf of California.

Coniferous forests have high microwave surface emittances and are one of the few high surface emittance signatures found (excluding dry arid soil) (see Figure 4.3). Particularly noticeable regions are portions of the Colorado Rockies, the Apache and Gila National Forests of Arizona and New Mexico, the Sacramento Mountains, New Mexico. The conifer vegetation most likely has (1) a higher infrared surface emittance than the surrounding vegetation that biases the surface skin temperature and thus the microwave surface emittances; (2) the water content of the coniferous vegetation is low compared is low compared with other ground vegetation (Jackson and Schmugge, 1991); (3) the coniferous vegetation is particularly rough in appearance to the SSM/I microwave frequencies [Choudhury et al., 1979; Jackson and Schmugge, 1989]; (or 4) a possible combination of these effects.

Particularly noticeable regions are portions of the Colorado Rockies, the Apache and Gila National Forests of Arizona and New Mexico, the Sacramento Mountains, New Mexico, and a large area on the western slopes of the Sierra Madre Mountains of Mexico (this area is covered with mainly needleleaf evergreen trees and patchy broadleaf evergreen shrub form which border the Gulf of California.

4.2.3 Effective Surface Emittance Retrieval Errors

The atmospheric corrected microwave surface emittance values are lower in value than the effective surface emittance values, and the image contrast is enhanced between surface water features and land. This is due to the fact that the sensor sees more of the land effects.

Center Point (ICAO)	Latitude/ Longitude	Elevation (feet)	Mean (90-Day) Vertical ε_{sfc} (effective)	Mean (90-Day) Horizontal ε_{sfc} (effective)
Waco, TX (KACT)	31.62N 97.22W	155	0.9795 $\pm$ 0.0025 (0.26%)	0.9695 $\pm$ 0.0040 (0.42%)
Austin, TX (KAUS)	30.30N 97.70W	189	0.9788 $\pm$ 0.0032 (0.33%)	0.9687 $\pm$ 0.0057 (0.59%)
Dallas, TX (KDAL)	32.85 N 96.85 W	148	0.9720 $\pm$ 0.0041 (0.42%)	0.9538 $\pm$ 0.0077 (0.82%)
Flagstaff, AZ (KFLG)	35.13N 111.67W	2137	0.9664 $\pm$ 0.0048 (0.50%)	0.9562 $\pm$ 0.0065 (0.68%)
Fort Smith, AR (KFSM)	35.33N 94.37W	141	0.9756 $\pm$ 0.0030 (0.31%)	0.9663 $\pm$ 0.0050 (0.53%)
Hobbs, NM (KHOB)	32.68 N 103.22 W	1115	0.9698 $\pm$ 0.0035 (0.36%)	0.9509 $\pm$ 0.0038 (0.40%)
Jackson, MS (KJAN)	32.32N 90.08W	101	0.9773 $\pm$ 0.0030 (0.31%)	0.9682 $\pm$ 0.0065 (0.67%)
Lufkin, TX (KLFK)	31.23N 94.75W	88	0.9822 $\pm$ 0.0022 (0.22%)	0.9758 $\pm$ 0.0034 (0.35%)
Little Rock, AR (KLIT)	34.73 N 92.23 W	79	0.9751 $\pm$ 0.0028 (0.29%)	0.9637 $\pm$ 0.0059 (0.62%)
Riverside, CA (KRIV)	33.88N 117.27W	469	0.9582 $\pm$ 0.0057 (0.60%)	0.9380 $\pm$ 0.0109 (1.16%)
Tucson, AZ (KTUS)	32.12N 110.93W	779	0.9608 $\pm$ 0.0047 (0.49%)	0.9454 $\pm$ 0.0075 (0.80%)

Table 4.2: Selected sites list. Calculated mean 90-day vertically and horizontally polarized effective surface emissivity and absolute uncertainty. Relative uncertainty expressed as a percentage is in parentheses.

Chapter 5

Normalized Polarization Difference (NPD) Method

5.1 Prior Work

The ability to extract cloud LWP from microwave data depends on the degree to which small cloud liquid water (CLW) signal can be separated from the surface emittance background (Diak, 1995), and that ability is essentially the crux of this work. Another principle of primary importance is that electromagnetic radiation emitted and reflected by a polarized surface at microwave wavelengths will depolarize when it interacts with a water cloud. The degree of this depolarization at the top of the atmosphere (TOA) is related to the amount of liquid water in the cloud. This work intends to build upon previous work using the normalized polarization difference method (NPD) in which the microwave brightness temperature difference at 85.5 GHz is divided by the surface emissivity polarization difference to define the NPD.

Using the transmittance form of the radiative microwave transfer equation (Equation 2.1), the difference between the V-polarization and H-polarization intensities can be expressed as

$$\begin{aligned} I_V - I_H &= (\varepsilon_V - \varepsilon_H)B(T_s)\tau \\ &- (\varepsilon_V - \varepsilon_H)\tau^2 \int_{p_s}^{0} \frac{B[T(p)]}{[\tau(p,0)]^2} \frac{\partial \tau(p,0)}{\partial p} dp \\ &- (\varepsilon_V - \varepsilon_H)\tau^2 B(T_{space}), \end{aligned} \tag{5.1}$$

where the frequency dependence has been dropped for clarity. An important consequence of this operation is that one of the atmospheric integral terms cancels. By applying the Rayleigh-Jeans law to the intensities I_V and I_H in equation 2.2 to yield the following for the polarization difference of the brightness temperatures:

$$\Delta T_B \approx \frac{c^2}{2K\upsilon^2} \Delta\varepsilon\tau \left\{ B(T_S) - \tau \int_{P_S}^{0} \frac{B[T(p)]}{[\tau(p,0)]^2} \frac{\partial \tau(p,0)}{\partial p} dp - \tau B(T_{cos}) \right\}, \tag{5.2}$$

where $\Delta\varepsilon = \varepsilon_V - \varepsilon_H$, c is the speed of light and K is the Boltzmann's constant.

$$\Delta T_B \approx \Delta\varepsilon(T_S - T_a)\tau \tag{5.3}$$

where ΔT_B is the brightness temperature polarization difference (v-h) at the TOA, $\Delta\varepsilon$ is the surface emissivity polarization difference (v-h), T_S is the surface skin temperature, T_a is the reflected atmospheric emission term, and τ is the total atmospheric transmittance. Also, the deep space term is included in Equation 2.3, but is neglected here since it is small. Since ΔT_B is directly proportional to $\Delta\varepsilon$, this allows the major surface property (i.e., emissivity) to be factored out to define a normalized polarization difference (NPD), $\Delta T_B/\Delta\varepsilon$. This type of normalization is not possible using only the individual brightness temperature polarization components (Combs et al., 1998).

The NPD method was developed to find cloud liquid water path over land, and will be applied to the highly related area of cloud detection and height estimation based on the degree of depolarization of the polarized signal.

5.1.1 Model Simulations

Greenwald (1997) extended and improved upon work done by Jones and Vonder Haar (1990) in retrieving cloud LWP for nonprecipitating clouds over land surfaces using SSM/I. Another aim was to investigate the retrieval problem and its limitations more thoroughly. As in the method of Jones and Vonder Haar, Greenwald used 85.5 GHz measurements of surface emissivity composites created from near-coincident and co-located SSM/I measurements and window IR measurements under clear sky conditions, but he used a modified method that takes advantage of the polarization difference of the brightness temperatures at 85.5 GHz.

First, Greenwald simulated 85.5 GHz measurements over land under clear sky conditions. He believed this would provide an indication of the integrity of the surface emissivity composites; give further confidence in attacking the inverse problem; and can yield a quantitative measure of the anticipated background noise level above which retrievals can be performed. Greenwald found that the horizontal component was more sensitive to surface moisture than the vertical component (as expected), and speculated that this might be caused by recent rainfall events or local irrigation. Despite the slightly greater noise at this polarization, this problem can be usually overcome in the CLW retrievals since the brightness temperature at horizontal polarization is more sensitive to CLW than at vertical polarization due to its lower surface emissivity.

Accurate knowledge of the skin temperature is a crucial element in correctly simulating clear-sky SSM/I brightness temperature over land. This may have direct implications for CLW retrievals since an incorrect skin temperature might lead to large biases in the retrievals. However, under cloudy conditions one might expect the surface air temperature and the skin temperature to usually be similar. In order to detect CLW at 85.5 GHz over land surfaces one must be above the clear-sky noise level of approximately 2.5 K. The potential sources of uncertainty in the skin temperature estimations include uncertainties in the transmittance model and humidity-temperature profiles.

One way to illustrate the detection of CLW at 85.5 GHz is to subtract the emission at the surface (i.e., the emission in the absence of an atmosphere) from the instantaneous SSM/I observations. This difference can be thought of as a measure of the absorption resulting from gaseous absorption (primarily H^2O) and CLW droplets (absorption by cloud ice particles is negligible at microwave frequencies). For precipitating clouds, however, this difference is more difficult to interpret since scattering processes also contribute to the brightness temperatures measured at the TOA.

The varied responses of these frequencies under different atmospheric and cloud conditions have several important ramifications for retrieving cloud liquid water over land surfaces. First, for clouds with high amounts of LWP (greater than 0.5 kg m^2 or so) it is clear that the polarization difference will be less useful at 85.5 GHz since the sensitivity of T_b to cloud LWP is greatly reduced. However, this is true for the value of specified in the calculations; more polarized land surfaces might make the 85.5-GHz frequency more useful at larger cloud LWP. At 37 GHz the sensitivity is higher for larger cloud LWP and suggests this frequency could be used for retrievals in nonprecipitating clouds with high LWP. The results also show that in atmospheres with an abundance of water vapor, such as in the Tropics, the ability to measure cloud LWP at 85.5 GHz is significantly reduced, but retrievals at 37 GHz might be possible since the magnitude of T_b remains large. There are many important advantages to the polarization difference approach. For example, the SC method, as discussed previously, suffers from an inability to detect low clouds, no matter how much liquid water is contained in the cloud. But from Fig. 5.1 we can see that low clouds become detectable from a polarization difference perspective. Based on model simulations, Greenwald (1997) calculated the polarization difference at 85.5 GHz for a 1-km-thick low cloud using the midlatitude summer (MS), midlatitude winter (MW), and tropical standard (TR) atmospheres using humidity and temperature profiles from McClatchey et al. (1972). Results indicate that the response at 85.5 GHz to cloud liquid water is very small.

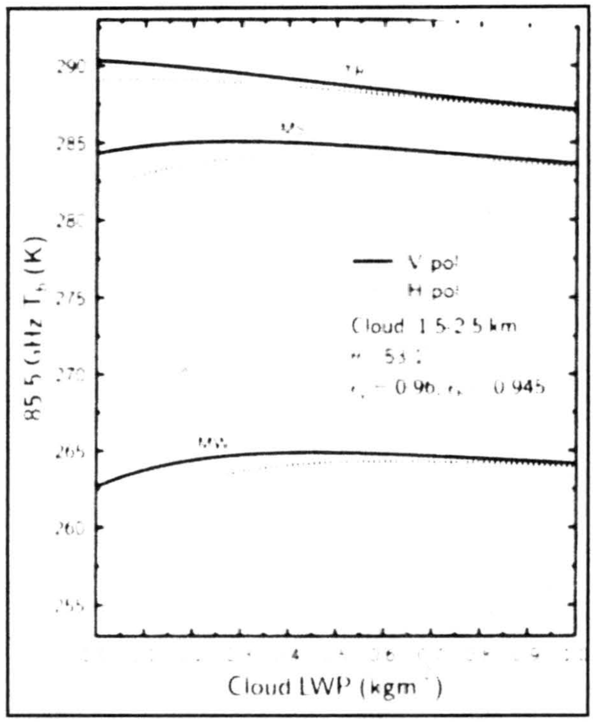

Figure 5.1: Theoretical calculations of 85.5-GHz brightness temperatures (K) at vertical and horizontal polarization versus cloud liquid water path for a low-lying cloud (1.5-2.5 km) over a land surface. The calculations were done at a zenith angle θ of 53.1° and for three different sets of temperature-humidity profiles taken from McClatchey et al. (1972): tropical (TR), where the integrated water vapor is 42 kg m^{-2}; midlatitude summer (MS), where PWC = 20 kg m^{-2}; and midlatitude winter (MW), where PWC = 8.8 kg m^{-2}.

At 85.5 GHz, the polarization difference decreases as a function of cloud LWP due to the greater water vapor and liquid water absorption and depolarization. There is also a definite brightness temperature polarization difference for the midlatitude summer atmosphere, which ranges from about 2.5K to 0.25K for cloud LWP of 1.0 kgm^{-2}.

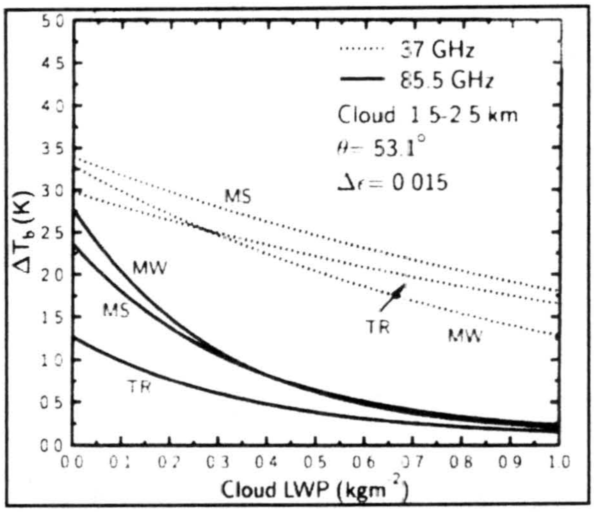

Figure 5.2: Theoretical calculations of the polarization difference (ΔTB) at 85.5 and 37 GHz as a function of cloud LWP for a 1-km-thick low cloud for three standard atmospheres (Greenwald, 1997).

In summary, Greenwald states that low clouds are easier to detect with this method than by using a single channel method. Greenwald further noted that errors in the cloud LWP retrievals originate from uncertainties in the Millimeter-wave Propagation Model (MPM), and the vertical distribution of liquid water and the cloud base and cloud-top heights. Diak (1995) found that multilevel clouds can introduce further errors in microwave retrievals.

Combs (1998) also calculated the theoretical results of ΔT_B / $\Delta\varepsilon$ versus cloud liquid water for different atmospheres at a zenith angle of 53.1°. Using Liebe's 1992 version of the Millimeter-wave Propagation Model to compute the atmospheric attenuation, she found that the 85.5 GHz NPD is sensitive to LWP in winter atmospheres, and diminishes for tropical atmospheres (Fig. 5.3). One advantage of the NPD method is that since $\Delta\varepsilon$ is small for land surfaces (0.015-0.020), ΔT_B is less sensitive to changes in the surface skin temperature. In addition, when applying this method to actual measurements, the relative accuracy of the measurements is more important than the absolute accuracy. One disadvantage of the NPD approach when compared to single channel methods is that since it is a difference method second order errors, such as instrument noise, become a greater contributor to the random errors (Combs, 1998).

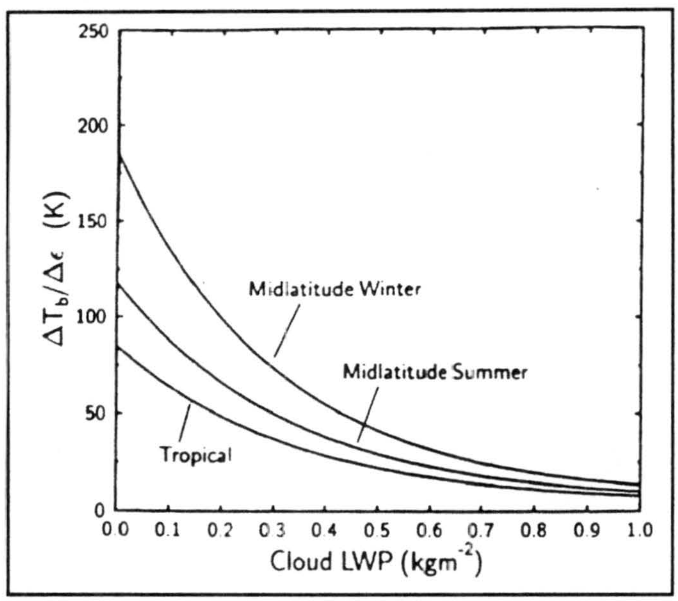

Figure 5.3: Theoretical results of ΔT_B / $\Delta\varepsilon$ versus cloud liquid water path at 85.5 GHz for different atmospheres at a zenith angle of 53.1^0 (Combs et al., 1998).

5.1.2 Case Studies

The work of Jones and Vonder Haar (1990), Greenwald (1997), and Combs (1998) showed that the use of passive microwave over land is indeed feasible. In fact, their success was due to the larger cloud attenuation and their ability to minimize the effects of surface emissivity variations.

Other potential difficulties that can generally plague microwave retrievals involve complex variations in surface emissivity and broken cloudiness. Increases in surface moisture from irrigation and, particularly, rainfall events in certain regions can often reduce the surface emissivity to such an extent that it is significantly smaller than the 7-day composite emissivity. In these cases the retrieval will likely greatly overestimate the cloud LWP. Therefore, care must be taken in identifying these situations. The problem of retrieving cloud liquid water under broken cloudiness is important since microwave measurements from space are typically of coarse spatial resolution. The study of JV90 addressed this issue and found that the retrieval errors were greatest for the smallest cloud LWP and sparse cloudiness. However, these effects may be at least partially accounted for by using IR and/or visible data to help in quantifying the degree of cloudiness within the FOV of the TRMM.

One of the most important advantages this method has over a single-channel (SC) method is that T_b is extremely insensitive to changes in the surface skin temperature; hence, precise knowledge of the skin temperature is less crucial in the retrievals. This can be demonstrated by taking the partial derivative of (3) with respect to T_s, which gives

$$\frac{\partial \Delta \mathrm{T_b}}{\partial \mathrm{T_s}} \approx \Delta\varepsilon\tau\left(\frac{\mathrm{h}\upsilon}{\mathrm{KT_s}}\right)^2 \frac{e^{\mathrm{h}\upsilon/\mathrm{KT_s}}}{(e^{\mathrm{h}\upsilon/\mathrm{KT_s}}-1)^2},$$

where h is Planck's constant and $\partial\Delta\varepsilon/\partial T_s$ is ignored since it is negligible. At 85.5 GHz, and using $T_s = 294$ K, $\Delta\varepsilon = 0.02$, and a typical cloudy atmospheric transmittance of 0.58, it follows that $\partial_{85}/\partial T_s \approx 0.011$. This means that a 1-K perturbation in T_s results in a very small change of 0.011 K in T_{85}. The high insensitivity of T_b to changes in T_s results primarily from the small values of $\Delta\varepsilon$ that occur over land and the extremely low sensitivity of $\Delta\varepsilon$ to changes in T_s (Greenwald, 1997).

Yet another advantage is that the polarization difference becomes dependent on the relative accuracy of the measurements rather than their absolute accuracy. Therefore, even though the magnitude of the polarization difference at 85.5 GHz in cloudy regions can often be less than 2 K, which is about the estimated absolute accuracy of the individual SSM/I measurements (Hollinger et al. 1990), the polarization difference is affected by *interchannel* relative accuracies that are, based on preflight calibration, within 0.2 K over a broad range of temperatures (Hollinger et al. 1987).

The major disadvantage of this approach is that in principle it can only be applied when the surface is polarized (i.e., 85.5 GHz vertical – 85.5 GHz horizontal > 0). However, this is not as severe a limitation as it first appears since the results from Jones (1996) indicate that a small surface polarization signal is measurable and very common over many land regions, with the notable exception of forested regions. With a sufficiently polarized land surface, quantitative LWP retrievals can be performed (Greenwald et al., 1997) i.e. $\Delta\varepsilon > 0.015$.

There are several advantages to the NPD approach (Greenwald et al., 1997). One is that low clouds are easier to detect with this method than by using a single channel method (Jones and Vonder Haar, 1990). This is due to the NPD method being less sensitive to the cloud height. Another is that since $\Delta\varepsilon$ is small for land surfaces (0.015-0.020), ΔT_b is less sensitive to changes in the surface skin temperature. In addition, when applying this method to actual measurements, the relative accuracy of the measurements is more important than the absolute accuracy. However, one disadvantage of the NPD approach when compared to single channel methods is that since it is a difference method second order errors, such as instrument noise, become a greater contributor to the random errors (Combs et al., 1998).

5.2 Results

A new method based on a normalized polarization difference has been developed to retrieve cloud LWP for nonprecipitating clouds over land surfaces using the 85.5-GHz channels of the TMI and IR measurements. A polarization difference approach can be applied over land surfaces since many land surfaces exhibit a small polarization signal. The method has the distinct advantages of being very insensitive to the surface skin temperature and is dependent only on the relative accuracy of the brightness temperatures rather than their absolute accuracy. Also, this method has the ability to estimate cloud LWP for low-lying clouds, which is more difficult for the single-channel methods, as shown from theory and observational evidence. The NPD method is shown to be less useful in atmospheres with an abundance of water vapor and for large values of cloud LWP. However, based on theoretical simulations, the polarization difference at 37 GHz may also prove useful for retrieving cloud LWP under these conditions.

The area that this work initially concentrated on was the southwestern United States, an area bounded from 90° to 120° W and from 20° to 40° N, from June through August of 1998. This area was chosen because the NPD method requires a surface emissivity polarization difference, in order to identify over-lying clouds (cloud signal). This accounts for the majority of the surface variation. The southwest US generally has sparse vegetation, high surface emittance values, and suitable polarization differences (0.010-0.020). Within this large sector, areas with significant polarization differences were found by calculating the mean polarization difference (85.5 GHz vertical minus horizontal surface emissivity), and the standard deviation of the mean polarization difference. Areas where the mean difference was greater than the standard deviation were plotted, with extremely large polarization differences filtered out (i.e., greater than 0.05) since these highly polarized regions were predominantly found over the warm water Gulf of Mexico and the Eastern Pacific. To test, specifically, which areas would be best suited for the NPD method, the mean and standard deviation polarization difference (background variability) at 85.5 GHz was calculated for each grid point. The mean polarization differences are large over water bodies and desert regions as expected in Figure 5.4. In the desert regions, values of $\Delta\varepsilon$ range from 0.03 to 0.05, while the large lakes can have $\Delta\varepsilon$ values greater than 0.2. These areas must be NPD-valid (mean polarization differences > 0.015), but must also have strong signals above the background noise.

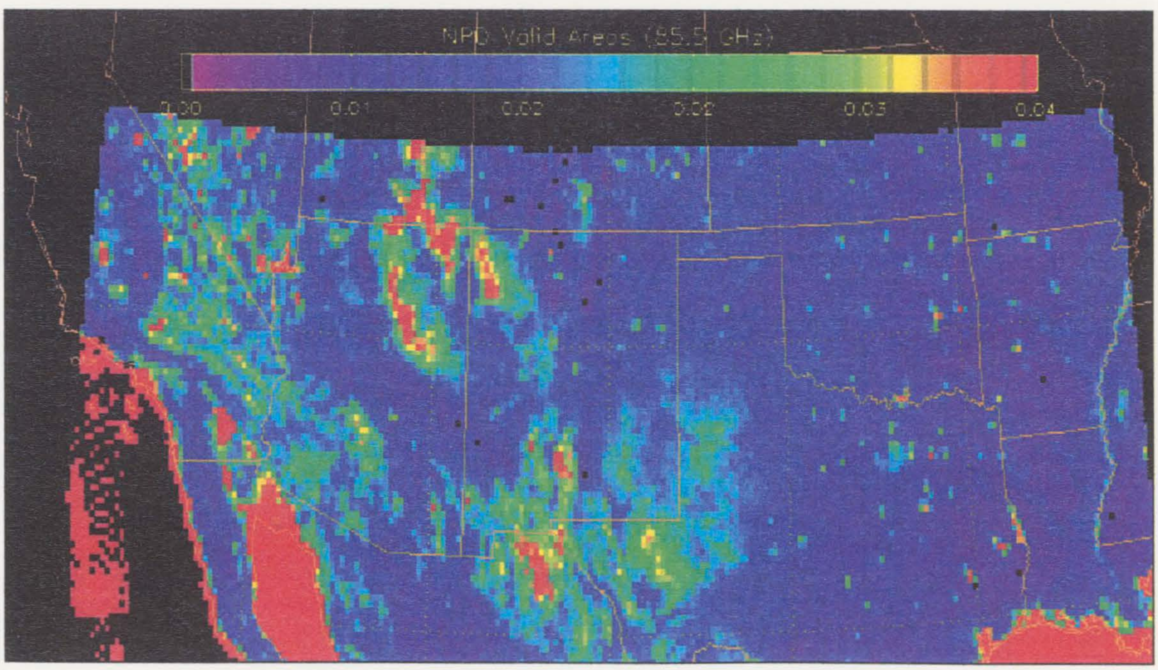

Figure 5.4: Mean 90-day 85.5 GHz surface emissivity polarization difference minus 90-day standard deviation of the 85.5 GHz surface emissivity polarization difference.

Figure 5.4 shows areas where the NPD method would be more likely to work, as well as poorly-polarized areas where the method probably won't work. Areas where the mean polarization difference for 85.5 GHz exceeded one standard deviation are plotted. When the mean polarization difference is less than one standard deviation, this signifies that the polarization difference is indistinguishable from the natural variability. When they exceed one standard deviation, the polarization difference can be distinguished from the background variability. The greater the positive difference, the greater the chance for the NPD method to succeed.

Once these NPD valid areas were identified, I selected a number of test areas, which also had sufficient observational coverage as well as high polarization differences. These sites are listed in the table below and show the mean polarization difference as well as the standard deviation of the polarization difference for the 90-day surface emissivity composite period.

Center Point (ICAO)	**Latitude/ Longitude**	**Elevation (feet)**	**Mean (90-Day) Polarization Difference (PD)**	**Standard Deviation (90-Day) of PD**	**Mean – Standard Deviation**
Waco, TX (KACT)	31.62N 97.22W	155	0.01864	0.00874	0.0099
Austin, TX (KAUS)	30.30N 97.70W	189	0.01591	0.00466	0.01125
Dallas, TX (KDAL)	32.85N 96.85 W	148	0.01958	0.00531	0.01427
Flagstaff, AZ (KFLG)	35.13N 111.67W	2137	0.00886	0.00486	0.004
Fort Smith, AR (KFSM)	35.33N 94.37W	141	0.01342	0.00528	0.00814
Hobbs, NM (KHOB)	32.68N 103.22 W	1115	0.01973	0.0056	0.01413
Jackson, MS (KJAN)	32.32N 90.08W	101	0.00917	0.00507	0.00411
Lufkin, TX (KLFK)	31.23N 94.75W	88	0.00662	0.00442	0.0022
Little Rock, AR (KLIT)	34.73N 92.23 W	79	0.0157	0.00566	0.01004
Riverside, CA (KRIV)	33.88N 117.27W	469	0.02141	0.00682	0.01459
Tucson, AZ	32.12N 110.93W	779	0.02501	0.00869	0.01632

(KTUS)					

Table 5.1: Selected sites list. Calculated mean 90-day effective surface emissivity polarization difference (PD) and standard deviation (background noise). Also, shown is the signal above the noise (i.e., PD minus standard deviation).

Table 5.1 shows the 11 primary sites that were examined in the Southwest US. As mentioned earlier, the NPD method should work when polarization differences are greater than 0.015. These sites are comprised of Dallas, Hobbs, Riverside, Tucson, Waco, Little Rock, and Austin. Additionally, an arbitrary threshold was set for those sites having a large polarization difference minus 1 standard deviation (background noise) value. These sites are thought to have a greater chance of seeing clouds (< 10,000 foot base) and are more likely for the NPD method to work successfully. These sites are Dallas, Hobbs, Riverside, and Tucson. Sites that have small polarization differences, and which are not likely to yield successful results are Flagstaff, Fort Smith, Jackson, and Lufkin.

Based on previous work, a new application of the NPD method to identify low cloud base height below ten thousand feet will be presented. The normalized polarization difference (vertical minus horizontal polarization) at 85.5 GHz is used in conjunction with the 11.0 μm brightness temperature to examine the possibility of identifying low cloud base height, or rather of separating the low cloud signal from that of the signal from cirrus, clear skies, precipitation areas, and background noise.

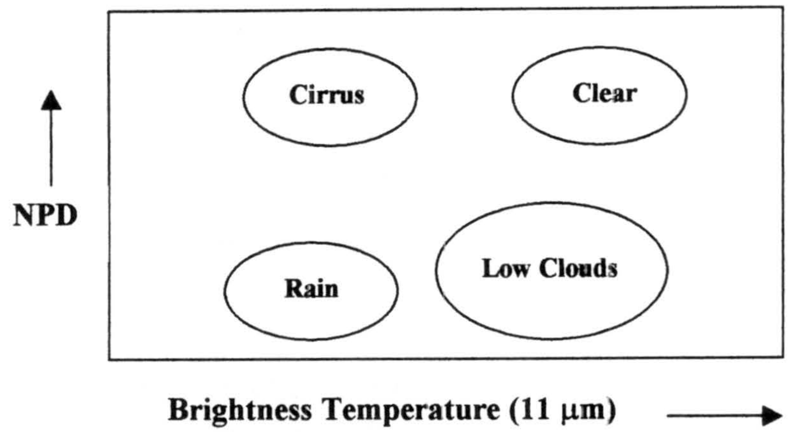

Figure 5.5: Cartoon depicting theoretical relationship between the IR Brightness temperature and the NPD value.

Figure 5.5 represents a simplified schematic showing the basic problem involved in separating the low-cloud signal from that of cirrus, precipitation, and clear skies using the normalized polarization difference and 11 μm infrared data. Low cloud areas should have relatively cool brightness temperatures since at infrared wavelengths the low clouds act to trap upwelling radiation, emitting at colder cloud-top temperatures. They should also have low values of NPD since they act to depolarize upwelling microwave radiation, preferentially in the horizontal. The thicker the cloud the more depolarized the radiation will become, and the NPD is expected to approach zero when the cloud completely depolarizes the radiation. Cirrus should have relatively high NPD values since the majority of upwelling microwave radiation will penetrate to the sensor, and warm to cool IR brightness temperatures since this is at a window channel and there should be very little attenuation of signal by atmospheric constituents, but depending on the thickness of the cirrus, the cirrus may trap some IR radiation and emit partially at colder cloud-top temperatures. Clear skies should have very warm IR brightness temperatures in the summer over the southwest US, and microwave brightness temperatures will be high since the relative humidity is very low in general, and the attenuation of microwave radiation will also be very low--this will produce high NPD values. Areas of precipitation will have low NPD and low IR brightness temperatures, since microwave upwelling radiation will be scattered by precipitation-sized particles (scattering processes dominate at the microwave wavelengths and the particle sizes involved--Mie region.

Results from the comparisons between NPD and IR brightness temperature at 11 μm will then be examined by comparing them quantitatively to observed cloud base height at several primary observation sites, as well as, contrasted against poorly polarized sites (Oklahoma City, OK and Little Rock, AK).

The primary objective is to filter the data and only keep the non-precipitating cloud cases. To meet this objective, a modified Grody algorithm was used to eliminate suspected precipitating clouds. Remember that the TRMM satellite has a frequency change of the water vapor channel from 22.235 to 21.3 GHz. This change off the center of the water vapor line was made in order to avoid saturation in the tropical orbit of TRMM, but could possibly affect the accuracy of the Grody algorithm. Observational data was also used to eliminate possible wet ground cases and multiple cloud layers.

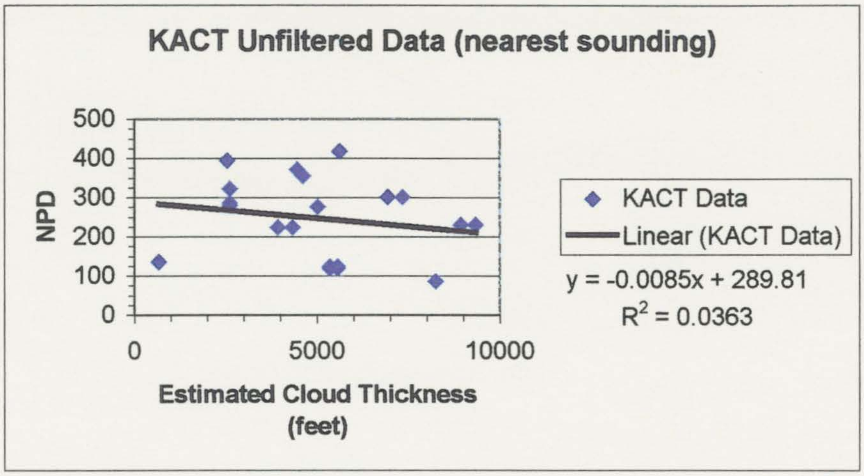

Figure 5.6: Waco, TX (KACT) NPD value versus estimated cloud thickness. Unfiltered data with linear best fit.

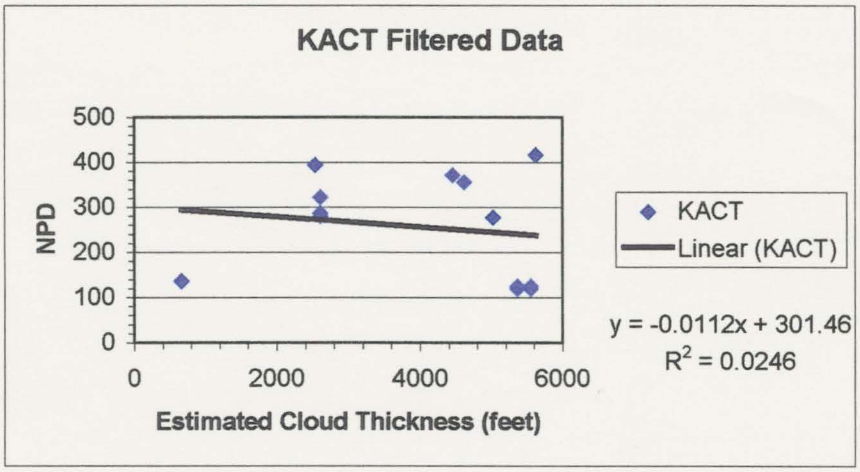

Figure 5.7: Waco, TX (KACT) NPD value versus estimated cloud thickness. Filtered data with linear best fit.

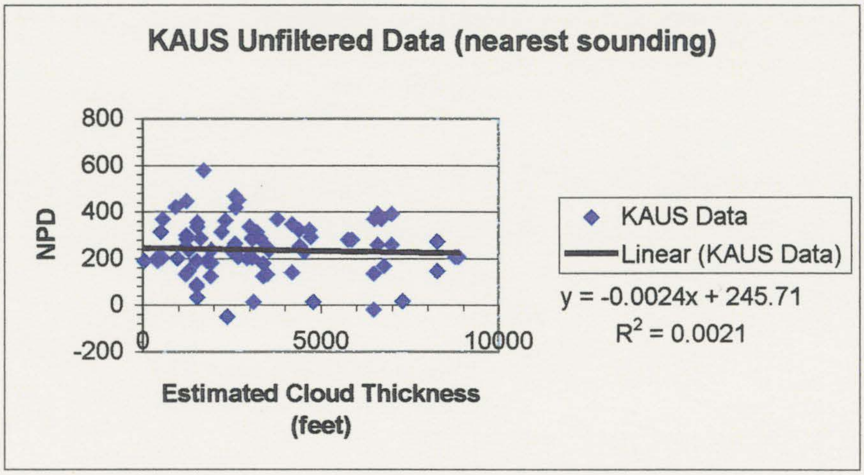

Figure 5.8: Austin, TX (KAUS) NPD value versus estimated cloud thickness. Unfiltered data with linear best fit.

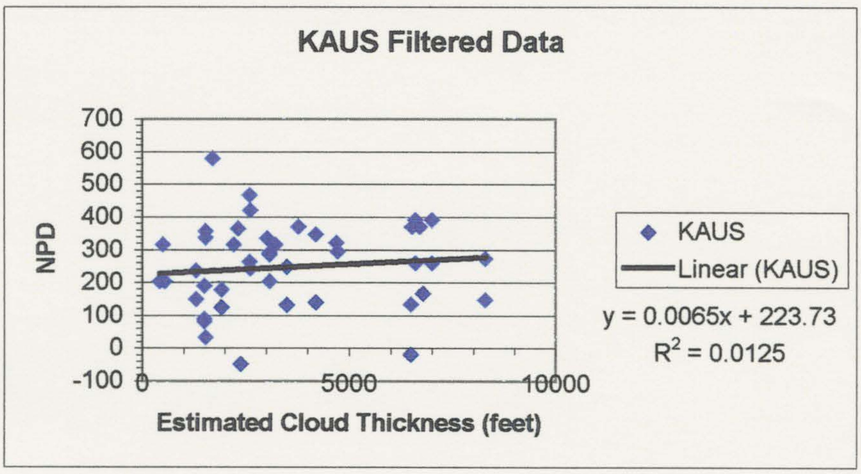

Figure 5.9: Austin, TX (KAUS) NPD value versus estimated cloud thickness. Filtered data with linear best fit.

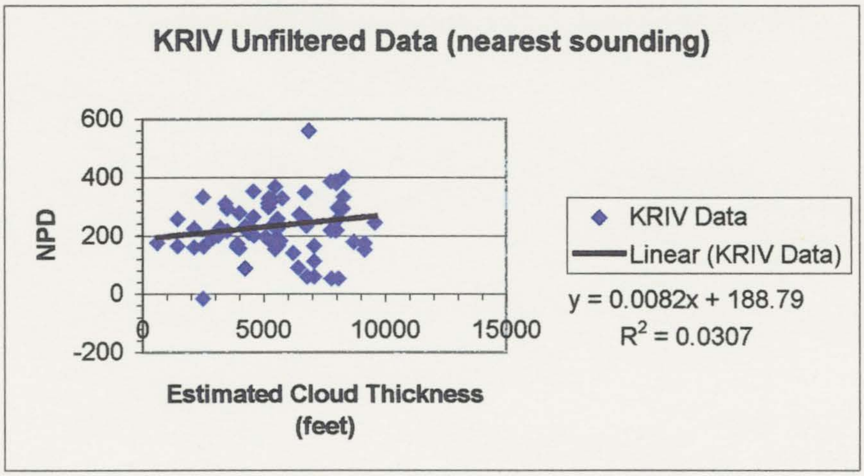

Figure 5.10: Riverside, CA (KRIV) NPD value versus estimated cloud thickness. Unfiltered data with linear best fit.

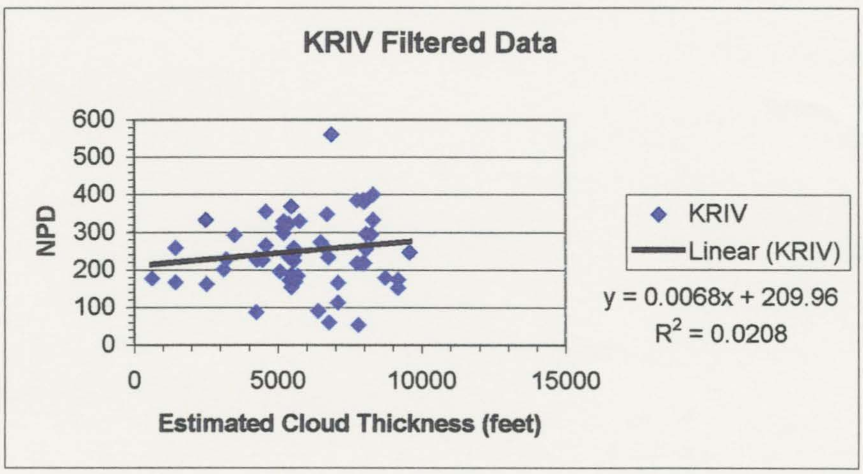

Figure 5.11: Riverside, CA (KRIV) NPD value versus estimated cloud thickness. Filtered data with linear best fit.

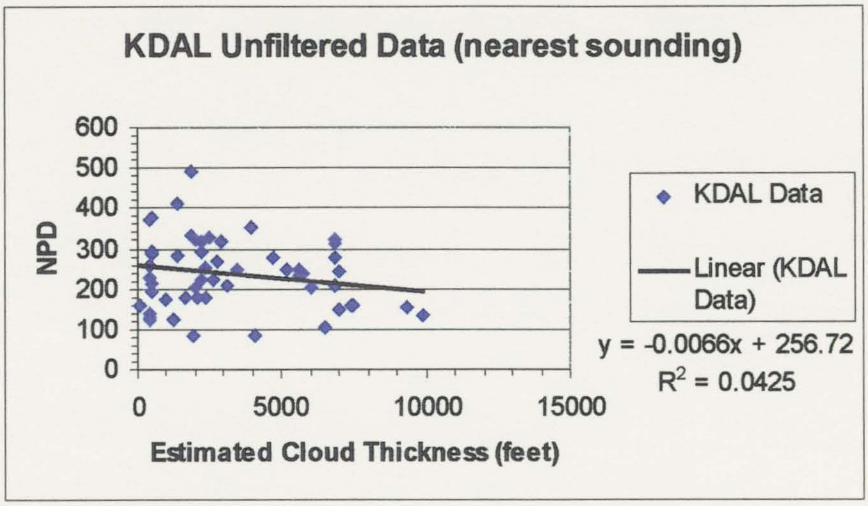

Figure 5.12: Dallas, TX (KDAL) NPD value versus estimated cloud thickness. Unfiltered data with linear best fit.

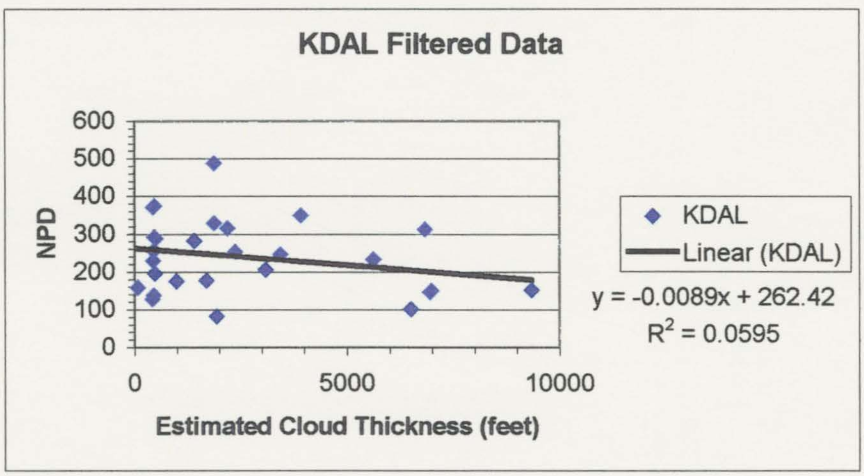

Figure 5.13: Dallas, TX (KDAL) NPD value versus estimated cloud thickness. Filtered data with linear best fit.

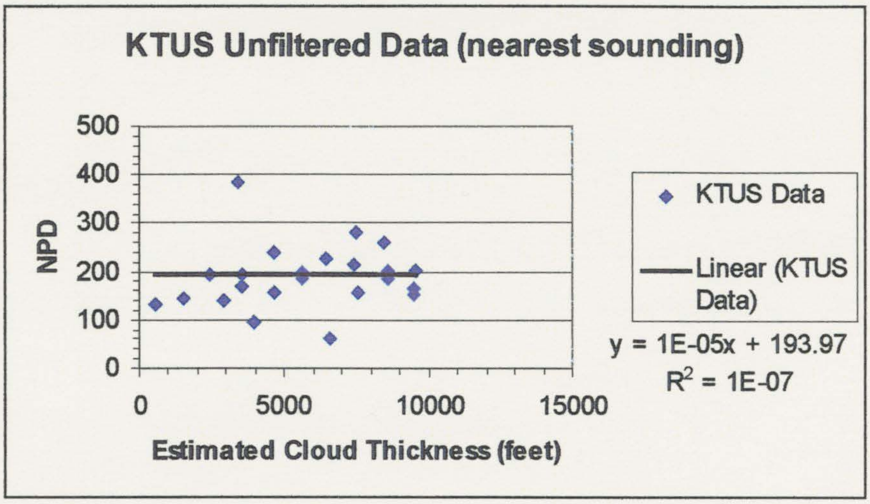

Figure 5.14: Tucson, AZ (KTUS) NPD value versus estimated cloud thickness. Unfiltered data with linear best fit.

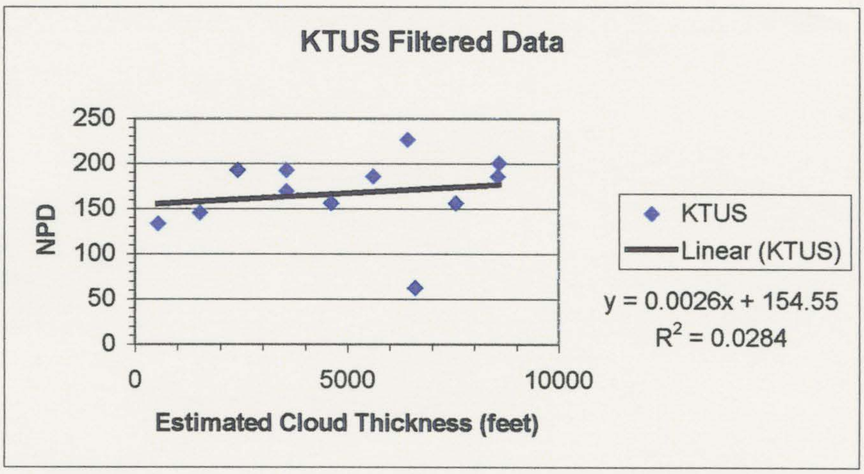

Figure 5.15: Tucson, AZ (KTUS) NPD value versus estimated cloud thickness. Unfiltered data with linear best fit.

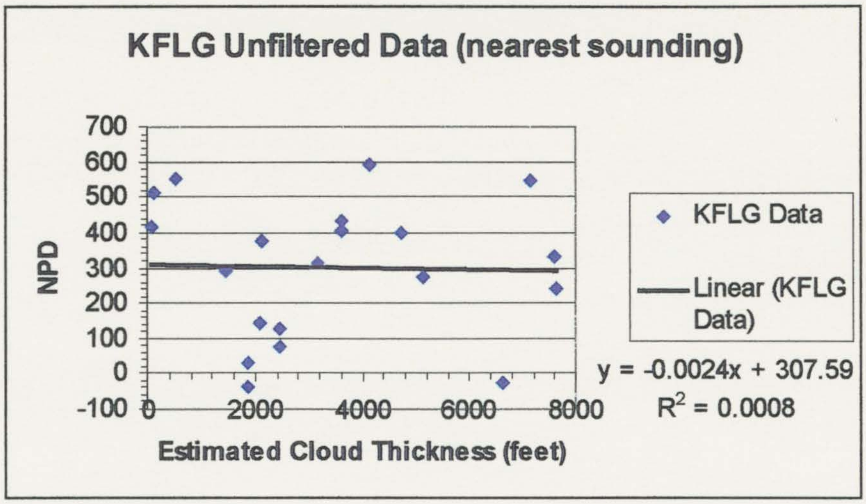

Figure 5.16: Flagstaff, AZ (KFLG) NPD value versus estimated cloud thickness. Unfiltered data with linear best fit.

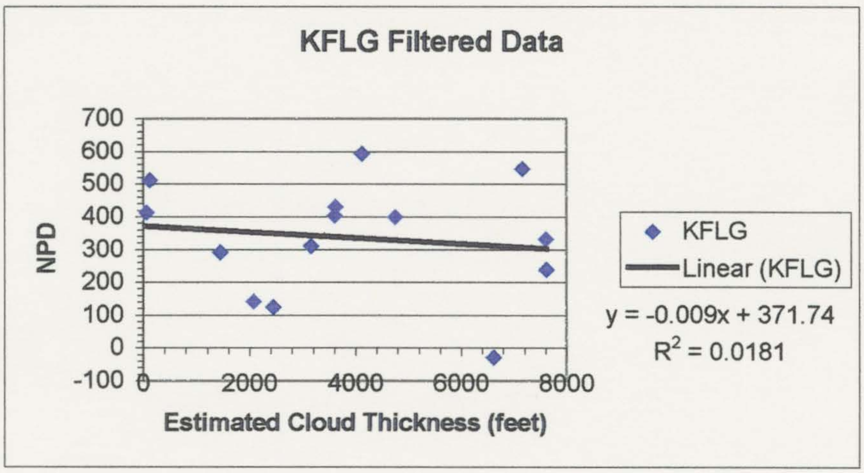

Figure 5.17: Flagstaff, AZ (KFLG) NPD value versus estimated cloud thickness. Filtered data with linear best fit.

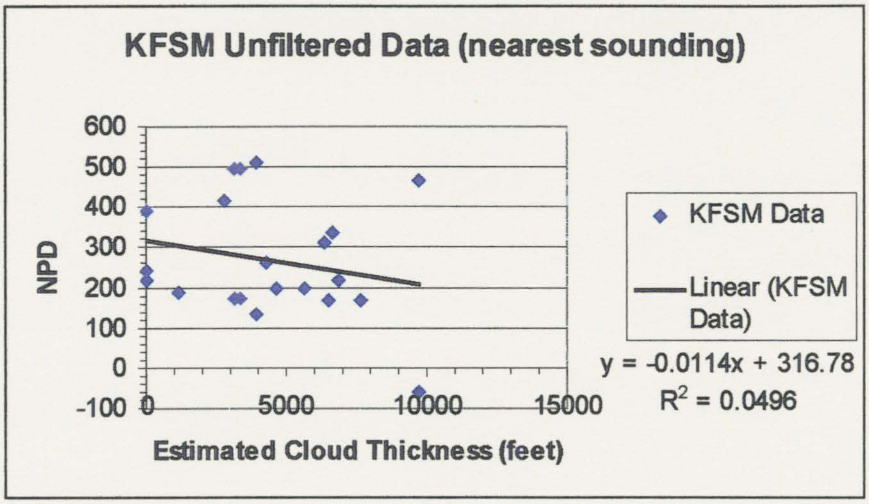

Figure 5.18: Fort Smith, AK (FSM) NPD value versus estimated cloud thickness. Unfiltered data with linear best fit.

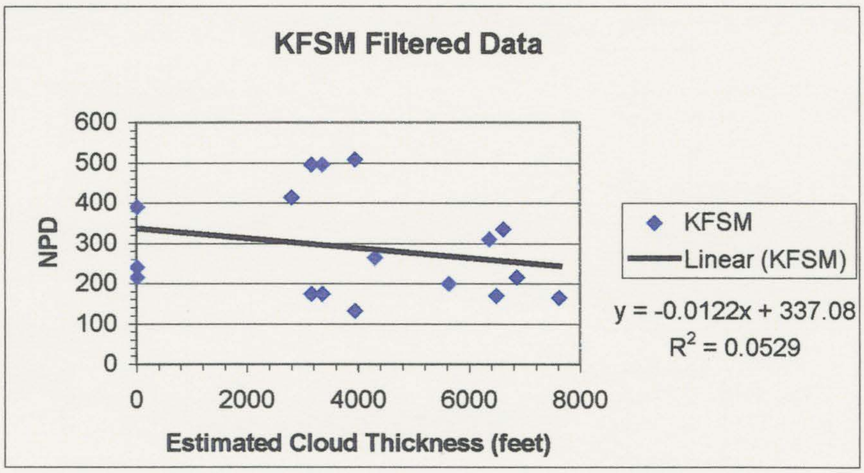

Figure 5.19: Fort Smith, AK (FSM) NPD value versus estimated cloud thickness. Filtered data with linear best fit.

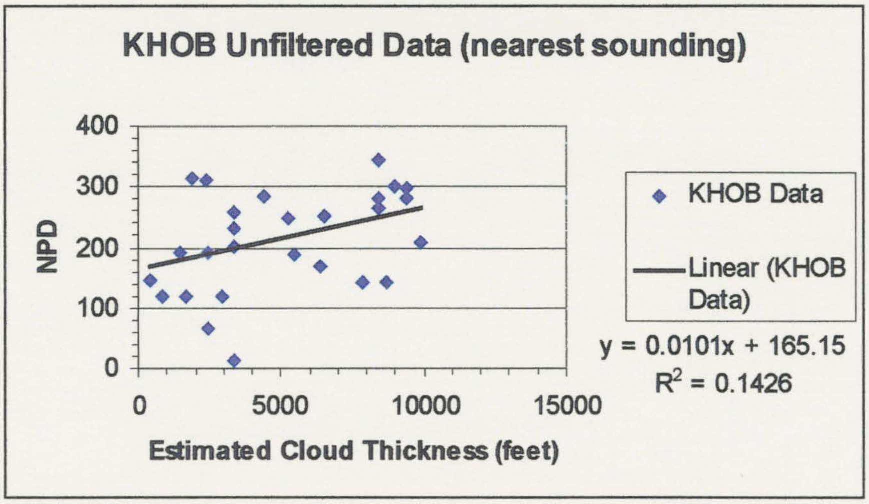

Figure 5.20: Hobbs, NM (KHOB) NPD value versus estimated cloud thickness. Unfiltered data with linear best fit.

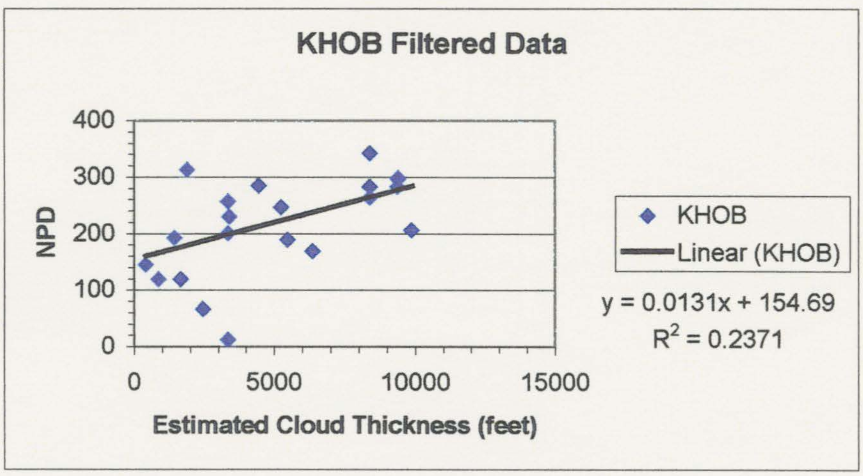

Figure 5.21: Hobbs, NM (KHOB) NPD value versus estimated cloud thickness. Filtered data with linear best fit.

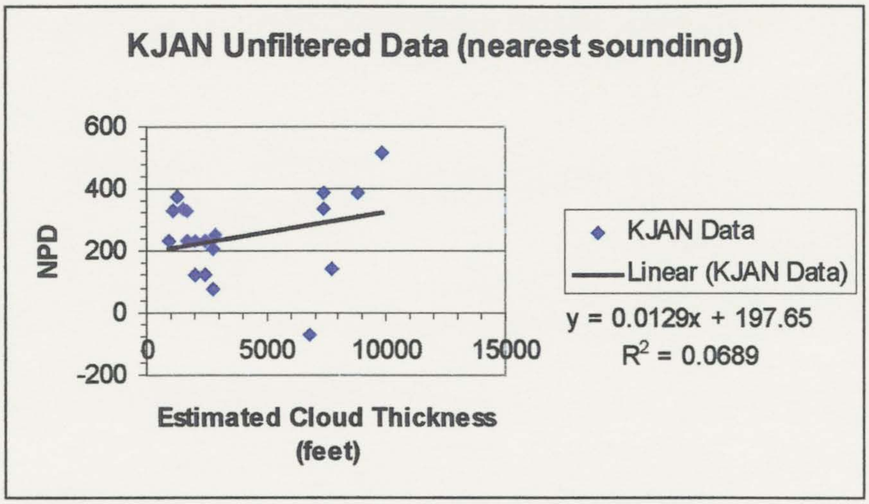

Figure 5.22: Jackson, MS (KJAN) NPD value versus estimated cloud thickness. Unfiltered data with linear best fit.

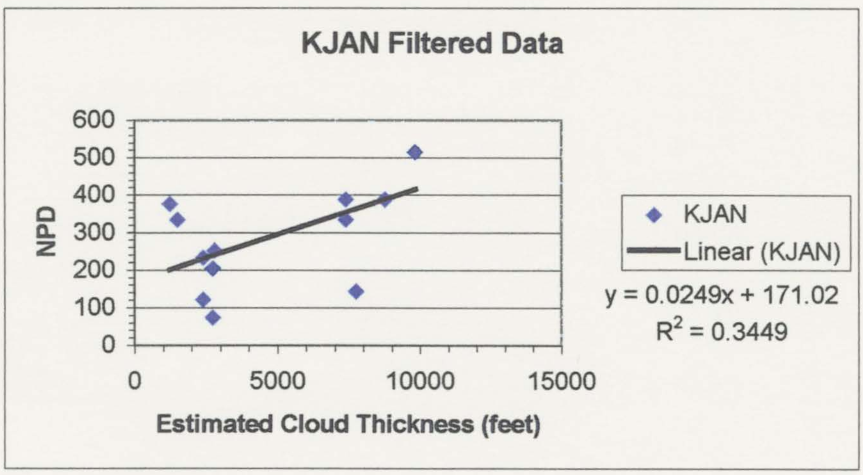

Figure 5.23: Jackson, MS (KJAN) NPD value versus estimated cloud thickness. Filtered data with linear best fit.

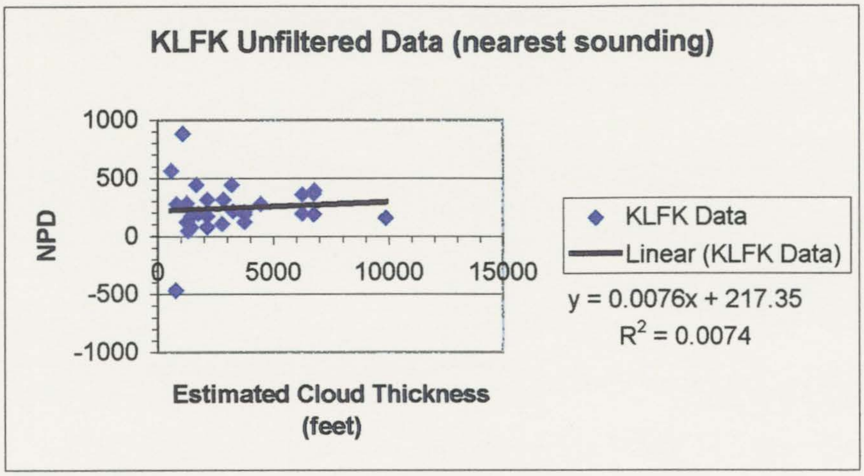

Figure 5.24: Lufkin, TX (KLFK) NPD value versus estimated cloud thickness. Unfiltered data with linear best fit.

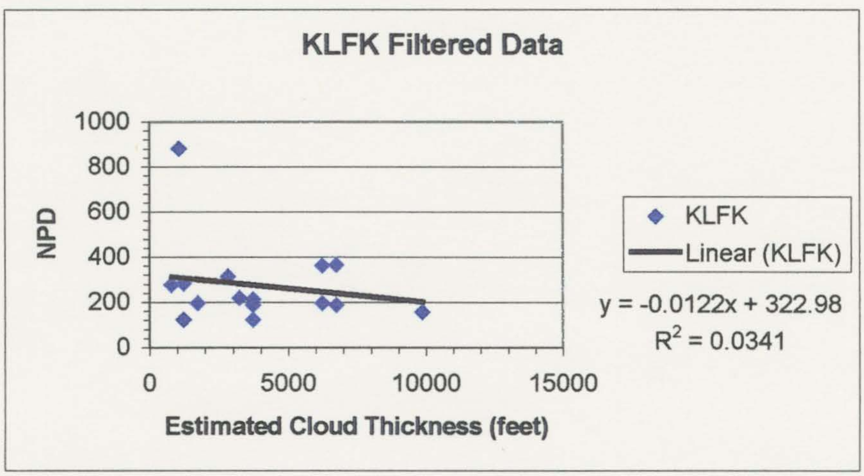

Figure 5.25: Lufkin, TX (KLFK) NPD value versus estimated cloud thickness. Filtered data with linear best fit.

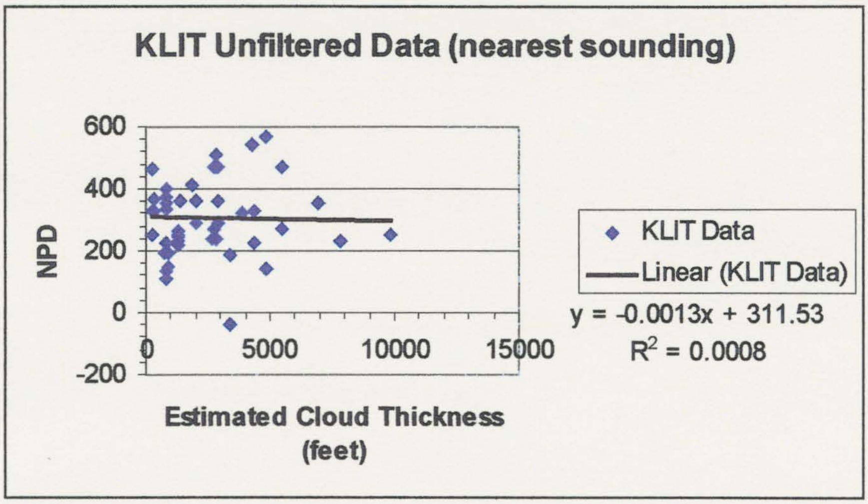

Figure 5.26: Littlerock, AK (KLIT) NPD value versus estimated cloud thickness. Unfiltered data with linear best fit.

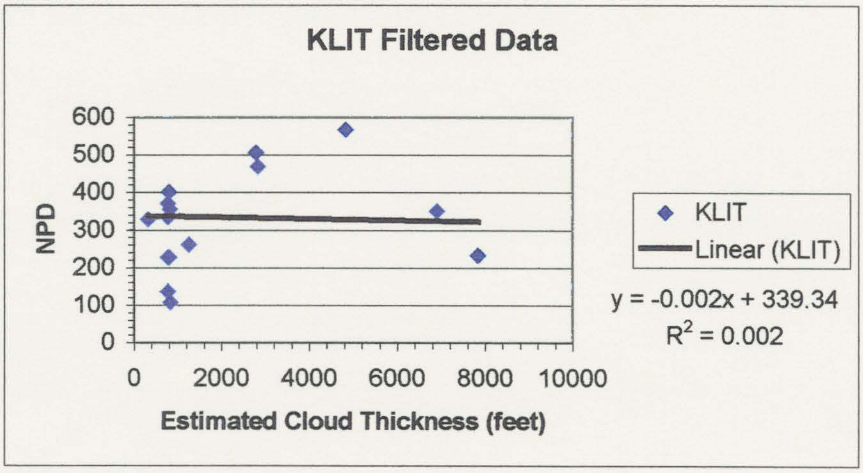

Figure 5.27: Littlerock, AK (KLIT) NPD value versus estimated cloud thickness. Filtered data with linear best fit.

Results are tabulated in Table 5.2, and indicate poor correlation both prior to filtering and after filtering. Although the majority of sites showed some improvement after filtering for rain events, precipitating clouds, and multiple cloud layers, the correlation (R^2) still remains poor.

Site (ICAO)	Sample Size (Unfiltered Data)	Sample Size (Filtered Data)	Unfiltered R^2 (Correlation)	Filtered R^2 (Correlation)
KACT	42	13	.036	.025
KAUS	219	51	.002	.013
KRIV	95	66	.031	.021
KDAL	163	27	.043	.060
KTUS	109	12	.000	.028
KFLG	55	14	.001	.018
KFSM	51	17	.050	.053
KHOB	57	22	.143	.237
KJAN	77	13	.069	.345
KLFK	52	17	.007	.034
KLIT	125	21	.001	.002

Table 5.2: List of sample sizes prior to, and after removing multiple layers, and possible precipitating clouds. Also, calculated correlation squared before and after filtering.

5.3 Error Analysis

One of the primary error sources was the use of an uncorrected atmosphere. The mean effective surface emissivities ranged from approximately 0.93 to 0.98, and based on the Bayesian Water-vapor Retrieval model indicate as much as a 3.5% error in the brightness temperature difference at 85.5 GHz (See BWR graphs below). Coincidentally, prior work by Jones et al. indicates approximately 3.5% atmospheric correction at 85.5H GHz. A larger atmospheric correction is present for the horizontal polarizations than for the vertical polarizations, as would be expected from their lower effective microwave values (see Figure 4) [Jones and Vonder Haar, 1997]. This is expected since the brightness temperature difference is proportional to the effective surface emittance difference,

$$\Delta T_B \approx \Delta\varepsilon(T_S - T_a)\tau$$

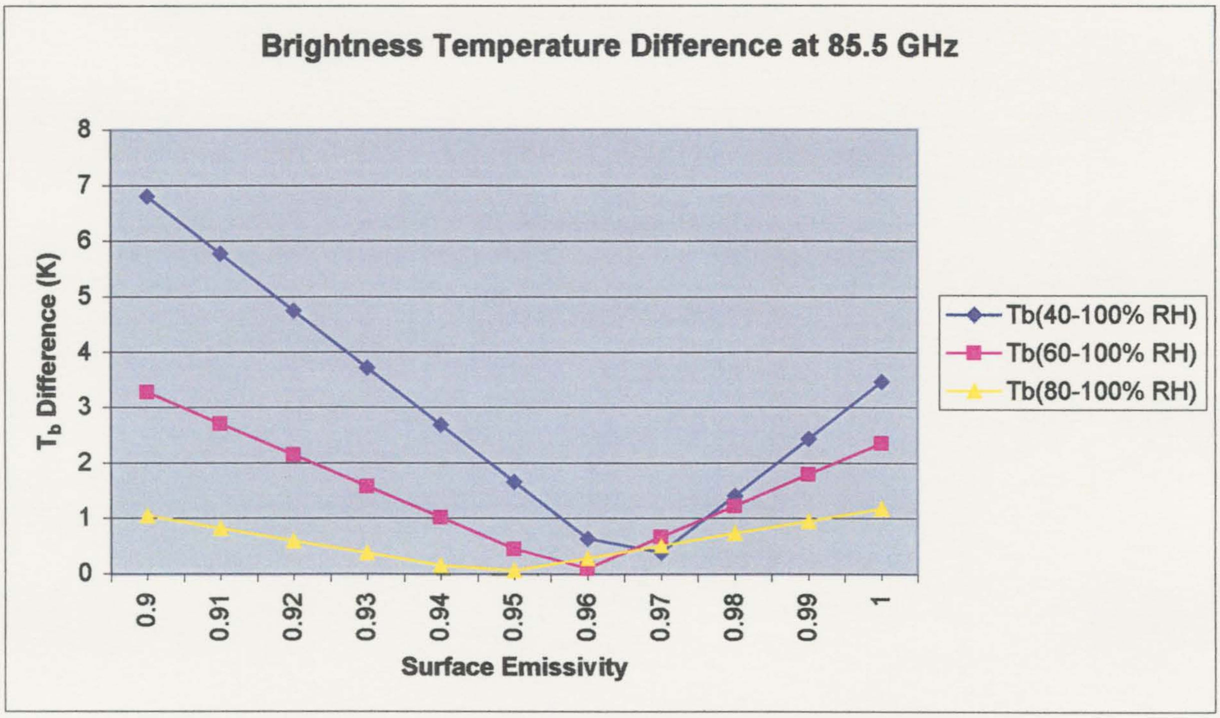

Figure 5.28: Model-simulated brightness temperature polarization difference as a function of surface emissivity. Several different relative humidity profiles differenced with worst case (100% relative humidity) using a standard midlatitude summer sounding.

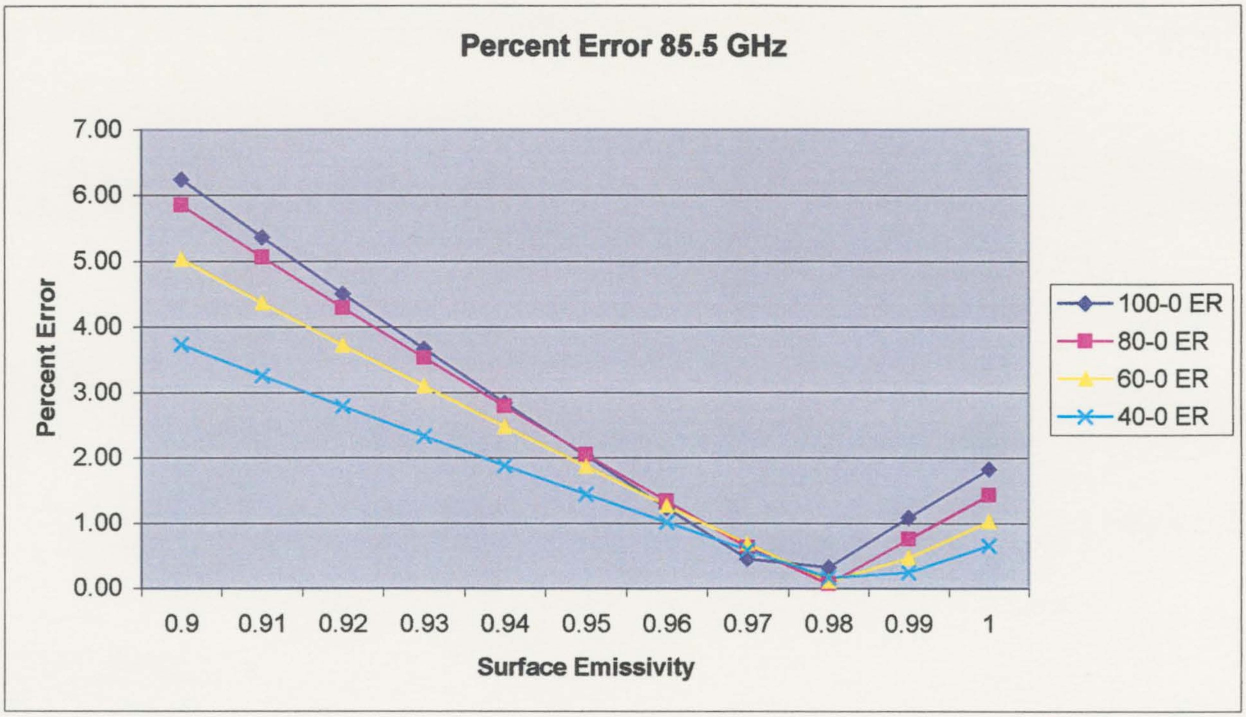

Figure 5.29: Model-simulated error percentage for brightness temperature polarization difference as a function of surface emissivity. Four different relative humidity profiles differenced with best case (0% relative humidity) using a standard midlatitude summer sounding.

Based on figures 5.28 and 5.29, and the mean effective surface emissivities in Table 4.1, we would expect approximately 0.7-1.7K errors in the brightness temperature polarization differences (ΔT_B) due to the uncorrected atmosphere.

Uncertainty in the effective surface emissivity (Table 4.1) also resulted in very large errors in the $\Delta\varepsilon$, and therefore resulted in large errors in NPD. Using the mean ΔT_B values from Table 5.3 for each site, the relative uncertainties (percentage) were as follows: KACT (89%), KAUS (41%), KDAL (37%), KFLG (121%), KFSM (65%), KHOB (39%), KJAN (123%), KLFK (200%), KLIT (57%), KRIV (47%), and KTUS

(53%). Sites with marginal and poor $\Delta\varepsilon$ were affected more severely since they had larger relative uncertainties in $\Delta\varepsilon$ values.

Errors in NPD values due to instrument noise ($\pm$ 1.5K) were also significant. Using the mean ΔT_B values from Table 5.3 for each site, the relative uncertainties (percentage) were as follows: KACT (56%), KAUS (52%), KDAL (31%), KFLG (50%), KFSM (55%), KHOB (29%), KJAN (52%), KLFK (75%), KLIT (44%), KRIV (27%), and KTUS (34%).

5.4 Horizontal Variability of Key Parameters

The horizontal variability of key parameters was calculated over a 5 x 5 grid centered on the applicable site. Key parameters such as the effective surface emissivity, microwave brightness temperature, infrared brightness temperature, and NPD value were calculated. First, the mean value and standard deviation of the parameter was calculated for each site and pass. Then the mean and standard deviations were binned into approximately 7 to 10-day bins and the mean was calculated along with the standard deviation. Finally, the 90-day mean, standard deviation (absolute uncertainty), and relative uncertainty were calculated for each site.

Site (ICAO)	T_{IR}	$\Delta\varepsilon$	ΔT_B	NPD
KACT	281.62 $\pm$ 5.43 (1.93%)	0.010 $\pm$ 0.002 (19.68%)	2.70 $\pm$ 1.42 (52.59%)	271.61 $\pm$ 136.27 (50.17%)
KAUS	283.72 $\pm$ 6.84 (2.41%)	0.010 $\pm$ 0.003 (29.46%)	2.88 $\pm$ 1.53 (53.18%)	284.39 $\pm$ 144.88 (50.94%)
KDAL	282.76 $\pm$ 6.47 (2.29%)	0.018 $\pm$ 0.004 (22.58%)	4.73 $\pm$ 1.87 (39.60%)	263.57 $\pm$ 95.53 (36.24%)
KFLG	274.91 $\pm$ 7.27 (2.64%)	0.010 $\pm$ 0.004 (36.05%)	3.01 $\pm$ 1.82 (60.45%)	308.17 $\pm$ 180.08 (58.43%)
KFSM	278.30 $\pm$ 4.82	0.009 $\pm$ 0.003	2.72 $\pm$ 1.59	299.49 $\pm$ 157.05

	(1.73%)	(30.54%)	(58.55%)	(52.44%)
KHOB	286.92 ± 4.11 (1.43%)	0.019 ± 0.002 (11.68%)	5.20 ± 1.22 (23.46%)	276.09 ± 64.96 (23.53%)
KJAN	272.87 ± 6.42 (2.35%)	0.009 ± 0.004 (42.59%)	2.89 ± 1.57 (54.23%)	346.16 ± 165.80 (47.90%)
KLFK	286.40 ± 3.53 (1.23%)	0.006 ± 0.002 (27.91%)	2.01 ± 1.41 (70.30%)	321.97 ± 215.67 (66.98%)
KLIT	269.57 ± 4.46 (1.65%)	0.011 ± 0.004 (31.30%)	3.40 ± 1.68 (49.58%)	315.45 ± 145.11 (46.00%)
KRIV	287.91 ± 1.99 (0.69%)	0.020 ± 0.006 (30.87%)	5.64 ± 2.65 (46.96%)	281.11 ± 123.73 (44.01%)
KTUS	289.41 + 2.99 (1.03%)	0.015 + 0.005 (30.06%)	4.34 + 1.93 (44.58%)	282.99 + 109.81 (38.81%)

Table 5.3: The 90-Day (June 1-Aug 31 1998) Mean and Absolute uncertainty for 10.8 μm infrared temperature (T_{IR}), polarization difference ($\Delta\varepsilon$), microwave brightness temperature difference (ΔT_B), and NPD value. Relative uncertainty (percentage) is in parentheses.

Chapter 6

Summary and Conclusions

6.1 Preliminary Conclusions

This study focused on using a new method, the Normalized Polarization Difference (NPD) method, on the problem of detecting low clouds, with bases below 10,000 feet, over the Southwestern United States. This area had the general characteristics necessary for the NPD method to succeed: significant surface emissivity polarization difference above the background signal; and relatively uniform horizontal characteristics. The study attempted to simplify the NPD method so it could be applied quickly and effectively to data-sparse, and data-denied regions of the world. The primary goal was to develop a quick-turn product for use by the military as a means of evaluating the weather conditions under a mid- or upper-layer of clouds.

Preliminary results indicate that the NPD method (without atmospheric corrections) didn't work very well over land using the stated simplifications. This was clearly evident in the graphs displaying the linear best fit and correlation values. Correlation values showed very poor correlation, at best. The removal of possible precipitating clouds, and multiple-layered clouds improved the correlation values at most test sites, however, values still remained low.

Four primary error sources were identified and quantified. The use of an uncorrected atmosphere resulted in a 0.7-1.7 K error. As a rough approximation, horizontal variations were examined over the 5x5 grid box. This resulted in very large variations in the infrared temperature on the scale of 2.0-7.3K. One of the more significant was instrument noise (NEΔT). The instrument noise, NEΔT, for 85V was 0.52K and 0.93K for 85H. Since the NPD method is a differencing method, accuracy could approach 1.5K. The effective surface emissivity relative uncertainties ranged from 0.22-1.16%. Part of this error could be attributable to unfiltered wet ground events, and are included in the absolute uncertainty of the measurements. Based on the significant error sources, errors in NPD were calculated using mean values of ΔT_B and $\Delta\varepsilon$, and showed significant relative uncertainties (see Table 5.3).

Additional contributing errors could be due to (1) error in the Bayesian Water-vapor retrieval (BWR) model (Forward mode) and Liebe's MPM92; (2) Precipitating clouds not filtered by the modified-Grody algorithm; (3) Errors in the binning method; (4) Errors due to fractional cloud coverage within the instrument FOV; (5) Error in estimating cloud top height (pressure) using the infrared brightness temperature; (6) Error in estimating cloud thickness using the nearest atmospheric sounding. The use of the atmospheric sounding was intended to mitigate error in estimation of cloud top height rather than using the more inaccurate standard midlatitude summer sounding and IR brightness temperature; or (7) Errors in the observed cloud height, and coverage.

6.2 Applications and Further Work

This work attempted to simplify previous work, and decrease the reliance on atmospheric corrections. In order to develop a quick-turn, cloud identification product, the NPD method clearly requires coincident sounding data and passive microwave data. This may be feasible with future sensor suites such as the SSM/IS. Further reductions in instrument noise would also lead to improved results. Increased temporal and spatial resolution, such as building a passive microwave radiometer on a future geostationary platforms, would also improve over-land results. Additonally, multi-spectral techniques could be used to eliminate wet ground events, and precipitating clouds.

References

Baird, D.C., 1988: *Experimentation, An Introduction to Measurement Theory and Experiment Design*. Prentice Hall, Englewood Cliffs, NJ., 193 pp.

Chandrasekhar, S., 1960: *Radiative Transfer*. Dover Publications Inc., New York, 393 pp.

Chauhan, N.S., 1997: Soil moisture estimation under a vegetation cover: combined active passive microwave remote sensing approach. *Int. J. Remote Sensing*, **18**, 1079-1097.

Choudhury, B.J., T.J. Schmugge, R.W. Newton, and A. Chang, 1979: Effect of surface roughness on the microwave emission from soils. *J. Geophys. Res.*, **84**, 5699-5706.

Combs, C., et al., 1998: Satellite detection of cloud liquid water over land using polarization differences at 85.5 GHz. *Geophys. Res. Ltrs.*, **25**, 75-78.

Deirmendjian, D., 1963: Complete microwave scattering and extinction properties of poly-dispersed cloud and rain elements. Rand Corp. Rep. 12-422-PR, Santa Monica, California, 54 pp.

Diak, G., 1995: Column cloud liquid water amounts for nonprecipitating clouds versus an "effective cloud fraction" derived from microwave data: a simulation study. *J. Atmos. Oceanic Tech.*, **12**, 960-969.

Elgered, G., et al., 1982: Measurements of atmospheric water vapor with microwave radiometry. *Radio Science*, **17**, 1258-1264.

Espenshade, E.B., Editor, 1990: *Goode's World Atlas, 18th Ed.* Rand McNally, Chicago, 367 pp.

Greenwald, T.J., et al., 1993: A physical retrieval of cloud liquid water over the global oceans using special sensor microwave/imager (SSM/I) observations. *J. Geophys. Res.*, **98**, 18471-18488.

Greenwald, T., et al., 1997: Further developments in estimating cloud liquid water over land using microwave and infrared satellite measurements. *J. Applied Met.*, **36**, 390-405.

Greenwald, T., et al., 1999: Error estimates of spaceborne passive microwave retrievals of cloud liquid water over land. *IEEE Trans. on Geoscience and Remote Sensing*, **37**, 796-804.

Grody, N., 1976: Remote sensing of atmospheric water content from satellites using microwave radiometry. *IEEE Trans. on Antennas and Propagation*, **AP-24**, 155-162.

Gunn, K.L.S., and T.W.R. East, 1954: The microwave properties of precipitation particles. *Quart. J. Royal Meteor. Soc.*, **80**, 522-545.

Hollinger, J., R. Lo, G. Poe, R. Savage, and J. Peirce, 1987: *Special Sensor Microwave/ Imager user's guide.* Naval Research Laboratory, Washington, D.C., 120 pp.

Heggli, M., R.M. Rauber, and J.B. Snider, 1987: Field evaluation of a dual-channel microwave radiometer designed for measurements of integrated water vapor and cloud liquid water in the atmosphere. *J. Atmos. and Oceanic Tech.*, **4**, 204-213.

Hogg, D.C., et al., 1982: A steerable dual-channel microwave radiometer for measurement of water vapor and liquid in the troposphere. *J. Climate and Appl. Met.*, **22**, 793-806.

Huang, H.L., and G.R. Diak, 1992: Retrieval of nonprecipitating liquid water cloud parameters from microwave data: a simulation study. *J. Atmos. and Oceanic Tech.*, **9**, 354-363.

Janssen, M.A., 1993: *Atmospheric Remote Sensing by Microwave Radiometry.* John Wiley and Sons, New York, NY., 592 pp.

Jones, A.S., and T.H. Vonder Haar, 1990: Passive remote sensing of cloud liquid water over land regions. *J. Geophys. Res*, **95**, 16673-16683.

Jones, A.S., and T.H. Vonder Haar, 1997: Retrieval of microwave surface emittance over land using coincident microwave and infrared satellite measurements. *J. Geophys. Res*, **102**, 13609-13626.

Jones, A.S., K.E. Eis, and T.H. Vonder Haar, 1995: A method for multisensor-multispectral satellite data fusion. *J. Atmos. and Oceanic Tech.*, **00**, 1-16.

Jones, A.S., and T.H. Vonder Haar, 2001: Overview of an HDF-EOS based parallel data-computing environment for multisensor satellite data merger and scientific analysis. *17th Conf. On Interactive Information and Processing Systems (IIPS) 14-19 Jan 2001.*

Kidder, S.Q., and T.H. Vonder Haar, 1995: *Satellite Meteorology, An Introduction.* Academic Press, San Diego, CA., 466 pp.

Kummerow, C., 1998: Beamfilling errors in passive microwave rainfall retrievals. *J. Applied Met.*, **37**, 356-370.

Kummerow, C., and W. Barnes, 1998: The tropical rainfall measuring mission (TRMM) sensor package. *J. Atmos. and Oceanic Tech.*, **15**, 809-817.
Liebe, H.J., 1981: Modeling attenuation and phase of radio waves in air at frequencies below 1000 GHz. *Radio Science*, **16**, 1183-1199.

Liebe, H.J., and G.G. Gimmestad, 1978: Calculation of clear air EHF refractivity. *Radio Sci.*, **13**, 245-251.

Liebe, H.J., and K.C. Allen, 1983: Tropospheric absorption and dispersion of millimeter and submillimeter waves. *Trans. Antennas and Propagation*, **AP-31**, 221-223.

Liou, K., 1980: *An Introduction to Atmospheric Radiation.* Academic Press, San Diego, CA., 392 pp.

Liou, K., 1992: *Radiation and Cloud Processes in the Atmosphere.* Oxford University Press, New York, NY., 487 pp.

Liu, Q., and C. Simmer, 1996: Polarization and intensity in microwave radiative transfer. *Beitr. Phys. Atm.*, **69**, 535-545.

McClatchey, R.A., R.W. Fenn, J.E. Selby, F.E. Voltz, and J.S. Garing, 1972: *Optical properties of the atmosphere. 3d. ed. AFCRL Environmental Research Paper 411, 108 pp.* [Available from Air Force Cambridge Laboratories, L.G. Hanscom Field, Bedford, MA 01731.]

Newton, R.W., Q.R. Black, S. Makanvand, A.J. Blanchard, and B.R. Jean, 1982: Soil moisture information and thermal microwave emission. *IEEE Trans. Geosci. Remote Sensing*, **GE-20**, 275-281.

Njoku, E.G., 1982: Passive microwave remote sensing of the earth from space: a review. *Proceedings of the IEEE*, **70**, 728-750.

Popa Fotino, I.A, J.A. Schroeder, and M.T. Decker, 1986: Ground-based detection of aircraft icing conditions using microwave radiometers. *IEEE Trans. Geosci. And Remote Sensing*, **GE-24**, 975-982.

Pruppacher, H.R., and J.D. Klett, 1978: *Microphysics of Clouds and Precipitation.* D. Reidel Publishing Co., Boston, 714 pp.

Reitz, J.R., F.J. Milford, and R.W. Christy, 1979: *Foundations of Electromagnetic Theory*, Addison-Wesley Publishing Co., 534 pp.

Schmugge, T.J., T.J. Jackson, and H.L. McKim, 1980: Survey of methods for soil moisture determination. *Water Resources Res.*, **16**, 961-979.

Schmugge, T.J., B.J. Choudhury, 1981: A comparison of radiative transfer models for predicting the microwave emission from soils. *Radio Sci.*, **16**, 927-938.

Schmugge, T.J., 1983: Remote sensing of soil moisture: recent advances. *IEEE Trans. Geosci. And Remote Sensing*, **GE-21**, 336-344.

Schmugge, T.J., 1985: Remote sensing of soil moisture. *Hydrological Forecasting*, M.G. Anderson and T.P. Burt, Eds., Wiley, New York.

Spencer, R.W., H.M. Goodman, and R.E. Hood, 1989: Precipitation retrieval over land and ocean with the SSM/I: Identification and characteristics of the scattering signal. *J. Atmos. and Oceanic Tech.*, **6,** 254-273.

Staelin, D.H., et al., 1976: Remote sensing of atmospheric water vapor and liquid water with the nimbus 5 microwave spectrometer. *J. Appl. Met.*, **15**, 1204-1214.

Stephens, G.L., 1980: Radiative properties of cirrus clouds in the infrared region. *J. Atmos. Sci.*, **37**, 435-446.

Stephens, G.L., 1994: *Remote Sensing of the Lower Atmosphere*. Oxford University Press, New York, NY., 523 pp.

Ulaby, F.T., R.K. Moore, and A.K. Fung, 1981: *Microwave Remote Sensing Active and Passive, Vol. I Microwave Remote Sensing Fundamentals and Radiometry*. Artech House, Norwood, Mass., 456 pp.

Ulaby, F.T., R.K. Moore, and A.K. Fung, 1981: *Microwave Remote Sensing Active and Passive, Vol. II Radar Remote Sensing and Surface Scattering and Emission Theory*. Artech House, Norwood, Mass., 608 pp.

Ulaby, F.T., R.K. Moore, and A.K. Fung, 1981: *Microwave Remote Sensing Active and Passive, Vol. III From Theory to Application*. Artech House, Norwood, Mass., 1098 pp.

Van Vleck, J.H., 1947: The absorption of microwaves by uncondensed water vapor. *Physical Review*, **71**, 425-433.

Wang, J.R., and T.J. Schmugge, 1980: An empirical model for the complex dielectric permittivity of soils as a function of water content. *IEEE Trans. Geosci. And Remote Sensing*, **GE-18**, 288-295.

Westwater, E.R., 1972: Microwave emission from clouds. NOAA Tech. Rep. 219-WPL-18, Boulder, Colorado, 43 pp.

Wilheit, T.T., 1978: A review of applications of microwave radiometry to oceanography. *Boundary Layer Met.*, **13**, 277-293.

Wilheit, T.T., and A.T.C. Chang, 1977: A satellite technique for quantitatively mapping rainfall rates over the oceans. *J. Appl. Met.*, **16**, 551-560.
Wu, R., and J.A. Weinman, 1984: Microwave radiances from precipitating clouds containing asherical ice, combined phase, and liquid hydrometeors. *J. Geophys. Res.*, **89**, 7170-7178.

Wu, M.C., 1987: Determination of cloud ice water content and geometrical thickness using microwave and infrared radiometric measurements. *J. Clim. Appl. Met.*, **26**, 878-884.

Yeh, H.Y., and K.N. Liou, 1983: Remote sensing of cloud parameters from a combination of infrared and microwave channels. *J. Clim. Appl. Met.*, **22**, 201-213.

Young, K.C., 1993: *Microphysical Processes in Clouds*. Oxford University Press, New York, NY., 427 pp.

Appendix A

Horizontal Variability of Key Parameters

This appendix contains figures depicting the 90-day horizontal variability of key parameters calculated over a 5 x 5 grid centered on the applicable site. The figures show the 90-day mean and the standard deviation of the effective surface emissivity, microwave brightness temperature, infrared brightness temperature, and NPD values, as a function of time (plotted on the "x" axis in approximate 10-day bins) for each of the primary sites.

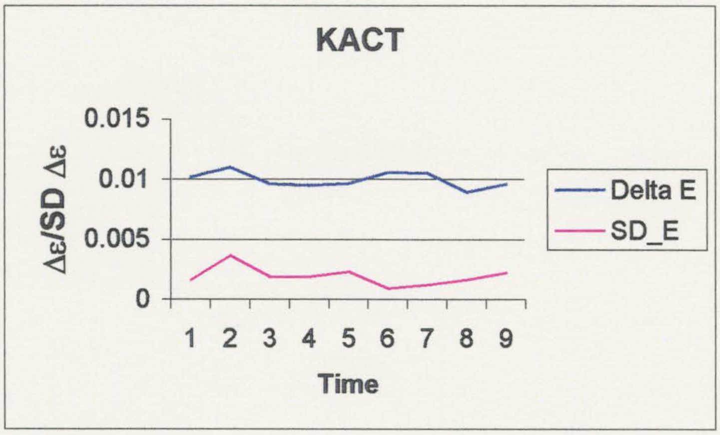

Figure A.1: Waco, TX (KACT) horizontal variation in surface emissivity polarization difference and standard deviation over the 90-day period within the 5x5 grid centered on the primary site.

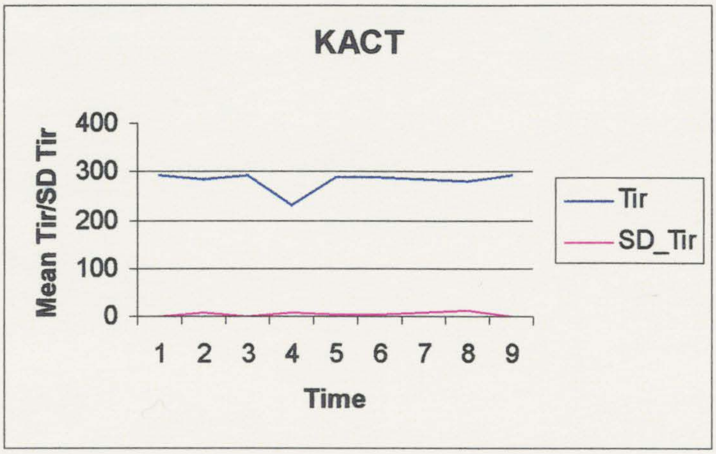

Figure A.2: Waco, TX (KACT) horizontal variation in infrared brightness temperature and standard deviation over the 90-day period within the 5x5 grid centered on the primary site.

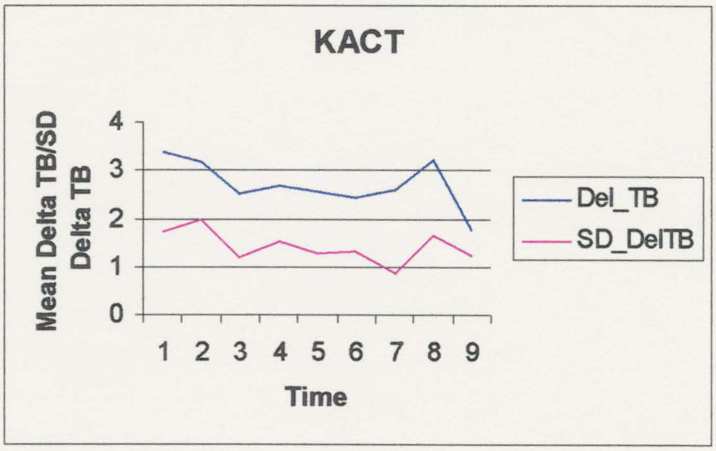

Figure A.3: Waco, TX (KACT) horizontal variation in 85.5 GHz brightness temperature polarization difference and standard deviation over the 90-day period within the 5x5 grid centered on the primary site.

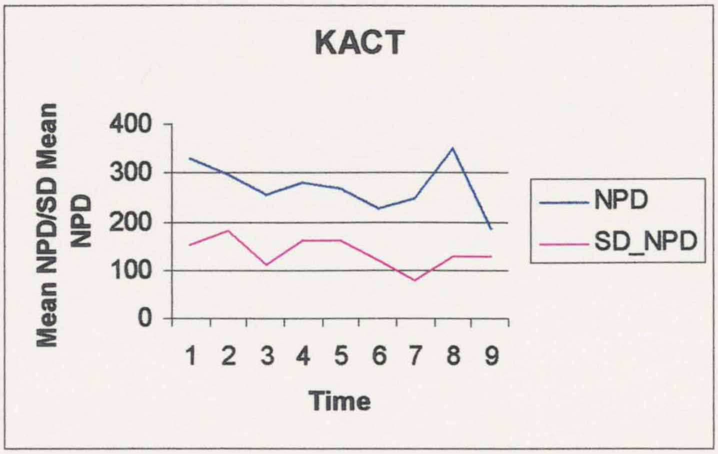

Figure A.4: Waco, TX (KACT) horizontal variation in the NPD value and standard deviation over the 90-day period within the 5x5 grid centered on the primary site.

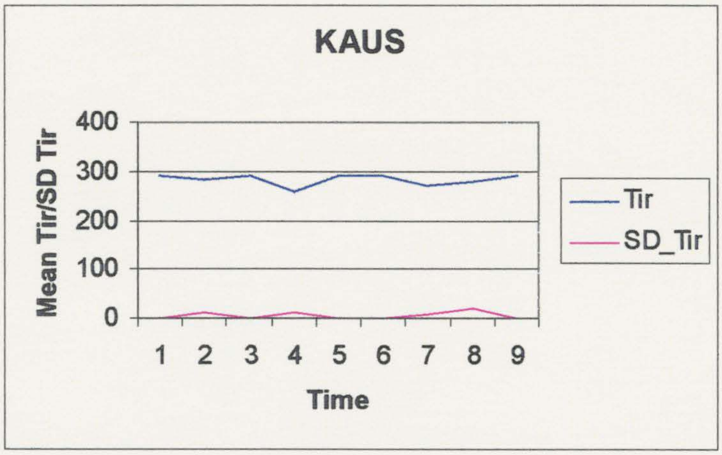

Figure A.5: Austin, TX (KAUS) horizontal variation in infrared brightness temperature and standard deviation over the 90-day period within the 5x5 grid centered on the primary site.

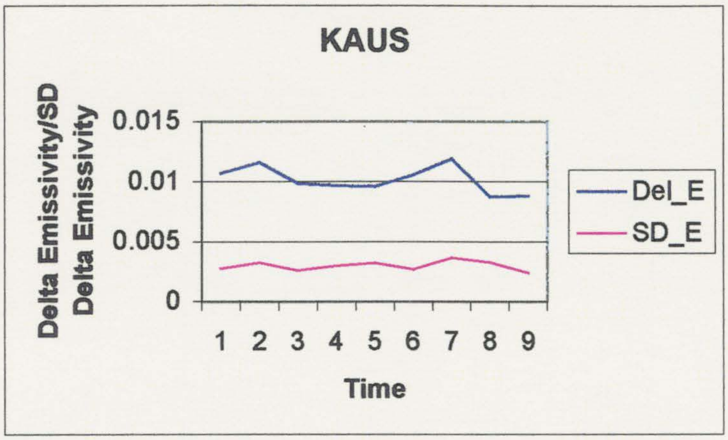

Figure A.6: Austin, TX (KAUS) horizontal variation in surface emissivity polarization difference and standard deviation over the 90-day period within the 5x5 grid centered on the primary site.

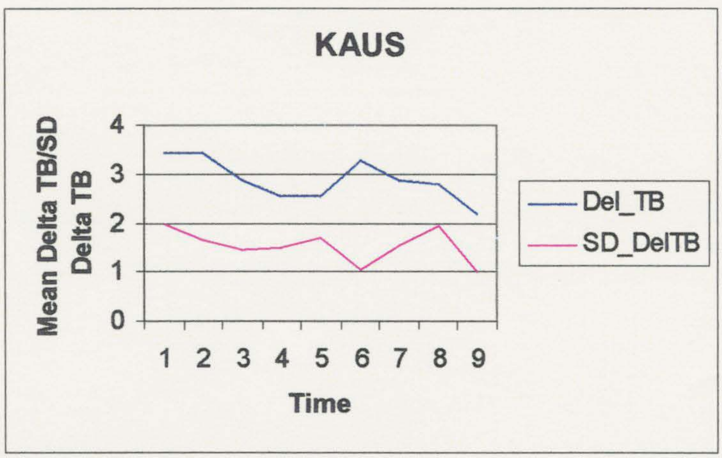

Figure A.7: Austin, TX (KAUS) horizontal variation in 85.5 GHz brightness temperature polarization difference and standard deviation over the 90-day period within the 5x5 grid centered on the primary site.

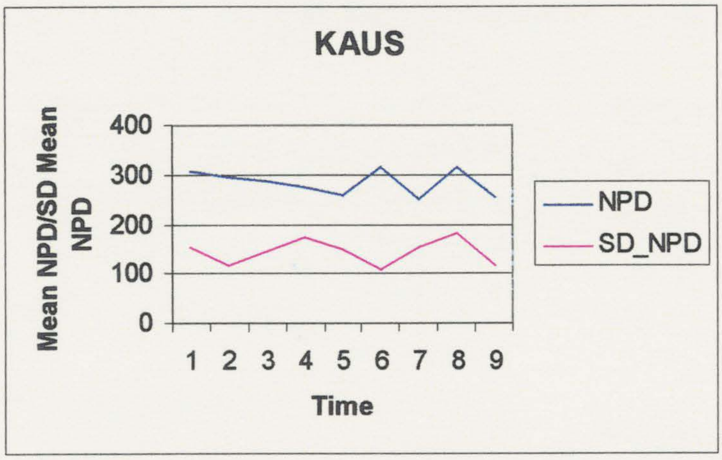

Figure A.8: Austin, TX (KAUS) horizontal variation in the NPD value and standard deviation over the 90-day period within the 5x5 grid centered on the primary site.

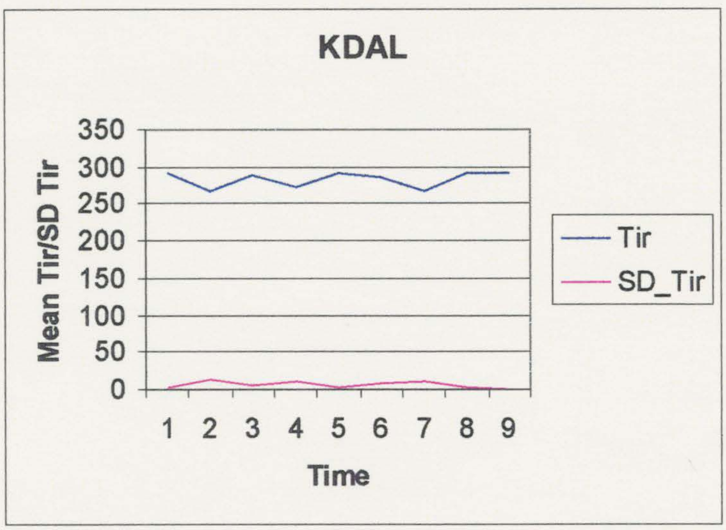

Figure A.9: Dallas, TX (KDAL) horizontal variation in infrared brightness temperature and standard deviation over the 90-day period within the 5x5 grid centered on the primary site.

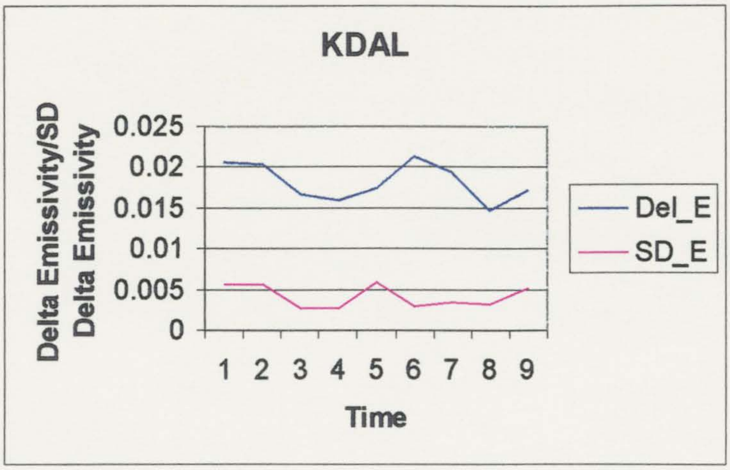

Figure A.10: Dallas, TX (KDAL) horizontal variation in surface emissivity polarization difference and standard deviation over the 90-day period within the 5x5 grid centered on the primary site.

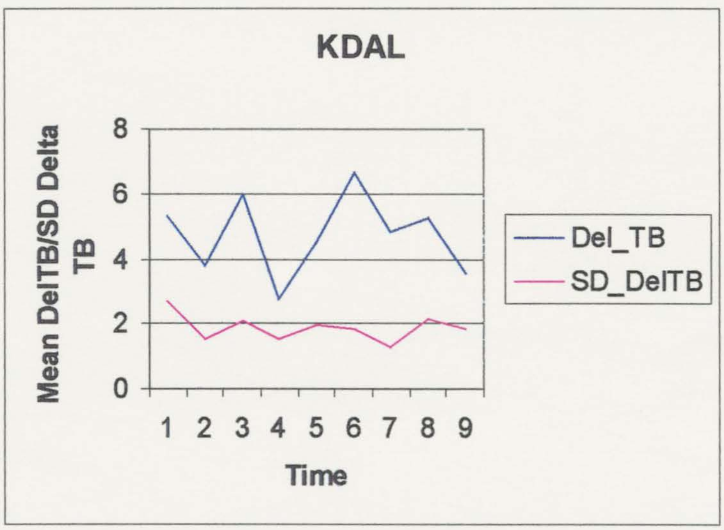

Figure A.11: Dallas, TX (KDAL) horizontal variation in 85.5 GHz brightness temperature polarization difference and standard deviation over the 90-day period within the 5x5 grid centered on the primary site.

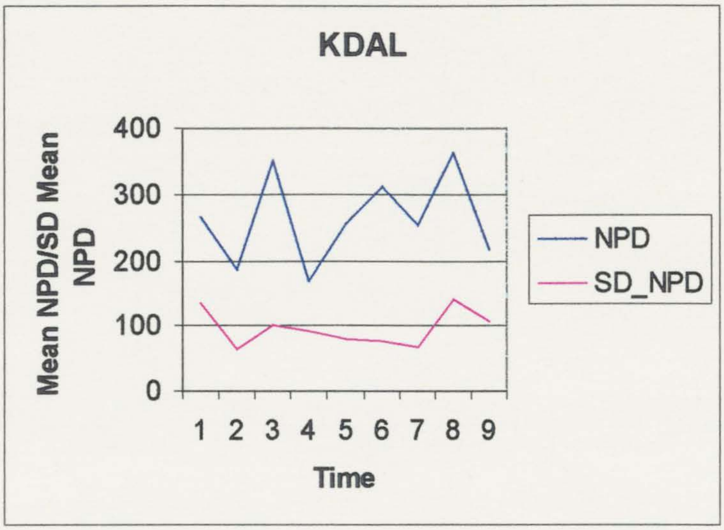

Figure A.12: Dallas, TX (KDAL) horizontal variation in the NPD value and standard deviation over the 90-day period within the 5x5 grid centered on the primary site.

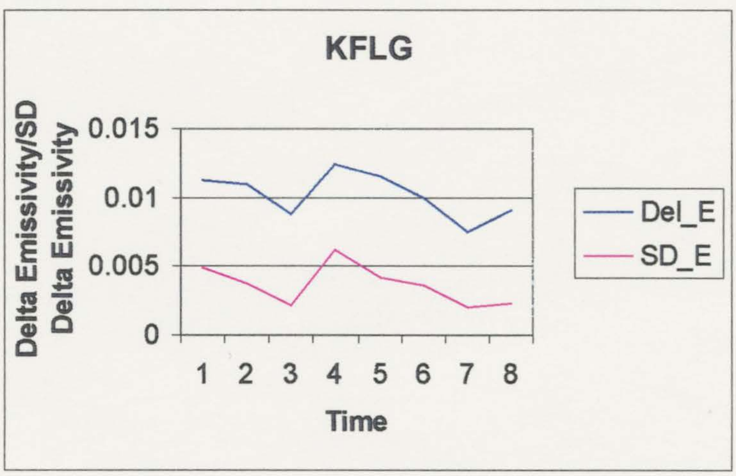

Figure A.13: Flagstaff, AZ (KFLG) horizontal variation in surface emissivity polarization difference and standard deviation over the 90-day period within the 5x5 grid centered on the primary site.

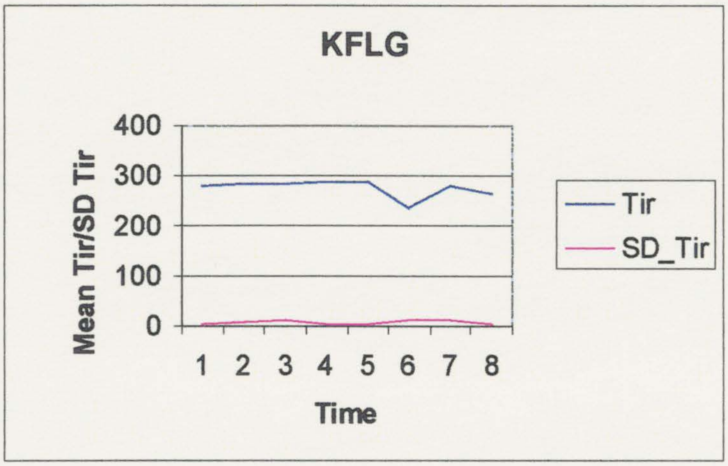

Figure A.14: Flagstaff, AZ (KFLG) horizontal variation in infrared brightness temperature and standard deviation over the 90-day period within the 5x5 grid centered on the primary site.

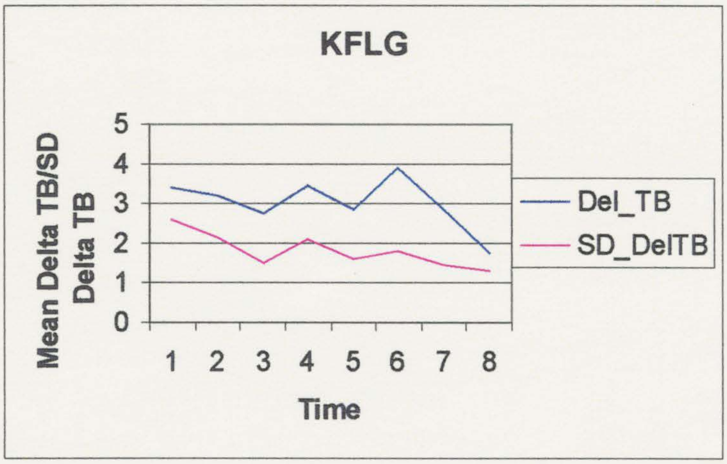

Figure A.15: Flagstaff, AZ (KFLG) horizontal variation in 85.5 GHz brightness temperature polarization difference and standard deviation over the 90-day period within the 5x5 grid centered on the primary site.

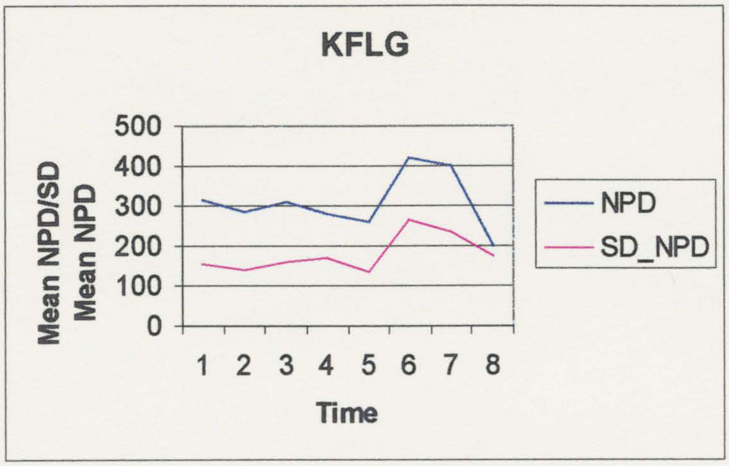

Figure A.16: Flagstaff, AZ (KFLG) horizontal variation in the NPD value and standard deviation over the 90-day period within the 5x5 grid centered on the primary site.

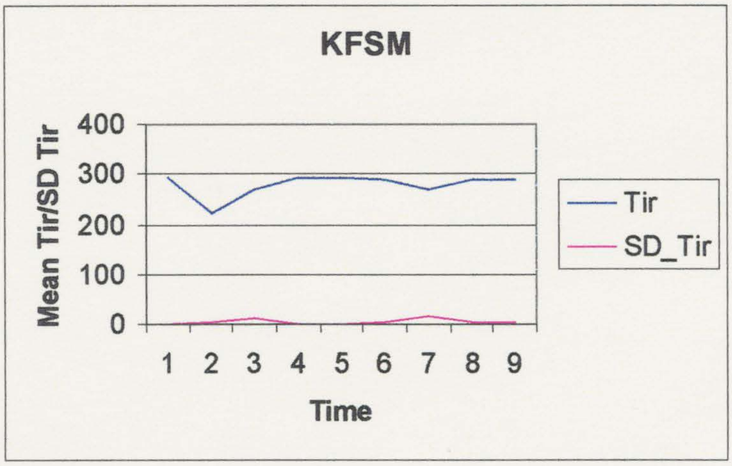

Figure A.17: Fort Smith, AK (KFSM) horizontal variation in infrared brightness temperature and standard deviation over the 90-day period within the 5x5 grid centered on the primary site.

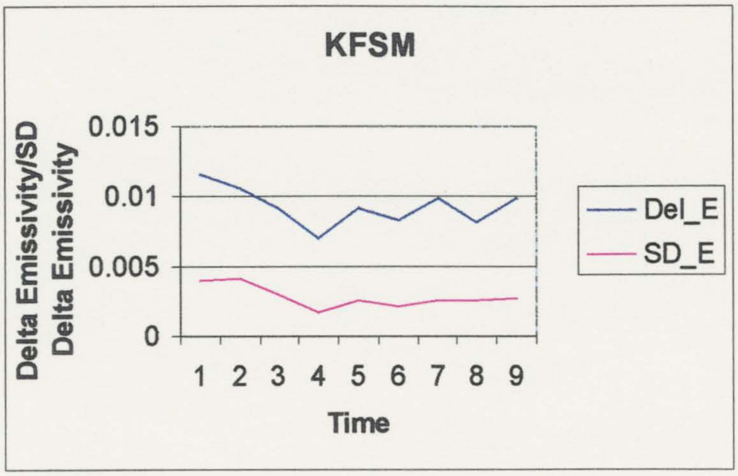

Figure A.18: Fort Smith, AK (KFSM) horizontal variation in surface emissivity polarization difference and standard deviation over the 90-day period within the 5x5 grid centered on the primary site.

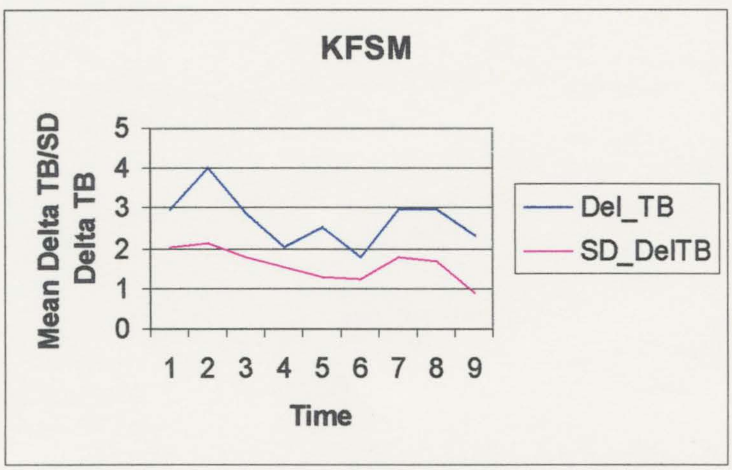

Figure A.19: Fort Smith, AK (KFSM) horizontal variation in 85.5 GHz brightness temperature polarization difference and standard deviation over the 90-day period within the 5x5 grid centered on the primary site.

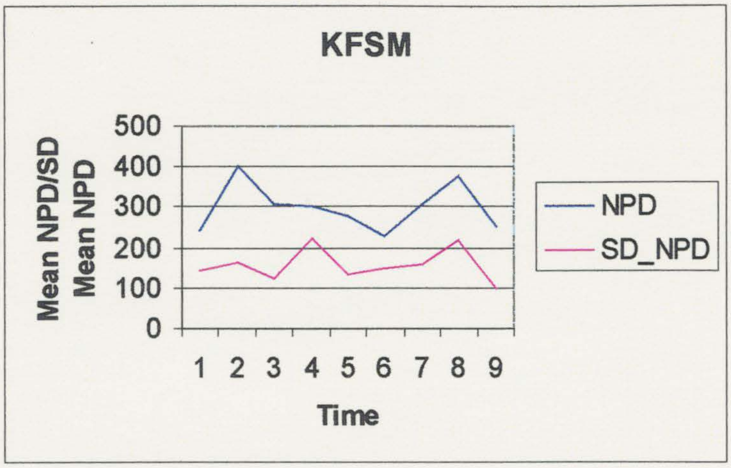

Figure A.20: Fort Smith, AK (KFSM) horizontal variation in the NPD value and standard deviation over the 90-day period within the 5x5 grid centered on the primary site.

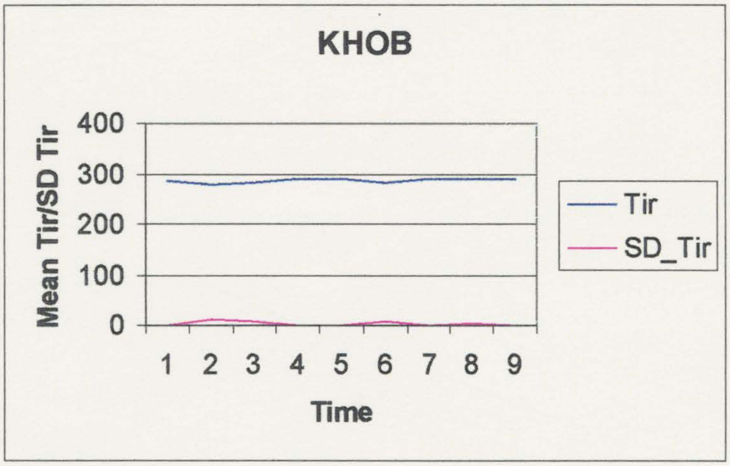

Figure A.21: Hobbs, NM (KHOB) horizontal variation in infrared brightness temperature and standard deviation over the 90-day period within the 5x5 grid centered on the primary site.

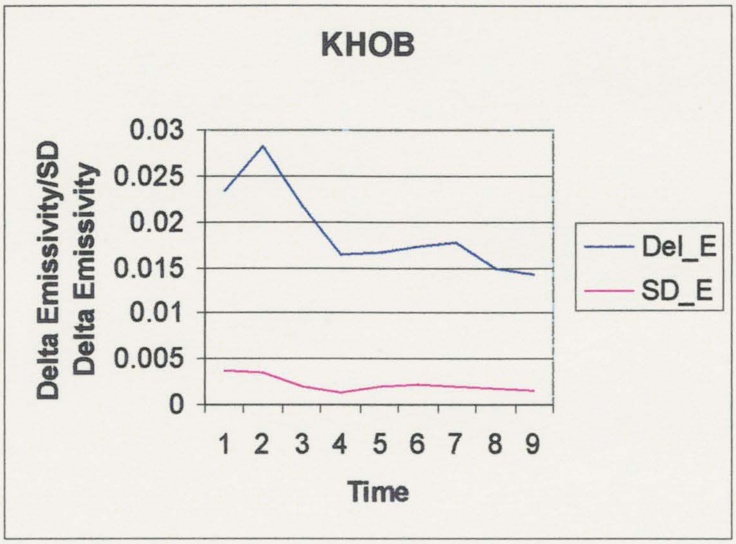

Figure A.22: Hobbs, NM (KHOB) horizontal variation in surface emissivity polarization difference and standard deviation over the 90-day period within the 5x5 grid centered on the primary site.

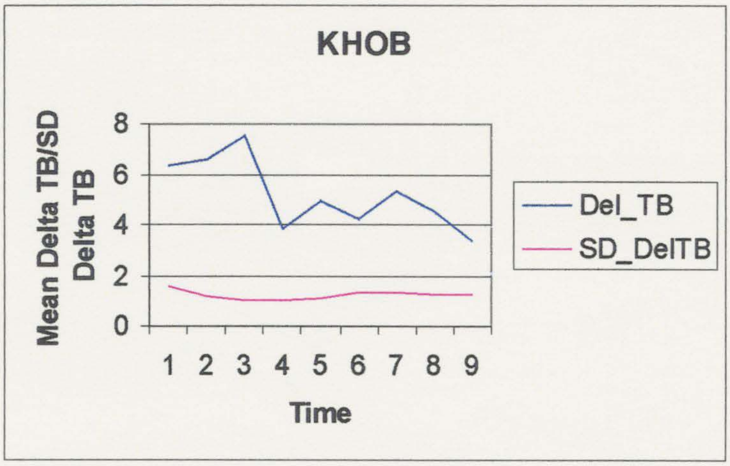

Figure A.23: Hobbs, NM (KHOB) horizontal variation in 85.5 GHz brightness temperature polarization difference and standard deviation over the 90-day period within the 5x5 grid centered on the primary site.

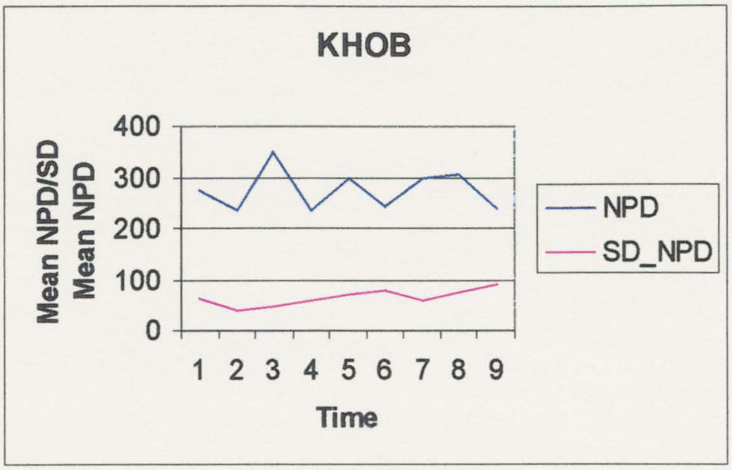

Figure A.24: Hobbs, NM (KHOB) horizontal variation in the NPD value and standard deviation over the 90-day period within the 5x5 grid centered on the primary site.

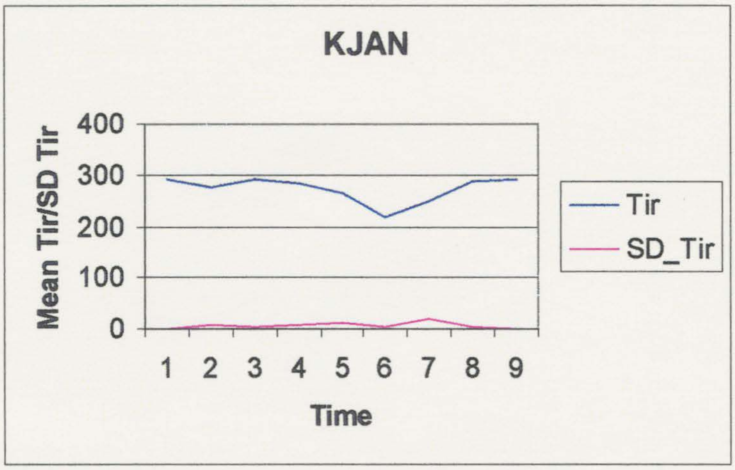

Figure A.25: Jackson, MS (KJAN) horizontal variation in infrared brightness temperature and standard deviation over the 90-day period within the 5x5 grid centered on the primary site.

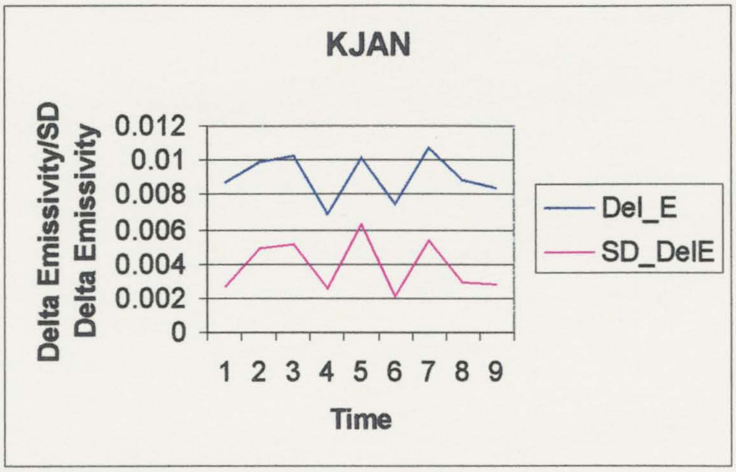

Figure A.26: Jackson, MS (KJAN) horizontal variation in surface emissivity polarization difference and standard deviation over the 90-day period within the 5x5 grid centered on the primary site.

Figure A.27: Jackson, MS (KJAN) horizontal variation in 85.5 GHz brightness temperature polarization difference and standard deviation over the 90-day period within the 5x5 grid centered on the primary site.

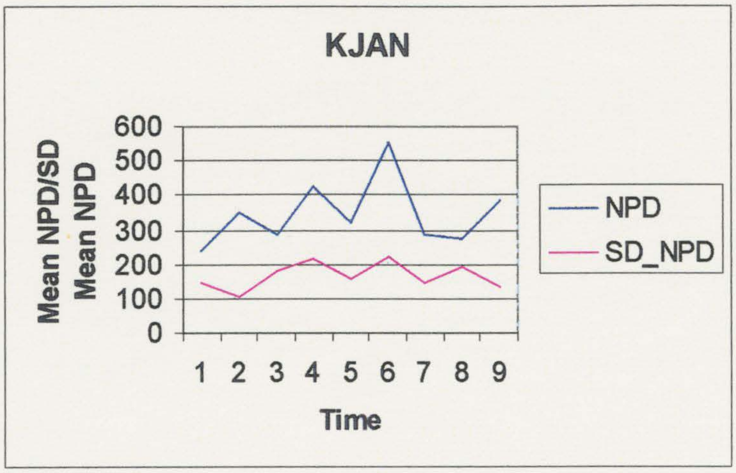

Figure A.28: Jackson, MS (KJAN) horizontal variation in the NPD value and standard deviation over the 90-day period within the 5x5 grid centered on the primary site.

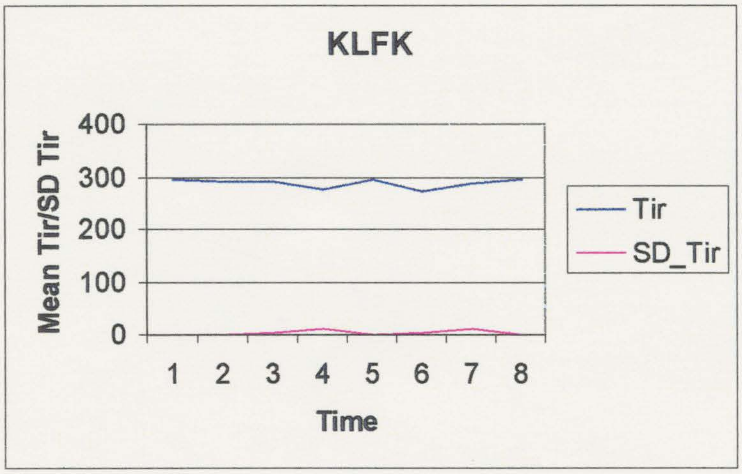

Figure A.29: Lufkin, TX (KLFK) horizontal variation in infrared brightness temperature and standard deviation over the 90-day period within the 5x5 grid centered on the primary site.

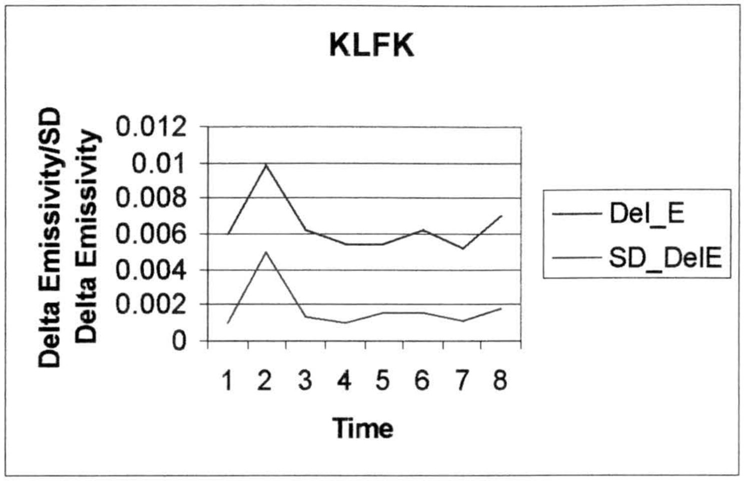

Figure A.30: Lufkin, TX (KLFK) horizontal variation in surface emissivity polarization difference and standard deviation over the 90-day period within the 5x5 grid centered on the primary site.

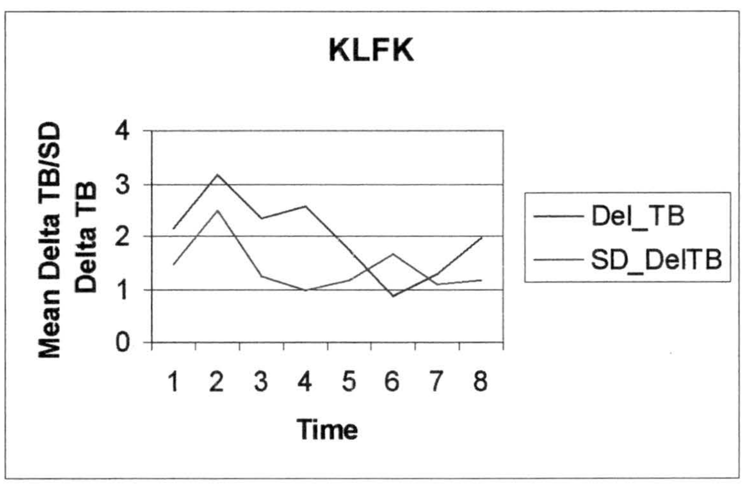

Figure A.31: Lufkin, TX (KLFK) horizontal variation in 85.5 GHz brightness temperature polarization difference and standard deviation over the 90-day period within the 5x5 grid centered on the primary site.

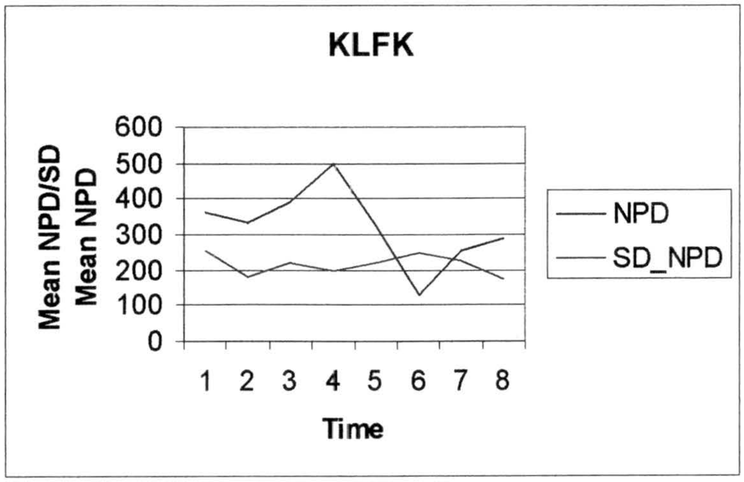

Figure A.32: Lufkin, TX (KLFK) horizontal variation in the NPD value and standard deviation over the 90-day period within the 5x5 grid centered on the primary site.

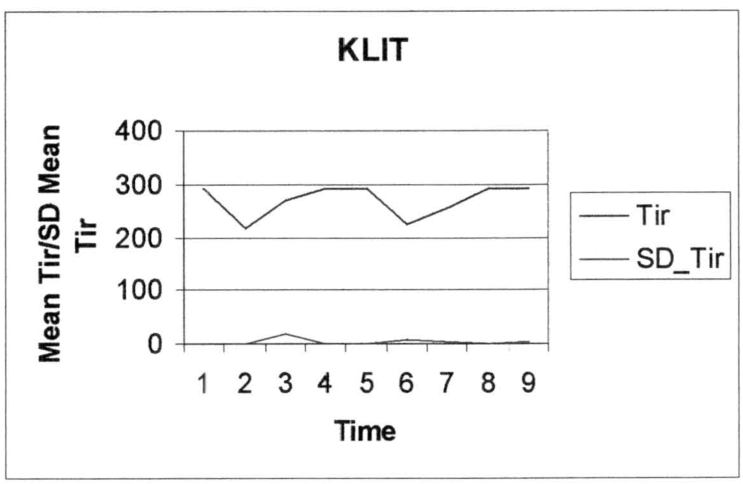

Figure A.33: Little Rock, AK (KLIT) horizontal variation in infrared brightness temperature and standard deviation over the 90-day period within the 5x5 grid centered on the primary site.

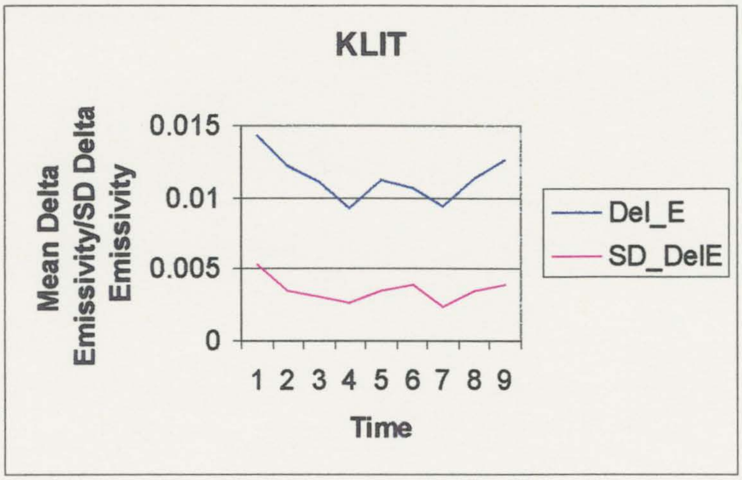

Figure A.34: Little Rock, AK (KLIT) horizontal variation in surface emissivity polarization difference and standard deviation over the 90-day period within the 5x5 grid centered on the primary site.

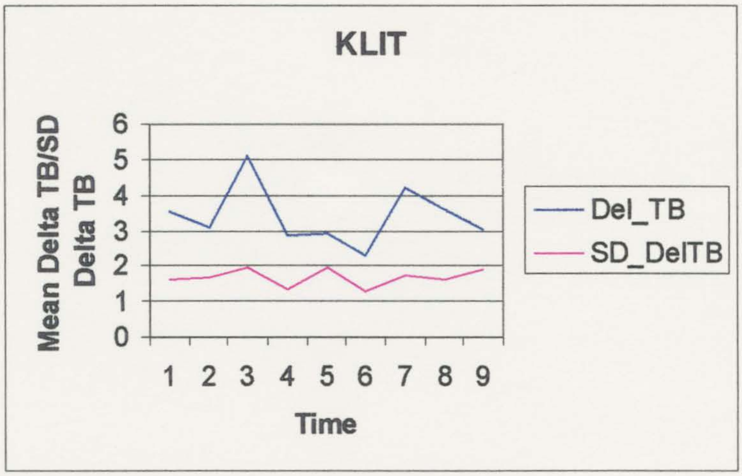

Figure A.35: Little Rock, AK (KLIT) horizontal variation in 85.5 GHz brightness temperature polarization difference and standard deviation over the 90-day period within the 5x5 grid centered on the primary site.

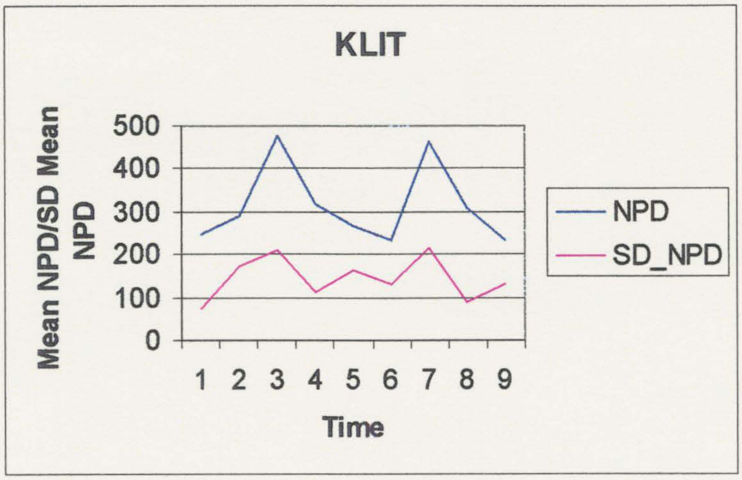

Figure A.36: Little Rock, AK (KLIT) horizontal variation in the NPD value and standard deviation over the 90-day period within the 5x5 grid centered on the primary site.

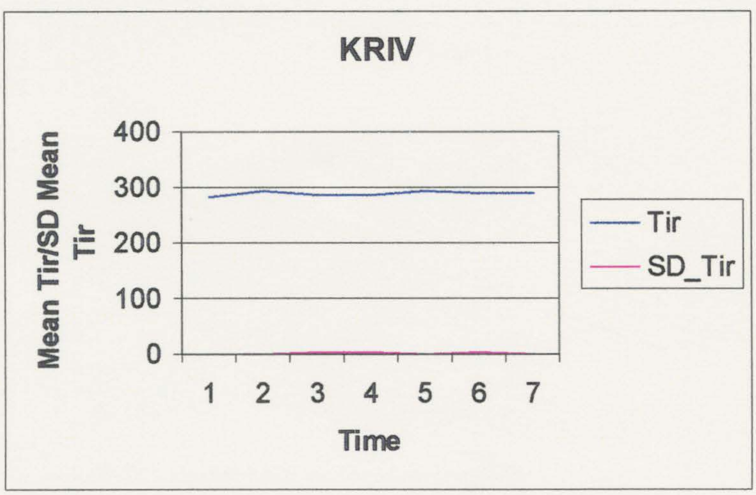

Figure A.37: Riverside, CA (KRIV) horizontal variation in infrared brightness temperature and standard deviation over the 90-day period within the 5x5 grid centered on the primary site.

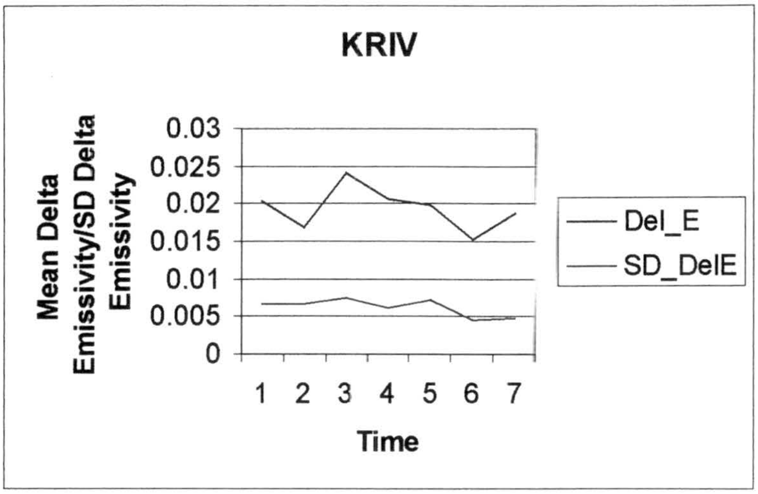

Figure A.38: Riverside, CA (KRIV) horizontal variation in surface emissivity polarization difference and standard deviation over the 90-day period within the 5x5 grid centered on the primary site.

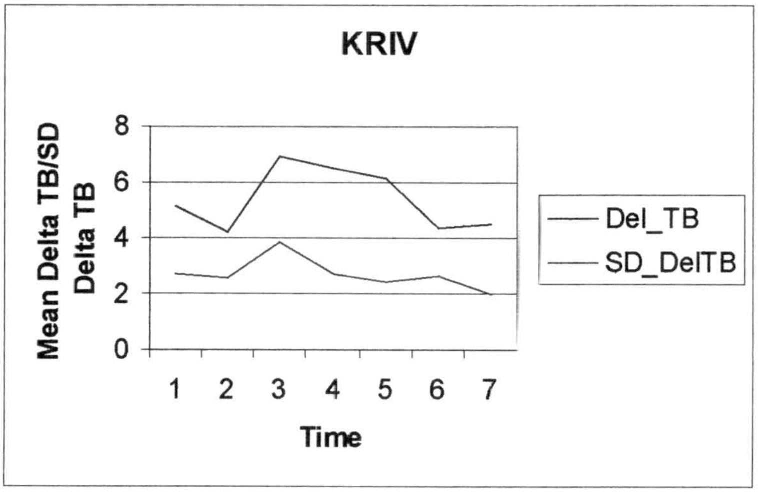

Figure A.39: Riverside, CA (KRIV) horizontal variation in 85.5 GHz brightness temperature polarization difference and standard deviation over the 90-day period within the 5x5 grid centered on the primary site.

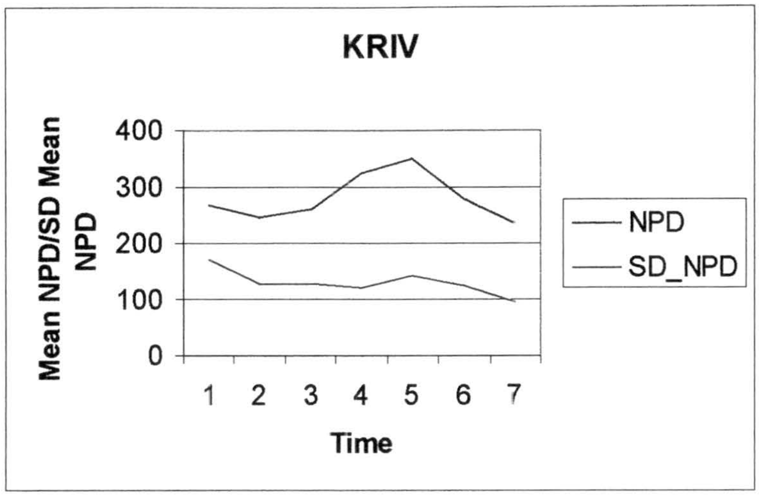

Figure A.40: Riverside, CA (KRIV) horizontal variation in the NPD value and standard deviation over the 90-day period within the 5x5 grid centered on the primary site.

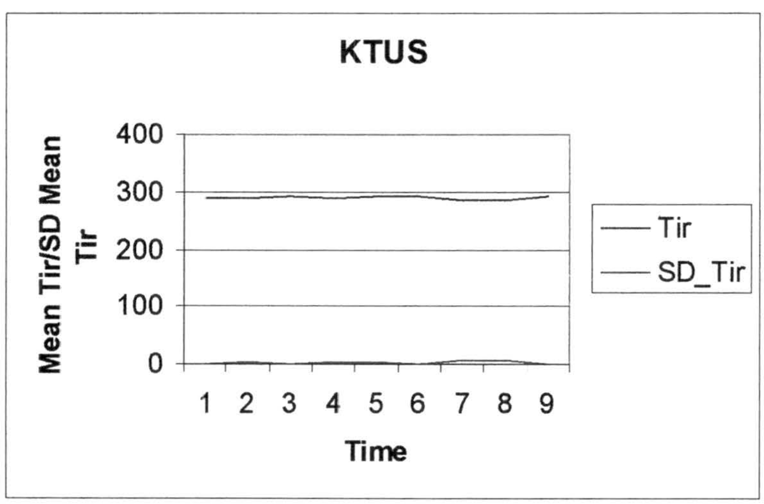

Figure A.41: Tucson, AZ (KTUS) horizontal variation in infrared brightness temperature and standard deviation over the 90-day period within the 5x5 grid centered on the primary site.

Figure A.42: Tucson, AZ (KTUS) horizontal variation in surface emissivity polarization difference and standard deviation over the 90-day period within the 5x5 grid centered on the primary site.

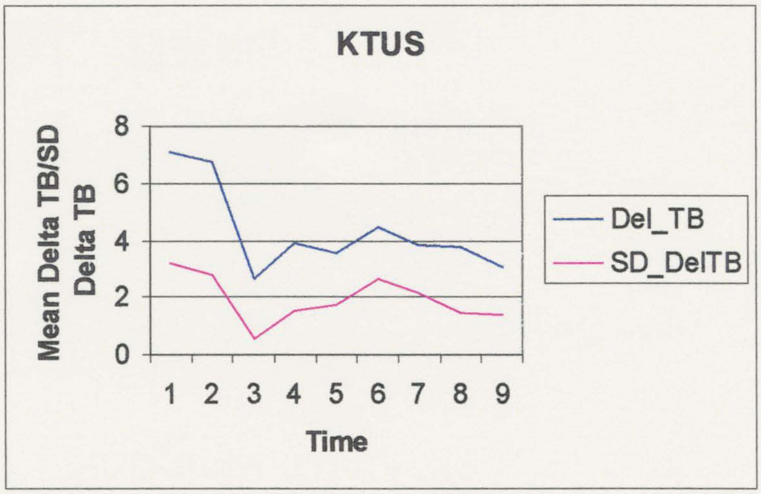

Figure A.43: Tucson, AZ (KTUS) horizontal variation in 85.5 GHz brightness temperature polarization difference and standard deviation over the 90-day period within the 5x5 grid centered on the primary site.

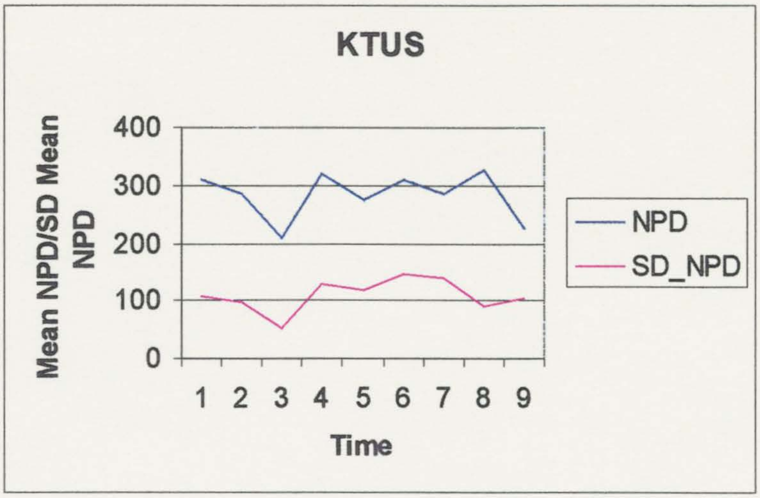

Figure A.44: Tucson, AZ (KTUS) horizontal variation in the NPD value and standard deviation over the 90-day period within the 5x5 grid centered on the primary site.